INVESTIGATION OF PARTICULATE MATTER EMISSIONS FROM GASOLINE DIRECT INJECTION ENGINES: EFFECTS OF LEAN COMBUSTION STRATEGIES, FUEL PROPERTIES, AND LUBE OIL ADDITIVES

A DISSERTATION
SUBMITTED TO THE FACULTY OF
UNIVERSITY OF MINNESOTA
BY

NOAH RICHARD HUNT BOCK

IN PARTIAL FULFILLMENT OF THE REQUIREMENTS
FOR THE DEGREE OF
DOCTOR OF PHILOSOPHY

Prof. WILLIAM F. NORTHROP

October 2020

© Noah Bock 2020

Acknowledgements

I would like to thank my advisor, Professor William Northrop, for his guidance and mentorship throughout my graduate career. The learning environment in Professor Northrop's research group provided me immense growth in my quest from student to scientist. I am likewise extremely grateful for the vast depth of knowledge and technical expertise provided to me by Professor David Kittelson throughout my research endeavors. His support was integral to my success. I would like to thank my committee members, Professor Cari Dutcher and Professor Jonathan Chaplin, for their support in both coursework and thesis work.

I would like to thank Professor Jacob Swanson for his mentorship throughout my undergraduate career, for introducing me to research methodology, and for opening the doors to myriad opportunities. I would like to thank all my colleagues at Thomas E. Murphy Engine Research Laboratory for their camaraderie and support. Specifically, Dr. Jeff Hwang for his leadership, Dr. Dereck Dasrath for comedic relief, and Seamus Kane for his encyclopedic memory. Additionally, I would like to thank Darrick Zarling for his guidance and assistance regarding experimental setups and measurement instrumentation. Lastly, I would like to thank my family for their love and support throughout my studies.

Abstract

Gasoline direct injection (GDI) engines have been widely adopted in passenger vehicles as a replacement for less efficient port-fuel injection (PFI) engines. However, GDI engines emit particulate matter (PM) in much higher concentrations than PFI engines. Human exposure to PM is harmful, causing increased morbidity and mortality. Additionally, PM from internal combustion engines (ICEs) is highly carbonaceous, and due to its high absorption of electromagnetic radiation, contributes to atmospheric warming and climate change. For these reasons, PM emissions from GDI engines are regulated, and the regulatory limits are becoming increasingly stringent. Regulatory limits on PM are an ongoing challenge for GDI engine development, especially in Europe and much of Asia where a particle number limit is enforced. This body of work experimentally investigates PM emissions from GDI engines, PM mitigation strategies, and a novel measurement method that can be used to meet the challenge of verifying reductions in engine emitted PM.

Lean-burn GDI engine operation can further improve thermal efficiency. However, lean-burn fuel injection strategies often lead to higher PM emissions. In the first part of this work, PM emissions were experimentally studied from different GDI combustion modes to identify synergies for simultaneous PM and greenhouse gas (GHG) reduction. Lean stratified injection modes were studied and found to benefit from marginally higher thermal efficiencies than standard GDI combustion modes (stoichiometric) but they produced order/s of magnitude higher PM emissions. It was determined that the use of these modes would only be acceptable with proper implementation of a gasoline particulate filter (GPF). Lean homogeneous modes were studied and showed slightly higher thermal

efficiencies, and in some cases, lower PM emissions than the stoichiometric combustion modes. This highlighted a key area of interest for reducing both PM and GHG emissions. A concerning finding was that there was a high fraction of solid particles in the 10 nm range emitted from GDI engines. This size range is effectively unchecked by current regulations and poses the highest risk to human health. The work provides further evidence for advocating to include 10 nm particles in regulatory number limits.

The second part of this work focused on the effects of fuel properties on PM emissions from GDI engines. Fuel physicochemical properties play a role in particle formation because soot, the main constituent of engine PM, is formed through incomplete combustion of hydrocarbons. Fuels were studied over three sets of experiments: steady state engine operation, regulatory driving transients, and a particle density investigation. It was found that with clean fuel injector tips and under steady state stoichiometric operation, fuel properties did not have a significant impact on PM emissions because the charge mixture preparation was ideal for complete combustion. However, with under nonideal mixture conditions, such as transients or stratified injection strategies, high aromatics and low volatility fuels produced much higher concentrations of PM. Interestingly, it was shown that fuel ethanol concentration has opposing effects on PM emissions. The high heat of vaporization slows fuel evaporation resulting in incomplete combustion and particle formation, but the effect of diluting the fuel aromatics reduces the chemical pathways to soot. A novel “Virtual Drivetrain” software program was developed to test the engine dynamometer as if it were in a vehicle performing and regulatory driving cycle. Through testing various fuels, it was shown that the state of soot loading on the GPF was more

influential on tailpipe PM emissions than the fuel used. This demonstrated the optimizing and controlling the state of loading on the GPF.

Because the amount of soot loaded on a GPF influences filtration efficiency, monitoring the state of loading is important for controlling PM emissions. To do this, understanding of soot oxidation rates is critical. Offline thermogravimetric (TGA) methods, the commonly used approach for measuring oxidation rate in the literature, may not accurately represent oxidation rates on a filter where the macroscopic morphology of the soot, the oxidizer flow process, and the potential for catalytic effects from a filter washcoating all likely play a role in the oxidation process. To resolve this, a novel, in-situ soot oxidative reactivity measurement method was developed. The novel method was demonstrated with a catalytic GPF using oils with additives that would produce soot of different reactivity. It was shown that calcium oil additives increase soot reactivity, while zinc dialkyldithiophosphate (ZDDP) oil additives inhibit oxidation and reduce oxidation rates. These findings and magnitude of the calculated oxidation rates agree with literature. However, calculated oxidation rates were higher for much lower temperatures than reported in literature using TGA indicating a catalytic effect from the GPF wash-coating. The developed method can provide more in-use relevant soot oxidation rates than TGA, and will be useful to researchers, engine developers, and fuel and lubricant scientists.

The last part of this work considered dicarboxylic acid emissions from both GDI and diesel engines equipped with aftertreatment systems (ATS). Although not necessarily emitted as particulate matter from engine, dicarboxylic acids participate in secondary organic aerosol formation. Thus, answering whether modern ATS eliminate dicarboxylic acids is important because it has not yet been studied. It was found that dicarboxylic acids

were emitted from both GDI and diesel engines, and their emission was very sensitive to engine conditions. The ATS largely eliminated dicarboxylic acids, but a significant fraction penetrated the emission control devices under certain conditions. Further study involving assessment of the relative contribution of these acids to atmospheric aerosols is required to understand if improvements in catalysts are warranted to mitigate these acid emissions.

Table of Contents

List of Tables ix

List of Figures xi

Nomenclature xvii

Chapter 1 Introduction 1

1.1 Motivation 1

1.2 Research Objectives 4

Chapter 2 Background 5

2.1 GDI Engines and Engine Generated Particle Emissions 5

2.1.1 Engine Generated Soot 9

2.1.2 Solid Nucleation-mode Particles 12

2.1.3 GPF Implementation 13

2.2 Oxidative Reactivity of Engine-generated Soot 15

2.3 Effects of Fuel Composition on Particle Emissions from GDI Engines 18

2.4 Dicarboxylic Acid Emissions from Internal Combustion Engines 21

Chapter 3 Engine-out Solid Particulate Matter Emissions from Lean and Stoichiometric GDI Combustion 25

3.1 Experimental Setup: Engine and Instrumentation Configuration 25

3.2 Experimental Engine Conditions 28

3.3 Results and discussion 31

Chapter 4 Effects of fuel properties on engine-out and GPF-out GDI PM emissions 40

4.1 Effects of Fuel Properties on Particle Number and Particle Mass Emissions from Lean and Stoichiometric Gasoline Direct Injection Engine Operation 40

4.1.1 Experimental 40

4.1.2 Results and discussion 44

4.1.3 GPF Filtration Efficiency 56

4.2 Influence of Fuel Properties on GDI PM Emissions over First 200 Seconds of WLTP Using an Engine Dynamometer and Novel "Virtual Drivetrain" Software 58

4.2.1 Motivation 58

4.2.2 Experimental 59

4.2.3 Results and Discussion 63

4.3 Effects of ethanol concentration and combustion strategy on the effective density of GDI PM 71

4.3.1 Experimental 72

4.3.2 Results and discussion 73

Chapter 5 A Novel, In Situ Soot Oxidative Reactivity Measurement Method: The Effects of Lube Oil Ash on GDI Soot Oxidative Reactivity in a Catalytic GPF 77

5.1 Operating Conditions and Setup 77

5.2 Experimental Methods: Oxidation Rate Calculation 81

5.3 Results and Discussion 84

Chapter 6 Dicarboxylic Acid Emissions from Aftertreatment Equipped Diesel and Catalyzed GPF Equipped GDI Engines 94

6.1 Dicarboxylic Acid Emissions from Aftertreatment Equipped Diesel Engines. 94

6.1.2 Experimental methods 95

6.1.3 Results and Discussion 101

6.2 Dicarboxylic Acid Emissions from a GDI Engine Equipped with a Catalytic Gasoline Particulate Filter..... 109

6.2.1 Experimental Methods..... 109

6.2.3 Results and Discussion 113

Chapter 7 Conclusions and Suggested Future Work 122

7.1 Engine-out PM Emission from Lean and Stoichiometric GDI..... 122

7.2 Fuel Effects on Lean and Stoichiometric GDI PM Emissions 123

7.3 A novel, in-situ soot oxidation measurement method 126

7.4 Dicarboxylic Acid Emissions from Aftertreatment Equipped GDI and Diesel Engines 127

Bibliography 129

List of Tables

Table 1: BMW N43-B20 Engine Specifications 26

Table 2: Engine conditions including operating mode and equivalence ratio 30

Table 3: Fuel property data and PM Index (PMI)..... 41

Table 4: Engine conditions tested. S=stoichiometric, LH=Lean homogenous, LS=lean stratified 73

Table 5: Oil formulations used for the 79

Table 6: Engine conditions for GPF loading oxidation experiments..... 79

Table 7: Injection strategy and spark timing for the oxidizing GPF loading conditions 80

Table 8: Nominal engine parameters for the three combustion modes tested. BMEP = brake mean effective pressure in bar, ET = energizing time in ms, SOI = start of injection in degrees before top dead center (°bTDC), EGR = exhaust gas recirculation rate in %. 96

Table 9: Lower limit of detection (LOD) for all acids measured in the experimental study including emissions index (mg/kg-fuel) for each engine mode. 101

Table 10: Average gas phase and particulate phase emissions factors for the three engine modes and two sampling locations, engine out (EO) and DPF out (DPFO) including one standard deviation from the mean as uncertainty estimate. Soot and PM loaded on filters calculated using filter gas flowrate. ND = not detected and NM = not measured. 103

Table 11: Nominal engine parameters for the two engine conditions tested. Where values differ between the two fuels, E0 and E10 is denoted. BMEP = brake mean effective pressure, BSFC = brake specific fuel consumption, ET = injector energizing time, SOI =

start of injection in degrees before top dead center (°bTDC), and φ = fuel/air equivalence ratio. 110

Table 12: Lower limit of detection (LOD) for all acids measured in the experimental study including emissions index (mg/kg-fuel) for each engine condition. 113

Table 13: Ratio of the acid emission factors for lean stratified engine condition to the stoichiometric engine condition for both fuels and both sample locations. Inf. = detectable strat concentration but stoich concentration below LOD, - = both strat and stoich below LOD. 118

Table 14: Ratio of E0 acid emission factor to E10 acid emission factor for each engine condition and sample location. inf. = detectable E0 concentration but E10 concentration below LOD, - = both E0 and E10 below LOD. 120

Table 15: GPF acid conversion efficiency for each fuel and engine condition. 121

List of Figures

Figure 1: Typical engine exhaust particle composition and structure [34] 8

Figure 2: Typical number and mass weighted size distribution from a diesel engine with alveolar deposition fraction [34] 9

Figure 3: Soot formation from gas phase to solid agglomerates [38] 10

Figure 4: Diesel fuel jet diffusion flame [39] 11

Figure 5: Ceramic wall-flow filter [22] 14

Figure 6: Engine and instrumentation schematic for engine-out solid particle emissions study 27

Figure 7: Representative injection strategy and spark timing versus crank angle degree (CAD) for the respective combustion modes 29

Figure 8: Average BSFC for the 10 steady state engine conditions. Error bars represent one standard deviation. 32

Figure 9: Average brake specific solid PN > 10 nm emissions as measured by EEPS for the 10 steady state engine conditions. Error bars represent one standard deviation. .. 33

Figure 10: Average brake specific soot emissions as measured by MSS for the 10 steady state engine conditions. Error bars represent one standard deviation. 33

Figure 11: SPN > 10 nm fraction between 10 nm and 23 nm. 34

Figure 12: Solid particle size distributions for all engine conditions 35

Figure 13: Correlation between MSS and PM calculated by EEPS. 36

Figure 14: Correlation between SPN and PM calculated by EEPS compared to that of Khalek et al. for stoichiometric GDI [17]. 38

Figure 15: Correlation between SPN > 23 nm and soot emissions measured by MSS compared with the PN to PM reported by Maricq et al. for stoichiometric GDI [111]. ... 39

Figure 16: Distillation curves for each of the fuels analyzed 42

Figure 17: Engine and instrumentation schematic showing dilution system and instruments used in the experimental study 44

Figure 18: Engine-out particle size distributions for the lean homogenous combustion mode at the four different engine conditions for each of the seven fuels tested. From top left to bottom right: LH1, LH2, LH3, and LH4. 46

Figure 19: Correlation between PN and the PM Index for the lean homogenous combustion mode at the 2000 rpm 7 bar BMEP engine condition with the E50 fuel omitted 48

Figure 20: Correlation between PM mass and the PM Index for the lean homogenous combustion mode at the 2000 rpm 7 bar BMEP engine condition with the E50 fuel omitted 49

Figure 21: Correlation between PN and the PM Index for the lean homogenous combustion mode at the 2400 rpm 7 bar BMEP engine condition with the E50 fuel omitted 49

Figure 22: Correlation between PM mass and the PM Index for the lean homogenous combustion mode at the 2400 rpm 7 bar BMEP engine condition with the E50 fuel omitted 49

Figure 23: Engine-out particle size distributions for the lean homogenous combustion mode at the two different engine conditions for each of the seven fuels tested 51

Figure 24: Clean injector tip (left) and dirty injector tip (right) 52

Figure 25: Engine-out particle size distributions for the stoichiometric combustion mode at the four different engine conditions for each of the seven fuels tested..... 53

Figure 26: Correlation between PN and the PM Index for the stoichiometric combustion mode at the 2000 rpm 7 bar BMEP engine condition..... 55

Figure 27: Correlation between PN and the PM Index for the stoichiometric combustion mode at the 2000 rpm 7 bar BMEP engine condition..... 55

Figure 28: Size-resolved GPF filtration efficiency as a function of non-oxidized soot mass loading on the GPF per GPF volume for the A-2 and E50 fuels 57

Figure 29: Schematic of virtual drivetrain, driving cycle controller and engine hardware 62

Figure 30: Simulated vehicle speed versus time over the first 200 seconds of the WLTP cycle compared to the manufacturer-provided data and the prescribed target speed for the cycle. 63

Figure 31: Engine torque (left) and engine speed (right) versus time over the first 200 seconds of the WLTP cycle compared to the manufacturer-provided engine data 64

Figure 32: Average pre- and post-GPF PSDs over the first 200 seconds of the WLTP 66

Figure 33: Cumulative solid PN > 23 nm pre- and post-GPF (left) and cumulative PM pre- and post-GPF (right) over the first 200 seconds of the WLTP..... 68

Figure 34: Average size resolved filtration efficiency over each 200 second run of the WLTP for fuels A-2, V-1, and E50..... 69

Figure 35: Correlation between cumulative soot mass and fuel aromatics concentration (top left), cumulative soot mass and PMI (top right), cummulative solid PN > 23 nm and

fuel aromatics concentration (bottom left), and cummulative solid PN > 23 nm and PM Index (bottom right) over the first 200 seconds of the WLTP. All emissions are pre-GPF. 71

Figure 36: Sampling system schematic for density measurements 72

Figure 37: Particle size distributions for each engine condition and fuel 74

Figure 38: Measured effective density functions for each engine condition and fuel 75

Figure 39: Comparison of total soot concentration measured by MSS and those calculated from ISPD methods using the corresponding measured effective density functions 76

Figure 40: Engine setup and sampling schematic for GPF loading oxidation experiments 78

Figure 41: Reference non-oxidizing loading condition: average filtration efficiency at 100 nm as a function mass of soot on filter for three oil formulations tested and a non-oxidizing loading condition 85

Figure 42: Pre-GPF particle size distributions for each of the oxidizing GPF loading engine conditions and each of the oils 86

Figure 43: Filtration efficiency at 100 nm and specific soot oxidation rates for each oil at the Mid Temp condition 88

Figure 44: Filtration efficiency at 100 nm and specific soot oxidation rates for each oil at the High Temp condition 89

Figure 45: Filtration efficiency at 100 nm and specific soot oxidation rates for each oil at the High Temp High Soot condition 91

Figure 46: Equilibrium specific soot oxidation rates for each engine condition and oil 92

Figure 47: Diagram of the test setup used in the experiments including sampling train and instrumentation. MSS = Micro-soot sensor, EP = Ejector pump diluters, FTIR = Fourier Transform Infrared analyzer, FID = Flame ionization detector, SMPS = scanning mobility particle sizer. 98

Figure 48. Engine-out particle size distributions for each engine condition tested in the experiments. 104

Figure 49: Gas phase and particle phase organic acid emission factors for the three engine conditions and two sampling locations for; A) KOH impregnated filters, and B) un-impregnated (plain) filters. Adipic acid was not measured for any condition and is omitted from the figure. 105

Figure 50: Diagram of emissions sampling and measurement equipment. MSS = micro soot sensor, FTIR = Fourier transform infrared spectrometer, FID = flame ionization detector, GPF = gasoline particulate filter, TWC = three-way catalyst, EP = ejector pump diluter, MFC = mass flow controller, Vac = vacuum pump, CS = catalytic stripper, EEPS = engine exhaust particle sizer. 111

Figure 51: Gas phase emissions from each engine condition, fuel, and sample location measured by the AVL emissions bench. Error bars represent one standard deviation from the mean of the three runs. 114

Figure 52: Solid particle size distributions for each engine condition, fuel, and sample location measured by the two EEPS's. Error bars represent one standard deviation from the mean of three runs. 115

Figure 53: Acid emissions in emission factors (EF) for each engine condition, fuel, and sample location from the GC-MS analysis. Error bars represent on standard deviation from the mean of three samples. 116

Nomenclature

°bTDC	Degrees before Top Dead Center
AKI	Anti-Knock Index
ATS	After Treatment System
BC	Black Carbon
BET	Break Even Temperature
BMEP	Brake Mean Effective Pressure
BSFC	Brake Specific Fuel Consumption
CAD	Crank Angle Degree
CARB	California Air Resources Board
CDC	Conventional Diesel Combustion
CIMS	chemical ionization mass spectrometry
CPC	Condensation Particle Counter
CPMA	Centrifugal Particle Mass Analyzer
CS	Catalytic Stripper
DBE	Double Bond Equivalent
DMA	Differential Mobility Analyzer
DOC	Diesel Oxidation Catalyst
Dp	Particle Diameter
DPF	Diesel Particulate Filter
DPFO	Diesel Particulate Filter Out
E0	Ethanol Free Gasoline
E10	10% Ethanol Gasoline
E30	30% Ethanol Gasoline
E50	50% Ethanol Gasoline
EC	Elemental Carbon
ECM	Engine Control Module
ECU	Engine Control Unit
EEPS	Engine Exhaust Particle Sizer
EF	Emission Factor
ELTC	Early Low Temperature Combustion
EO	Engine Out
EP	Ejector Pump
FID	Flame Ionization Detector
FTIR	Fourier transform infrared spectrometer
GC-MS	Gas Chromatography-Mass Spectrometry
GDI	Gasoline Direct Injection
GHG	Green House Gas
GPF	Gasoline Particulate Filter
HOV	Heat of Vaporization
HR-TEM	High Resolution-Transmission Election Microscopy
HTO-TDMA	High Temperature Oxidation - Tandem Differential Mobility Analyzer

IPSD	Integrated Particle Size Distribution
LDD	Light Duty Diesel
LOD	Limit of Detection
LSPI	Low Speed Pre-Ignition
LTC	Low Temperature Combustion
MAF	Mass Air Flow
MAP	Manifold Absolute Pressure
MPPS	Most Penetrating Particle Size
MSS	MicroSoot Sensor
NDIR	Non-Dispersive Infrared
NEDC	New European Driving Cycle
NI	National Instruments
OC	Organic Carbon
PAH	Polycyclic Aromatic Hydrocarbon
PAO	Polyalphaolefin
PFI	Port Fuel Injection
PM	Particulate Matter
PMP	Particle Measurement Programme
PN	Particle Number
PSD	Particle Size Distribution
PSL	Polystyrene Latex
RF	Radio Frequency
SI	Spark Ignition
SME	Soy Methyl Ester
SMPS	Scanning Mobility Particle Sizer
SOF	Soluble Organic Fraction
SOI	Start of Injection
SPN	Solid Particle Number
TDC	Top Dead Center
TGA	Thermogravimetric Analysis
THC	Total Hydrocarbon
TWC	Three Way Catalyst
VOC	Volatile Organic Fraction
VPR	Volatile Particle Remover
WLTP	World-harmonized Light-duty Test Procedure
ZDDP	Zinc Dialkyldithiophosphate

Chapter 1 Introduction

1.1 Motivation

Continued pressure exists to improve vehicle engine efficiency to reduce greenhouse gas (GHG) emissions that drive anthropogenic climate change. Many vehicle manufacturers are attempting to meet this challenge by implementing gasoline direct injection (GDI) engines that offer improved fuel economy over their port fuel injection (PFI) counterparts. However, GDI engines are beset by high particulate matter (PM) emissions compared to PFI engines [1–6] and modern diesel engines employing diesel particulate filters (DPF) [7–9]. Increasingly stringent particle emissions regulations present a significant challenge to this technology. Specifically, the California Air Resources Board (CARB) LEV III PM emissions standards are an upcoming challenge for GDI engines as the 3 mg/mi limit is currently being phased in and a 1 mg/mi limit will be phased in starting in 2025 [10]. Additionally, the European Commission enacted the first particle number (PN) limit from GDI vehicles of $6x10^{12}$ solid particles > 23 nm per km with the Euro 6 standard in 2014. The limit was reduced by an order of magnitude to $6x10^{11}$ solid particles > 23 nm per km in 2017 [11]. These PM emissions standards have been imposed due to evidence from epidemiological studies showing human exposure to fine/ultrafine PM results in a higher incidence of respiratory distress, morbidity, and mortality [12,13].

Fuel physicochemical properties have a considerable impact on particle emissions from both gasoline and diesel engines. Understanding this effect is crucial for designing combustion systems that can meet regulatory limits while operating on a range of commercially available fuels. There is currently significant effort focused on characterizing fuel effects on particle emissions from GDI engines [4,14–20]. However, published

research on the effects of fuel properties on particle emissions from lean GDI combustion strategies is scarce. GDI engine technology can enable lean-burn combustion modes, which further increase thermal efficiency but can also increase PM emissions. Identifying synergies between fuel formulation and lean-burn combustion strategies can lead to reductions of both greenhouse gas and PM emissions.

As PN emissions standards become increasingly stringent, fuel formulation and in-cylinder combustion strategies alone are likely not enough to meet the required reductions. Because of this, auto manufacturers are expected to implement gasoline particulate filters (GPFs) to reduce tailpipe particulate matter emissions from GDI engines. GPFs are very effective at reducing PM emission by filtering the engine exhaust and trapping PM on the filter. Widespread adoption of GPFs is currently underway in both Europe and China [21].

Because accumulation of PM on the filter leads to a higher pressure drop in the exhaust system, which reduces engine efficiency, GPFs require periodic regeneration. Filter regeneration occurs when exhaust temperatures and oxygen concentrations are sufficiently high that soot, which is the main constituent of engine PM, oxidizes and is burned off the filter. GPF regeneration often happens passively under normal driving conditions due to the higher exhaust temperatures of gasoline engine exhaust, and active regeneration strategies are not required as they are for diesel engines. Increased soot loading also has a beneficial impact of significantly increasing the filtration efficiency of GPFs [22]. Controlling the soot loading on the filter is critical to the balance of maintaining high filtration efficiency while keeping the pressure drop low enough to not impact engine efficiency. Additionally, if regeneration is initiated with too much accumulated soot on the filter, a thermal runaway event that damages the filter can occur. Soot oxidation kinetics

must be well understood to develop engine strategies that allow the effective GPF performance.

Recent studies have examined the oxidative reactivity of GDI soot and factors that may influence it, but the current breadth of literature is far from comprehensive [23,24]. Soot oxidative reactivity is generally measured using an offline method. However, there may be differences in the kinetics of soot oxidation in the offline method and the kinetics of soot oxidation on a GPF, especially in the case of catalyzed GPFs. Investigation of oxidation rates of soot in its state of interest, on filter, is necessary to achieve confidence in how GPFs load and regenerate. This can be achieved with an in-situ soot oxidative reactivity measurement method.

Only solid PM is regulated under emissions standards, however, atmospheric aerosols are composed of both liquid and solid PM. Atmospheric aerosols originate from both primary sources, such as vehicle exhaust, and secondary sources, such as atmospheric reactions of precursor gases. Dicarboxylic acids make up a significant portion of the soluble organic fraction (SOF) of atmospheric aerosols [25–28]. These acids influence nucleation rates of atmospheric particles and are thought to be derived mainly from secondary, atmospheric reactions. However, some evidence exists that dicarboxylic acids are emitted from combustion sources, suggesting they also originate from primary sources [29,30]. Investigation into the engine conditions and configurations which produce these acids, and whether exhaust aftertreatment systems removes them, is required to better understand the full scope of impact vehicle emissions have on atmospheric PM.

1.2 Research Objectives

The first objective of this work was to determine the effects of fuel physicochemical properties on solid particle emissions from stoichiometric, lean stratified, and lean homogeneous combustion modes of a GDI engine operating in representative steady state and transient engine conditions. This work included using a baseline fuel to identify a set of steady state engine conditions that were of interest regarding PM emissions. Then, PM emissions from these conditions were evaluated with a range of fuels with varying properties. An engine dynamometer software program was developed to enable transient testing under regulatory driving cycles that usually require a full vehicle on a chassis dynamometer. This novel platform was used to investigate PM emissions from the engine operating with various fuels over the driving cycles. The last part of this objective was achieved with particle density measurements. These measurements showed the impact of fuel ethanol concentration and combustion mode on particle morphology and allowed the measurement of real-time particle mass emissions.

The second objective of this work was to identify the effect of specific lube oil additives on the oxidative reactivity of GDI soot particles using a novel, in situ oxidative reactivity measurement method. A method was developed for calculating on-filter soot oxidation rates by measuring the filtration efficiency of a catalyzed GPF while it was undergoing loading and passive oxidation simultaneously. The method was used to show differences in soot reactivity caused by lube oil additives at various engine conditions.

The third and final objective of this work was to quantify dicarboxylic acid emissions from both a diesel engine and GDI engine. Measurements were taken before and after the aftertreatment devices of each engine under various engine conditions. These

measurements demonstrated which combustion strategies produced dicarboxylic acids and at what conditions the exhaust after-treatment systems were effective at removing them.

Chapter 2 Background

2.1 GDI Engines and Engine Generated Particle Emissions

GDI engines can attain higher thermal efficiency compared to their PFI counterparts for several reasons. As the name implies, GDI engines inject fuel directly into the combustion chamber as opposed to injecting fuel into the air intake ports as is done in PFI engines. In PFI engines, the fuel and air are mixed outside of the combustion chamber, allowing more time for the fuel to fully evaporate and mix with the air as it travels from the intake port into the combustion chamber. During the trip from the intake port to combustion chamber, the charge cools due to the evaporation of the fuel. This charge cooling is advantageous because it increases the charge density thus allowing more charge to enter the cylinder. In PFI engines, a portion of the latent heat of vaporization of the fuel comes from the intake ports and intake valves, whereas in GDI engines, the full charge cooling benefit from fuel vaporization is realized in-cylinder, leading to a cooler and denser charge and thus higher volumetric efficiency than in PFI engines.

GDI engines can operate at fuel lean conditions not attainable in PFI engines. Fuel lean combustion offers efficiency benefits in IC engines for several reasons. Fuel lean combustion, or more commonly referred to as lean combustion, is combustion that occurs with more oxidizer than is required for a chemically balanced (stoichiometric) reaction. Fuel rich combustion is combustion that occurs with more fuel than is stoichiometric. The equivalence ratio, φ, is a measure of deviation from stoichiometry of an air and fuel mixture and is defined as the ratio of the stoichiometric air fuel ratio to the actual air fuel ratio ($\varphi >$

1 = rich, φ < 1 = lean). Lean engine operation can increase engine thermal efficiency by reducing throttling losses and by increasing the specific heat ratio of the charge. By allowing more air to enter the engine than is stoichiometrically required, less work is required to move the pistons during the intake stroke, i.e. when the intake manifold pressure is close to that of the crankcase pressure, less work is required to move the piston during the intake stroke, and therefore more useful work is produced per engine cycle.

Another efficiency gain attained from lean operation can be explained by first looking at the cycle efficiency of the Otto cycle, an idealized cycle used for comparison to a spark ignition (SI) engine cycle. The Otto cycle efficiency is defined as

$$\eta_{Otto} = 1 - \frac{1}{r^{\gamma-1}} \qquad \text{Eq. 2.1}$$

where r is compression ratio and γ is the specific heat ratio of the intake charge. The specific heat ratio of a stoichiometric mixture of gasoline and air is approximately 1.3 whereas that of air is 1.4, thus, the specific heat ratio of a fuel air mixture increases as φ decreases [31,32]. Consequently, the thermal efficiency of an IC engine increases as equivalence ratio decreases. Additionally, the cooler charge temperature achieved from direct injection and from lean operation reduces the risk of pre-ignition (knock) which allows higher compression ratios to be run and further increases thermal efficiency.

There exists a lean combustion limit for SI engines employing a homogeneous charge. The lean limit for a SI engine fueled with gasoline/isooctane is usually no lower than about φ =0.7 [33]. To achieve lower equivalence ratios in SI engines, fuel stratification is often required. Fuel stratification is achieved by an injection event during the compression stroke to form a locally fuel rich region near the spark plug and ignite a globally lean fuel-air

mixture. The major limitation of PFI injectors is that they cannot inject fuel into the engine while the intake valve is closed. This constrains them to homogenous charge operation. Because GDI engines inject fuel directly into the combustion chamber, fuel delivery is not limited by valve events, and they are able to utilize fuel stratification injection strategies.

The fuel injection strategies used by GDI engines, which provide efficiency advantages, also produce higher PM emissions. By injecting fuel directly into the combustion chamber, the fuel has less time to adequately mix with the intake air resulting in locally fuel rich regions that produce soot. Fuel spray overpenetration can also wet in-cylinder surfaces, leaving fuel films, which burn as diffusion flames, as opposed to burning by clean, pre-mixed combustion.

Engine generated nanoparticles are composed of both solid (non-volatile) and liquid (semi-volatile) material. The non-volatile portion of PM is composed of carbonaceous soot, produced from fuel rich regions of combustion, and metallic ash particles, derived from lubrication oil additives. The semi-volatile portion, sometimes called the soluble organic fraction (SOF) or volatile organic fraction (VOF), is composed mainly of unoxidized organics from fuel and lubrication oil, but also includes sulfates and aqueous sulfuric acid. The semi-volatile portion of PM is formed through nucleation when gas phase species become supersaturated as the engine exhaust cools as it travels through the exhaust system and eventually mixes with ambient air. Figure 1 shows an illustration of the composition and structure of engine nanoparticles copied from Ref. [34].

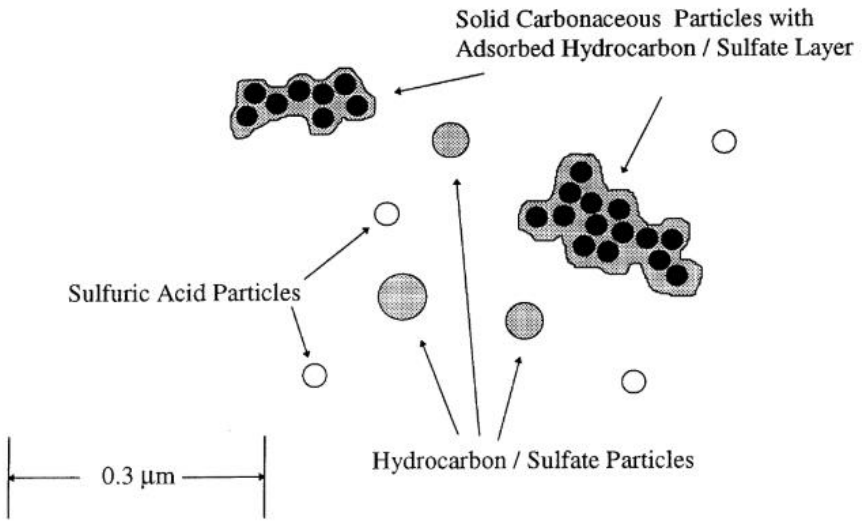

Figure 1: Typical engine exhaust particle composition and structure [34]

Particulate matter emissions from engines fit well to lognormal distributions. Figure 2 shows a typical particle number and mass weighted distribution for a diesel engine, copied from ref. [34]. The nucleation, or nuclei, mode with a number peak near 20 nm, dominates the number distribution and is composed of semi-volatile material and ash. The accumulation mode, with a number peak near 100 nm, dominates the mass distribution and is composed of soot agglomerates, adsorbed semi-volatiles, ash. The nucleation mode is very sensitive sampling conditions, specifically, dilution ratio and temperature, while the solid fraction of the accumulation mode is stable under most conditions [35].

PM mass emissions have traditionally been measured by gravimetric analysis for regulatory compliance. However, because GDI engines and DPF equipped diesel engines emit much lower solid mass concentrations than previous generation diesel engines, sensitivity and repeatability issues arise from the variance in semi-volatile PM emitted [36]. The PN limit imposed in Europe applies only to solid particles greater than 23 nm. This criterion eliminates the variance caused by the semi-volatiles in PM, and is more suitable

for low emitting engines, such as DPF equipped diesels and GDI engines. However, the number limit of $6x10^{11}$ #/km is a more imposing challenge than the current mass limits, especially for GDI engines which more particles of smaller sizes per unit mass than diesel engines [17]. Additionally, GDI engines have been shown to emit a much lower fraction of organic carbon than diesel engines [20]. For these reasons, the focus of the current work is on solid particle emissions.

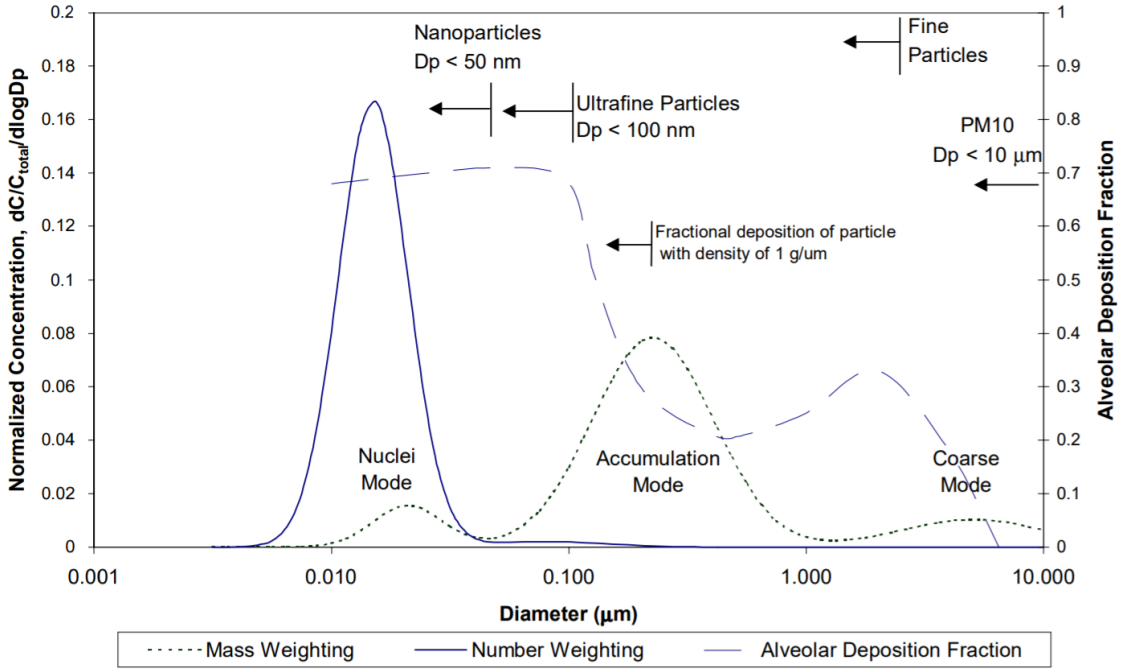

Figure 2: Typical number and mass weighted size distribution from a diesel engine with alveolar deposition fraction [34]

2.1.1 Engine Generated Soot

Soot (also referred to as black carbon (BC) or elemental carbon (EC)), the largest contributor to engine exhaust PM mass, is formed in locally fuel rich regions of combustion. The lack of oxygen in the fuel rich regions causes fuel pyrolysis and polycyclic aromatic hydrocarbons are formed. It is the consensus among combustion researchers that gaseous PAHs act as precursors in soot formation. PAHs form and grow

by chemical reactions until a point at which they become large enough that they adhere to each other during collisions, forming clusters, i.e. nucleation. These clusters then grow by collisions with other clusters as well as with molecular PAHs, while the gaseous PAH compounds are undergoing chemical molecular growth. This continues until the PAH clusters coalesce and form solid primary particles of tightly bound, graphitized carbon, representing the pathway for the gas-to-particle conversion of hydrocarbons to soot. The final step of soot formation is the collision of primary particles to form fractal soot particle agglomerates [37,38]. This process is illustrated in Figure 3, copied from ref. [38].

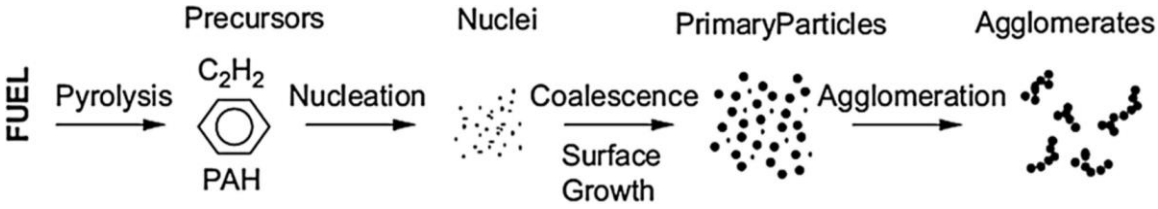

Figure 3: Soot formation from gas phase to solid agglomerates [38]

There are two main sources of soot formation in IC engines: from locally rich fuel air mixtures in the gas phase due to charge inhomogeneity, and from liquid fuel films on cylinder surfaces. Locally rich fuel air mixtures occur in IC engines when there is insufficient time, charge motion, and/or heat in the period between start of injection and start of combustion to fully mix and vaporize the fuel. Diesel engines, for example, inject fuel directly into the combustion chamber just prior to the piston reaching top dead center (TDC) during the compression stroke. Combustion commences at the periphery of the fuel jet as the fuel evaporates and hot oxidizer diffuses into the fuel jet. Soot is formed in high concentrations on the fuel rich side of the flame front. This is illustrated in Figure 4, copied from ref. [39]. Similarly, soot producing diffusion flames can occur in GDI engines from fuel dripping from the injectors, from excessive fuel spray penetration that wets the piston

surface, cylinder walls, or spark plug, and from poor charge mixing that leaves either suspended liquid droplets of fuel or locally rich regions in the combustion chamber.

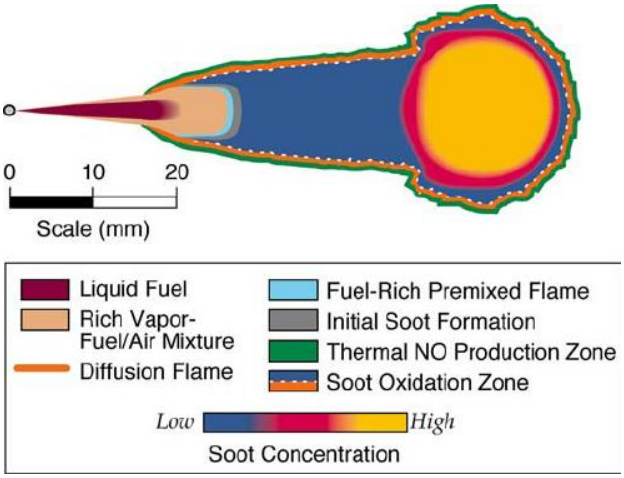

Figure 4: Diesel fuel jet diffusion flame [39]

Particle morphology influences fundamental properties on which particle measurement instruments operate, such as transport properties, optical properties, and electrical charging properties. The density of nanostructured particles, like soot agglomerates, is not equal to that of the bulk material from which they are composed. Because of this, a quantity called effective density, ρ_e, is used to relate electrical mobility dimeter and particle mass:

$$\rho_e = \frac{6m}{\pi d_m^3} \qquad \text{Eq. 2.2}$$

where m is the mass of the particle and d_m is the mobility diameter of the particle. Effective density provides information on particle morphology, which can be used for converting between different particle sizing methods (e.g. mobility diameter to aerodynamic diameter) and can enable real-time particle mass distribution measurement. The particle sphericity can be determined using the mass mobility exponent, D_{mm}. The mass mobility exponent ranges from 1, for infinitely long, chain-like agglomerates, to 3, for spherical particles. The relationship between D_{mm}, mobility diameter, and effective density are:

$$m = C \cdot {d_m}^{D_{mm}} \quad \text{Eq. 2.3}$$

$$\rho_e = C' \cdot {d_m}^{D_{mm}-3} \quad \text{Eq. 2.4}$$

where C and C' are constants [40].

As discussed earlier, the gravimetric method currently used to determine regulatory compliance with particle mass emission limits may not be sensitive enough for future limits. As particle mass emission limits become increasingly stringent, and engines become cleaner, the amount of mass collected on a filter may be insufficient for accurate mass emission measurements. However, with the characterization of effective density, real-time particle mass emissions can be measured with particle sizing instruments with much greater sensitivity than gravimetric methods.

2.1.2 Solid Nucleation-mode Particles

Non-volatile sub-23nm particles composed of metal oxides that originate from fuel and/or lubrication oil additives have been shown to make up a substantial portion of GDI PN [41–43] and can dominate solid particle number (SPN) distributions measured from PFI engines [44]. As discussed previously, engines typically emit total PN size distributions that fit a bimodal lognormal distribution comprising a nucleation mode of semi-volatiles and ash, and an accumulation mode of soot, semi-volatiles and ash. When the semi-volatile material is removed, the accumulation mode scavenges most of the ash, leaving only an accumulation mode. However, if there is a large amount of ash present relative to soot, a separate, solid ash mode may be found in the 10 nm diameter range [45–48]. Diesel and SI engines both have been shown to have high solid nucleation mode emissions during cold start and idle conditions [49–51]. A thorough review of the literature

conducted in 2014 showed the percentage of sub-23 nm SPN is typically between 30-40% for stoichiometric GDI engines [52].

The 10 nm ash mode is not counted in current emissions standards because it only accounts for a tiny fraction of mass that would be measured under the particle mass emission limits and it is below the 23 nm cutoff for PN under current EU rules. However, smaller particles pose greater toxicological harm due to increased surface to volume ratio, higher penetration into the human respiratory system, and increased likelihood of passage through cell membranes and the blood brain barrier [53,54]. For these reasons, future PN regulations may include particles as small as 10 nm. It is likely that this regulation could only be met by implementing GPFs.

2.1.3 GPF Implementation

GPFs are composed of wall-flow ceramic substrates (shown in Figure 5 [22]) that can effectively remove a large fraction of PM from tailpipe emissions. Implementing GPFs on GDI vehicles is the most effective method for reducing exhaust particles to meet increasingly stringent emissions standards [42]. The combination of increasingly stringent PM emission regulations around the world, specifically in Europe and China, and the high concentration of PM emitted by GDI engines has led to the consensus that GPFs will become ubiquitous in GDI-equipped vehicles [55–57]. GPFs can be coated with a three-way catalyst washcoating to remove unburned hydrocarbons, oxides of nitrogen, and carbon monoxide from the exhaust [55]. This combines the functions of a catalytic converter and particulate filter into one device, reducing the need for additional system components.

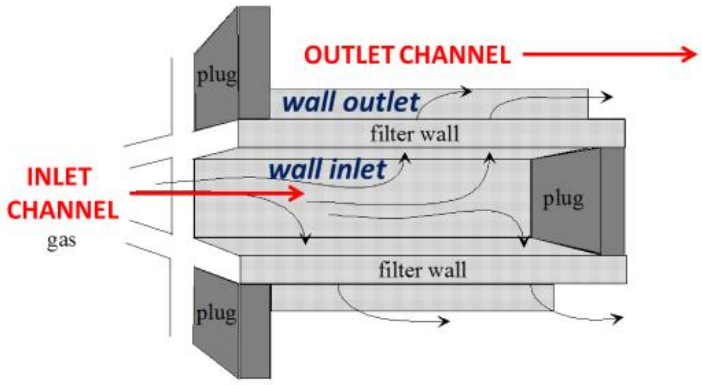

Figure 5: Ceramic wall-flow filter [22]

As with diesel particulate filters, GPF filtration efficiency increases as soot is loaded on the substrate. GPF total number filtration efficiencies are usually between 50 and 80% when the filter is clean to over 99% with sufficient soot loading [58,59]. The level of soot loading required to reach ~99% filtration efficiency is on the order of 100 mg soot per L of filter volume for blank filters and less than that for catalyzed filters [57]. This is due to pore filling and the buildup of a "soot cake" through which additional filtration occurs. However, the soot-cake also increases the pressure drop across the filter, which results in a fuel efficiency penalty, though this is usually minimal.

Periodic filter regeneration by soot oxidation is needed to remove soot from the filter. In diesel engines, this is typically done by a post-combustion fuel injection late in the expansion stroke [60]. The fuel is oxidized in an oxidation catalyst directly upstream of the DPF to increase exhaust temperatures to a level that will result in the oxidation of soot trapped in the filter. GPFs require less frequent or no active regeneration because the exhaust temperatures are much higher in SI engines and the engine-out soot concentrations are generally much lower. The soot loaded on GPFs is often regenerated passively under ordinary driving conditions, such as high exhaust temperature from acceleration followed

by a fuel cut due to deceleration. It has been shown that during the high speed portions of regulatory cycles, GPFs often oxidize the soot cake which results in higher PM emissions due to the filtration efficiency loss [58]. However, if there is a very high level of soot loading on the GPF, the exotherm of soot oxidation can cause thermal shock and damage the filter substrate. Consequently, accurate GPF soot load estimation is crucial.

Soot loading estimation for GPFs can be accomplished by several methods. Open loop models use engine maps that approximate soot production for certain engine conditions and calculate soot loading based on the amount of time spent at given engine conditions [61]. Closed loop methods rely on filter temperature and pressure sensors to estimate loading based on flow resistance [62]. Microwave or radio frequency (RF) sensors have also been explored and have been shown to have good correlation between sensor gain and soot loading [63]. However, these methods alone all have issue and can result in error when partial soot oxidation occurs. Incorporating soot oxidation kinetics models with RF, pressure, and temperature sensors has been shown to predict the most accurate soot load [64]. To do this, accurate GDI soot oxidation kinetics on GPFs and catalytic GPFs must be known.

2.2 Oxidative Reactivity of Engine-generated Soot

Soot oxidative reactivity is an important parameter for characterizing particulate emissions from engines, specifically because of its implication for particulate filter (GPF/DPF) loading and regeneration. It generally encompasses the temperature required to initiate oxidation of soot particles and the rate at which oxidation proceeds. This information is required to accurately predict the time and temperature required to oxidize the soot loaded on exhaust particulate filters. It is also needed for prediction the level of

soot loading on particulate filters, especially GPFs due to the high exhaust temperatures of gasoline engine exhaust that lead to passive regeneration under normal engine operation.

The predominant method for measuring soot reactivity is thermogravimetric analysis (TGA). The TGA method consists of weighing a soot sample in a crucible that is suspended from a microbalance in a furnace at high temperature and in the presence of oxygen. The furnace temperature can either be held at constant temperature for isothermal oxidation experiments or ramped from ambient temperature to ~ 1000 °C. Information about the reactivity of the soot can be determined by the rate of change in mass of the soot sample as a function of temperature. The volatile organic fraction (VOC) of the soot can be removed from the sample prior to the oxidation experiment by heating the sample in the TGA furnace in an inert gas such as nitrogen. At the end of the TGA experiment, when all the soot has been oxidized, only the ash fraction of the sample remains. The ash mass can be measured to calculate the ash fraction and then the ash can be removed for subsequent analysis.

Another method for characterizing the oxidation kinetics of soot, called high-temperature oxidation tandem differential mobility analyzer (HTO-TDMA), was developed at the University of Minnesota [65]. The experimental setup of this method is composed of two differential mobility analyzers (DMAs) and a high temperature furnace. The first DMA is used to select soot particles of a certain mobility diameter from an input stream so that a monodisperse soot aerosol flows through the furnace. The second DMA is used in scanning mode in conjunction with a condensation particle counter (CPC) to measure the size distribution of the aerosol exiting the furnace. The furnace temperature is

ramped from ambient temperatures to over 1000 °C. Information about the soot reactivity can be determined by the change in particle size through the furnace.

The HTO-TDMA method was developed using soot generated from an ethylene diffusion flame but has been used to determine the kinetics of diesel nanoparticle oxidation [66], the impact of lubricating oil on diesel soot oxidation kinetics [46], the difference in oxidative properties between flame and diesel soot particles [67], the kinetics of biodiesel soot oxidation [68], and kinetics of soot oxidation by NO_2. The results of these studies have revealed the following conclusions: activation energies for diesel soot are dependent on engine condition; metal lubrication oil additives enhance the oxidation rate of diesel soot particles but increased dosing has little effect on the activation energy; soy methyl ester (SME) biodiesel fuel enhances soot oxidation rate; and diesel soot has lower activation energy when oxidized in NO_2 rather than air. Results from HTO-TDMA for GDI soot oxidation experiments have yet to be reported.

Several studies diesel soot oxidative reactivity using TGA have been performed over the last 15 years. These studies have shown that diesel soot reactivity increases with exhaust gas recirculation due to more amorphous soot nanostructure, which promotes core burning [69,70], increases with the addition of biodiesel fuel, again, due to disordered nanostructure [71,72] and possibly, due to increased surface oxygen functionality [73], and that cerium oxide on soot decreases the ignition temperature but not the reaction rate [74,75].

Fundamental work by Vander Wal and Tomasek on acetylene, benzene, and ethanol derived soot showed a strong dependence of oxidative reactivity on soot nanostructure [76]. Parameters identified to influence reactivity were structure “disorderedness”, curvature of

layer planes, and fringe length. In subsequent work they found that the differences in soot nanostructure were dependent on formation conditions [77]. The nanostructure analysis in these studies was performed using high resolution transmission electron microscopy (HR-TEM).

There have been few studies on the oxidative reactivity of GDI soot. All have been performed using the off-line TGA method and stoichiometric or rich combustion. Choi and Seong showed that the fuel- and oil-borne ash fraction of soot particles is likely the most influential parameter on GDI soot reactivity due to catalytic effects [23,24]. More specifically, calcium has been shown to strongly increase the oxidative reactivity of GDI soot and ZDDP inhibits GDI soot compared to other ash components [23,78].

In a Ph.D. thesis, Easter examined the effects of injection parameters on the oxidative reactivity of soot particles from a wall-guided GDI engine from a single stoichiometric engine condition [79]. Four injection parameters were tested including a baseline, late start of injection (SOI), low injection pressure, and early SOI. Because engine speed and load were constant for all tests, oil consumption was likely constant, and therefore PM ash fraction was likely inversely related to soot concentration. Results showed soot oxidative reactivity trended inversely, one-to-one, with soot concentration. Soot nanostructure showed no discernable difference between injection conditions. This indicates that ash fraction and composition may be the dominant factor that determines oxidative reactivity of GDI soot.

2.3 Effects of Fuel Composition on Particle Emissions from GDI Engines

Fuel properties and chemical composition strongly influence soot formation. The fuel property commonly regarded as most relevant to particle emissions is volatility. Because

low volatility fuels require higher temperatures for complete evaporation, they remain in the liquid phase longer after injection. This can result in locally rich regions, suspended liquid droplets, or fuel films on cylinder surfaces, resulting in diffusion flame combustion and ultimately soot production. Generally, aromaticity is the most influential chemical characteristic regarding soot production. If aromatics are present in high concentrations in the fuel, they will be available for the formation and growth of PAH's, where otherwise, the formation and growth of PAH's, and thereby the formation of soot, would be limited by aromatic ring growth through reactions involving aliphatic compounds [37].

Understanding fuel effects on particle emissions from GDI engines is critical due to tightening PM emission regulations that are being imposed around the world. Tanaka et al. showed that lower volatility fuels produce higher PN concentrations from GDI engines, especially under cold engine operating conditions with advanced injection timing, indicating that fuel films were the source of higher emissions of PN with mobility diameter greater than 23 nm (PN > 23 nm) [14]. Additionally, they showed that fuels containing high concentrations of aromatic compounds produced higher PN > 23 nm emissions under rich, homogenous charge conditions compared to fuels with the same distillation curve and lower aromatics. This demonstrated that fuel chemistry influences PM emissions and is relevant for PM emissions originating from locally rich regions like those found in stratified engine conditions.

Information of fuel properties and chemistry have been used to determine a fuel's propensity for PM production. Aikawa et al. developed a predictive model, called the PM Index, for determining a fuel's influence on PM emissions based on the mass fraction,

double bond equivalent (DBE), and vapor pressure of the fuel's components [15]. The PM Index is given by

$$PM\ Index = \sum_{i=1}^{n} \left(\frac{DBE_i + 1}{P_{vap,i}(443K)} \times Wt_i \right) \qquad \text{Eq. 2.5}$$

where DBE_i is the double bond equivalent for component i, $P_{vap,i}(443K)$ is the vapor pressure of component i at 443 K, and Wt_i is the weight fraction of component i. This presumes that high DBE components and low volatility components correspond to a high PM Index. In the study by Aikawa et al., the PM Index showed very strong correlation to PM emissions for vehicles operating under the New European Driving Cycle (NEDC). A supplementary study to the same campaign was conducted at Southwest Research Institute which showed the highest volatility fuel of three fuels tested produced significantly lower PM emissions under various drive cycles [17].

Previous studies have shown that ethanol has minimal impact on PM emissions from stoichiometric GDI operation when in low concentrations of the fuel mixture but has significant impact when in high concentration. Results from Chan show no significant difference between E0 and E10 on PN or soot emissions from a stoichiometric GDI engine running various drive cycles [18]. Storey et al. reported a 30-40% reduction in PM mass emissions from steady state stoichiometric GDI operation with E20 fuel [80]. Maricq et al. reported no statistically significant change in PM emission from E0 to E20, but a statistically significant drop in PM for E32 and E45 fuels [20]. Szybist et al. reported 1 to 2 orders of magnitude reduction in PM emissions from steady state stoichiometric GDI operation with E85 fuel relative to E20 and gasoline fuels [4].

Reduced PM emissions from oxygenated fuels are likely the result of two consequences: soot particles from oxygenated fuels have higher oxidative reactivity and oxygenated fuels have lower concentrations of aromatics. By adding oxygenated components such as ethanol to fuel, the aromatic components are diluted, thereby reducing the production of PAH's which are responsible for soot formation. Oxygenated fuels have been shown to increase the oxidative reactivity of soot particles from GDI engines [81] and diesel engines [82]. Higher soot reactivity leads to increased soot oxidation in-cylinder and in aftertreatment catalysts leading to lower tailpipe soot concentrations. It is still unclear whether the increase in soot reactivity is due to a chemical effect of the oxygenated fuel, such as increased oxygen functional groups, or is simply a result of a larger ash contribution to each soot particle as a result of lower soot formation from low aromatic content fuel. The impact of ethanol on PM emissions from lean GDI combustion has not been thoroughly examined. Further investigation of impacts of fuel properties and chemistry on PM emissions from lean combustion strategies in GDI engines is warranted for seeking simultaneous reduction of GHG and PM emissions.

2.4 Dicarboxylic Acid Emissions from Internal Combustion Engines

Atmospheric particle nucleation processes are important because they control precipitation and human exposure to pollutants. Anthropogenic gases and particles can enhance nucleation and influence and weather patterns [83]. Organic compounds have been shown to make up a significant portion of total atmospheric number concentration and cloud condensation nuclei fraction [84]. The binary nucleation of sulfuric acid and water was originally thought to be the dominant source of new particle formation in the atmosphere; however, this model does not fully account for the observed nucleation rate

and growth of atmospheric particles [85]. The ternary nucleation of water, ammonia, and sulfuric acid is more representative of what occurs in the atmosphere, especially with more recent parametrization which has approximated the observed growth rate within one order of magnitude [86]. Additionally, the presence of aromatic carboxylic acids has been shown to further enhance the growth rate of new atmospheric particles [87]. Similarly, short-chain dicarboxylic acids, such as oxalic, malonic, maleic, and succinic acid, likely encourage particle nucleation by binding to sulfuric acid and ammonia [88], and due to their presence in the atmosphere, could help explain the gap between the observed nucleation rate and the modeled nucleation rate. Atmospheric dicarboxylic acids have traditionally been thought to be products of aqueous particle phase reactions in cloud and fog droplets involving organic anthropogenic precursors such as aldehydes, alcohols, and monocarboxylic acids [25–27,89]. However, atmospheric dicarboxylic acids also likely originate from a combination of primary sources like combustion and secondary gas-phase reactions [29].

Monocarboxylic acids are known products of hydrocarbon combustion in both diesel and spark-ignited engines [90–95] and are ubiquitous in atmospheric aerosols [96]. Direct dicarboxylic acid emissions from engines could provide another route for particle formation. Although atmospheric acids are thought to originate in part from combustion, very few studies have established a clear connection to vehicle emissions. An earlier study by Kawamura and Kaplan [30] strongly suggests that both diesel and gasoline engines are primary sources of gas phase and particle phase dicarboxylic acids. The authors collected gas and particle phase dicarboxylic acids emitted from a non-ATS-equipped diesel engine operating at idle using plain and KOH impregnated filters in series and analyzed them using a derivatization technique. Between 25% and 70% of the dicarboxylic acid mass was

collected on the plain filter. Kawamura and Kaplan reported exhaust concentrations of dicarboxylic acids on orders of 10 to 100 nmol/m^3.

Huang et al. [97] disputed the findings of Kawamura and Kaplan by suggesting oxalic acid was not present in vehicle exhaust. This is significant because Kawamura and Kaplan found oxalic acid to be the most abundant dicarboxylic acid in both the atmosphere and vehicle exhaust. Huang compared samples collected in a roadway tunnel to those collected in an ambient urban environment and found that concentrations from the two collection sites were not significantly different. From these data, they concluded that vehicular emissions were not a primary source of oxalic acid. The sample collection method of Huang et al. consisted of a MOUDI (MSP Corp., Shoreview, MN) aerosol impactor with a final stage cut-size diameter of 56 nm using un-impregnated quartz filters for impaction substrates (no gas flow through filters). It should be noted that from this collection method, due to the sharp cut-size of the impactor and absence of an impregnated filter, no sub-56 nm particulate matter and no gas phase acids would be collected. Additionally, it should be noted that the nucleation mode of combustion generated nanoparticles has a diameter of less than 50 nm [34]. Thus, the oxalic acid collected in the study would have been solely from atmospheric aerosol particles greater than 56 nm. The conclusion that vehicle exhaust is not a primary source of oxalic acid cannot be drawn from this experiment; the work of Kawamura and Kaplan remains valid.

In other work, Fraser et al. [98] determined that vehicle exhaust was a primary source of particle phase aliphatic and aromatic dicarboxylic acids, but did not measure their presence in the gas phase. More recently, Wentzell et al. [99] quantified a number of gas phase acids using chemical ionization mass spectrometry (CIMS), including oxalic acid,

emitted from a light duty diesel (LDD) engine equipped with a diesel oxidation catalyst (DOC). Still other work has identified pathways for organic compounds like dicarboxylic acids to assist the nucleation of sulfuric acid in diesel engine exhaust [100].

After-treatment systems (ATS) of modern engines oxidize unburned organic species and filter emitted nanoparticles and might also remove dicarboxylic acids. Whether dicarboxylic acids are formed during combustion may be of no importance, other than for academic value, if ATS also effectively eliminate them from being emitted into the atmosphere. Diesel ATS are composed of DOCs, DPFs, and selective catalytic reduction (SCR) systems while gasoline engines employ three-way catalysts (TWCs) and sometimes GPFs. Improving tailpipe emissions is an essential step towards improving air quality, a goal that implementing ATS technology has largely achieved [101]. However, Arnold et al. showed that engine ATS can promote the formation of low vapor pressure gases that can lead to nucleation mode particles [102]. These particles mostly consisted of sulfuric acid but also included organic acids. Other work has shown that a diesel ATS was not able to fully convert semi-volatile hydrocarbons when exhaust temperatures were lower than the diesel oxidization catalyst light-off temperature at light engine load [103]. Hydrocarbon slip also occurred when using premixed low temperature combustion (LTC) modes where engine-out unburned hydrocarbon emissions are higher than conventional mixing-controlled diesel combustion. Investigating whether ATS, such as DOCs, DPFs, and catalyzed GPFs, are effective at removing dicarboxylic acids is required to determine if there should be concern that modern engines are primary sources of dicarboxylic acids.

Chapter 3 Engine-out Solid Particulate Matter Emissions from Lean and Stoichiometric GDI Combustion

In the work reported in this chapter, PM emissions from lean and stoichiometric combustion modes were experimentally investigated to determine the impact of various fuel injections strategies at steady state engine conditions. Testing was conducted using a certification fuel that would serve as a baseline of comparison for future fuels testing. This work was presented in a previously published conference paper [104].

3.1 Experimental Setup: Engine and Instrumentation Configuration

A BMW N43B20, four-cylinder, 2.0 L, naturally aspirated engine with centrally mounted spray guided piezo injectors was used for this study. The engine operated in three combustion modes: stoichiometric, lean homogeneous, and lean stratified. Table 1 details relevant engine specifications. Full control of all engine parameters was enabled by National Instruments (NI) software and hardware in lieu of the factory engine control unit (ECU). The software calibration was developed by another research group with the factory ECU and the vehicle on a chassis dynamometer to closely match the engine modes employed by the factory ECU.

Gaseous emissions were measured by an AVL (Graz, Austria) SESAM i60 multi-component exhaust measurement system composed of a Fourier transform infrared spectrometer (FTIR) for gas phase speciation, a flame ionization detector (FID) for measuring unburned hydrocarbon concentrations, and separate CO_2 non-dispersive infrared (NDIR) analyzer. Particle measurement were made with an AVL Micro Soot Sensor (MSS) for measuring soot mass concentration, a TSI (Shoreview, MN) engine exhaust particle sizer (EEPS) spectrometer using the soot inversion matrix for measuring

particle size distributions (PSD) at a rate of 1 Hz, and a TSI scanning mobility particle sizer (SMPS) spectrometer for measuring PSDs. SMPS measurements were taken at steady state conditions with a scan time of 60 seconds to verify size distributions measured by the EEPS.

Table 1: BMW N43-B20 Engine Specifications

Specification	**Value**
Engine Type	4 Cylinder, Inline GDI
Displacement (cc)	1995
Bore x Stroke (mm)	84 x 90
Compression Ratio	12:1
Rated Power (kW)	125 @ 6700 rpm
Rated Torque (Nm)	210 @ 4250
Induction	Naturally Aspirated
Injection	Central Spray Guided Piezo Injectors
Max Rail Pressure (bar)	200

Figure 6 shows the exhaust sampling system and instrumentation used in the study. Dilution was achieved using ejector pump (EP) diluters with critical orifices upstream of the sample flow. The primary dilution ratio was calculated throughout testing at a 1 Hz rate by the ratio of the undiluted to primary diluted CO_2 concentrations as the dilution air was free of CO_2. The primary dilution ratio was approximately 12:1 and the secondary dilution ratio was 40:1. Secondary dilution was used to keep particle concentrations within ranges required by the EEPS and SMPS for engine conditions with high PN concentration. Critical orifices upstream of the ejector pumps were used to maintain a constant volumetric flow

rate (choked flow) of the sample flow. The mass flow rate of the primary sample flow varied slightly corresponding to fluctuations in density of the exhaust stream caused by changes in exhaust temperature and pressure. The conditions upstream of the secondary dilution ejector pump were constant, thus the dilution ratio was assumed to be constant throughout the test and was only measured prior to each test. A catalytic stripper (CS) operated at 300 °C was used upstream of the EEPS and SMPS to remove all volatile and semi-volatile material such that the particle size distributions measured were that of only solid particles. The design and performance of the CS is discussed at length in other work [105].

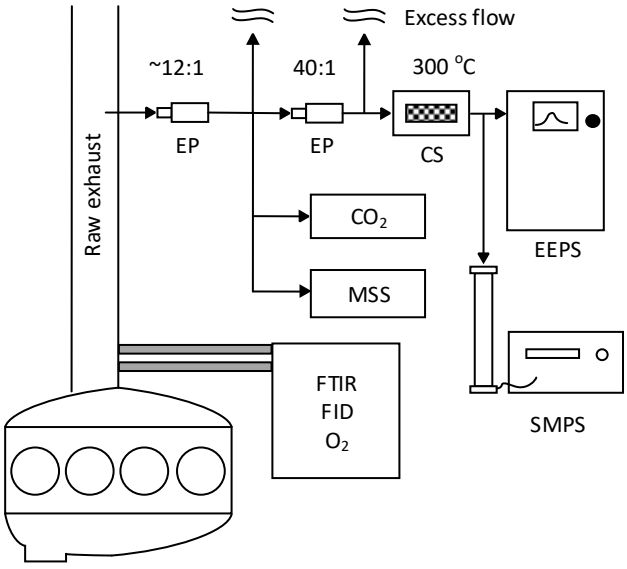

Figure 6: Engine and instrumentation schematic for engine-out solid particle emissions study

It has been shown that re-nucleation of semi-volatile material can occur downstream of the volatile particle removers (VPR) employed by particle measurement programme (PMP) sampling systems resulting in sub-23 nm particles [44]. This is not of concern when using a PMP protocol compliant system with a particle counter with a 23 nm cut-off size.

However, because sub-23 nm particle emissions were of interest for this study, a CS was used instead of a VPR because the CS more effectively removes semi-volatile material [105,106].

Loss through the CS was characterized by challenging it with atomized NaCl particles of four different mobility diameters (15 nm 30 nm, 50 nm and 100 nm) classified by a differential mobility analyzer (DMA). The penetration of these particles was calculated by measured concentrations upstream and downstream of the CS using a condensation particle counter (CPC). A penetration model based on size dependent laminar diffusion losses and essentially size independent thermophoretic losses was fit to the measured penetration data. This penetration model was then applied to the EEPS and SMPS data to obtain size-resolved, loss-corrected particle size distributions. The loss correction was significant, especially for small particles. It increased total solid number concentrations by 40 to 80 %.

3.2 Experimental Engine Conditions

The chosen combustion modes differed primarily in equivalence ratio and injection strategy. Figure 7 shows the injection strategy and spark timing for each of the combustion modes used in this work. The stoichiometric mode featured two injections during the intake stroke with two thirds of the fuel delivered in the primary injection and the remainder in the secondary injection. The lean homogeneous mode featured a primary injection during the intake stroke where two thirds of the fuel was injected, followed by a secondary injection delivering the remainder of the fuel and beginning approximately 10 crank angle degrees (CAD) prior to the spark event. This is not a truly homogeneous charge combustion mode. Instead, the composition of the charge has two thirds of the fuel quantity well mixed and the remaining one third stratified near the spark plug. This allows leaner global

mixtures than would be possible with a truly homogeneous charge. The lean stratified mode featured two injections approximately 20 and 10 CAD prior to the spark event followed by a small, third injection just after the spark. The factory ECU only employed the lean stratified mode up to approximately 5 bar brake mean effective pressure (BMEP).

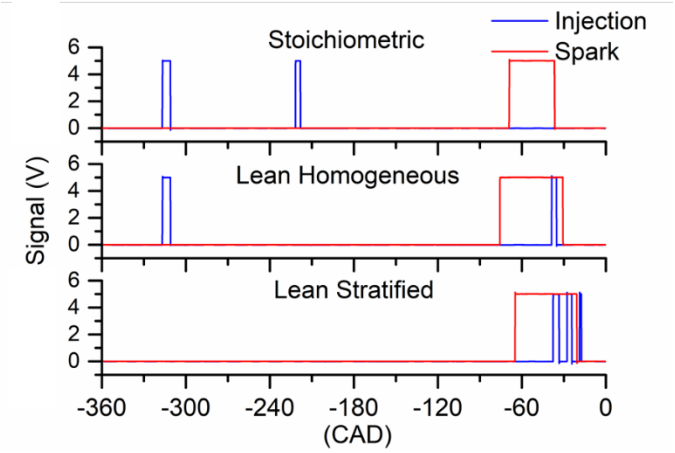

Figure 7: Representative injection strategy and spark timing versus crank angle degree (CAD) for the respective combustion modes

Ten steady state operating conditions were evaluated in this study and are shown in Table 2 with corresponding equivalence ratio. The steady state operating conditions included stoichiometric, lean homogeneous, and lean stratified operating modes. The full set of engine conditions was run once per day on three separate testing days to determine repeatability. These conditions were selected to be representative of common engine states during regulatory driving cycles with guidance from an industry project sponsor.

It has been shown that injector deposit formation has a strong impact on PN and PM emissions from GDI engines [107]. Fuel adsorption on the injector deposit results in diffusion flames; a known cause of particle emissions in GDI engines. Running the engine at high speed and high load can effectively burn off deposits and return the emissions to that from an engine with clean injectors. To attain repeatable particle emissions at a given

condition from test to test, each condition in the test matrix was run in the same specific order with the same amount of time (to the second) spent at each condition. This was implemented by an automated test plan during which all controllable engine and dynamometer parameters were compiled in spreadsheet with a specified time step for each condition. The data was then fed to a program that wrote the parameters to the engine and dynamometer controllers. A high speed/high load "de-coking" condition (2500 rpm 8 bar BMEP) preceded each set of engine mode operations (i.e., a high speed/high load condition before stoichiometric operation, a high speed/high load condition before lean homogeneous operation etc.) to burn off injector deposits and set a baseline engine state to proceed from.

Table 2: Engine conditions including operating mode and equivalence ratio

Condition	Speed (rpm)	BMEP (bar)	Mode	φ
SS 1	1400	2	S	1.0
	1400	2	LH	0.67
	1400	2	LS	0.5
SS 2	2000	4	S	1.0
	2000	4	LH	0.65
	2000	4	LS	0.65
SS 3	2000	7	S	1.0
	2000	7	LH	0.69
SS 4	2400	7	S	1.0
	2400	7	LH	0.73

An oxygenated 90.8 anti-knock index (AKI) fuel containing no additives was used for all testing. The fuel composition included 27% aromatics and 9.94% ethanol with properties including a T90 distillation temperature of 161.6 °C and research and motor octane numbers of 96.2 and 85.4 respectively.

3.3 Results and discussion

Figure 8 shows the average brake specific fuel consumption (BSFC) for each of the steady state conditions. At the low speed/low load condition of 1400 rpm 2 bar BMEP, the lean stratified operating mode showed a significant fuel efficiency advantage over the lean homogeneous and stoichiometric operating modes which can be attributed to the lower equivalence ratio ($\varphi = 0.5$). Specifically, there was an 8.6% and 19% reduction in fuel consumption at this speed load condition compared to the lean homogenous and stoichiometric modes respectively, and an 11% reduction in fuel consumption from stoichiometric to lean homogeneous. At the 2000 rpm 4 bar BMEP condition, the fuel efficiency was approximately equal for the lean operating modes which show a marginal increase in fuel efficiency compared to the stoichiometric mode. Note from Table 2 that the lean operating modes shared the same equivalence ratio at this speed and load condition. There was a slight advantage for the lean homogeneous mode at this condition that can be attributed to the earlier combustion phasing of the lean stratified case in which 50% mass fraction burned (MFB50) is at approximately top dead center as opposed to an ideal value for maximum brake torque of 7 CAD. The lean homogeneous 2400 rpm 7 bar condition had the lowest BSFC with 222 g/kWh corresponding to a brake thermal efficiency of 37.2% for E10 gasoline. No accessories were driven from the engine, so there were no parasitic losses. The efficiency would be slightly lower if the engine was driving an alternator, power steering pump, and mechanical water pump.

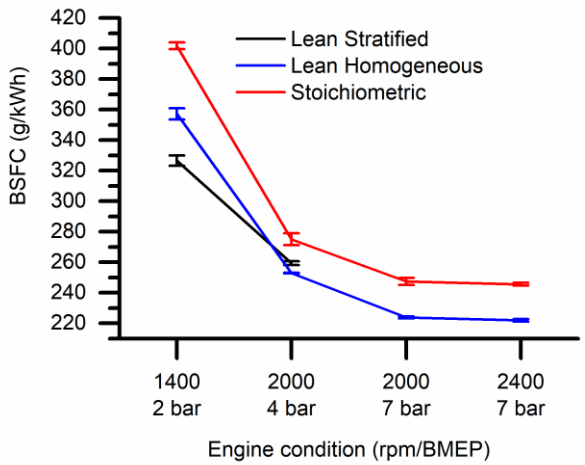

Figure 8: Average BSFC for the 10 steady state engine conditions. Error bars represent one standard deviation.

Figure 9 and Figure 10 show the brake specific SPN > 10 nm and brake specific soot concentrations for each of the steady state operating conditions respectively. The lean stratified operating modes emitted one to two orders of magnitude higher PN > 10 nm concentrations and two to three orders of magnitude higher soot concentration than the lean homogenous and stoichiometric modes at the respective conditions. The 2000 rpm 7 bar BMEP condition was the only case in which the lean homogeneous mode emitted more SPN > 10 nm than the stoichiometric mode. The soot emissions for the stoichiometric conditions were greater than that of the lean homogeneous conditions by a factor greater than that of the SPN > 23 nm emissions. This indicates the lean homogenous conditions produced a greater number of small particles.

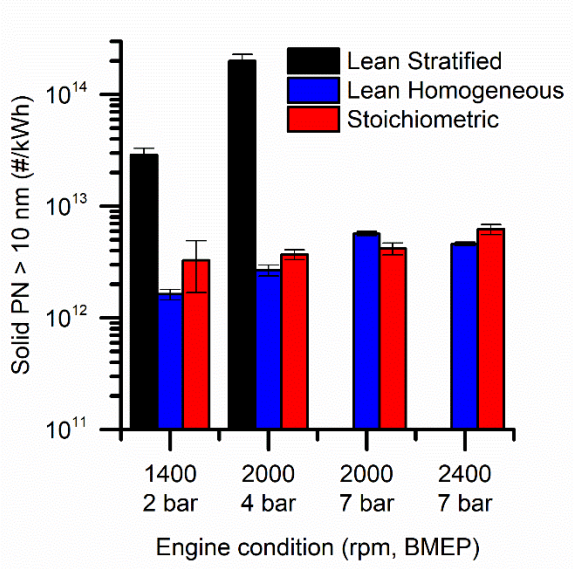

Figure 9: Average brake specific solid PN > 10 nm emissions as measured by EEPS for the 10 steady state engine conditions. Error bars represent one standard deviation.

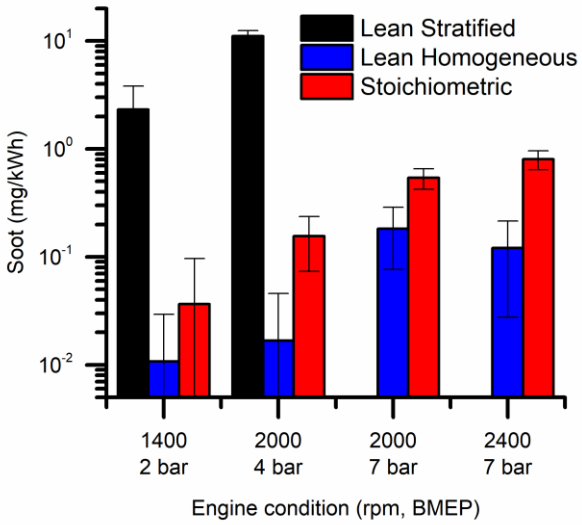

Figure 10: Average brake specific soot emissions as measured by MSS for the 10 steady state engine conditions. Error bars represent one standard deviation.

Figure 11 shows the fraction of solid PN > 10 nm between 10 and 23 nm, for each steady state condition. The stoichiometric 4 and 7 bar BMEP conditions had concentrations on the high end of what is reported in the literature. However, all lean homogeneous cases are dominated by SPN between 10 and 23 nm. It is presumed that the particles in this size

range are predominately composed of ash. This ash mode is likely highly sensitive to fuel and oil composition as well as engine oil consumption. The fraction of ash emitted in the nucleation mode range is also dependent upon the amount of soot present to scavenge ash. Thus, the lean stratified condition with its large soot modes is associated with a smaller fraction of tiny ash particles. Future work will look to confirm composition of these particles using the methods described by Apple et al. 2009 [108].

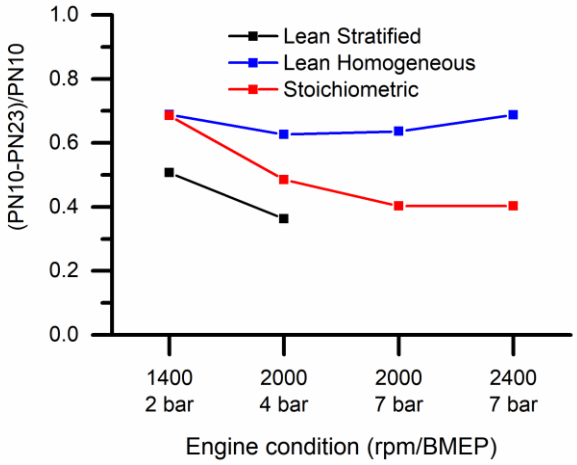

Figure 11: SPN > 10 nm fraction between 10 nm and 23 nm.

Figure 12 shows the average solid particle size distributions (PSD) for all the steady state conditions as measured using the EEPS instrument. As with all measurements taken for the steady state conditions, they are the average of three two-minute averages taken for each test with error bars showing the standard deviation between the three test averages. Thus, the error bars represent the repeatability of the tests rather than the stability of the emissions during the sampling period. Large accumulation modes present for the lean stratified conditions are consistent with the high soot mass measured by the MSS. The lean homogeneous and stoichiometric operating modes had very similar ash modes at 10 nm

except for the 1400 rpm 2 bar BMEP conditions, which were slightly lower than the other cases but still dominate their respective size distributions.

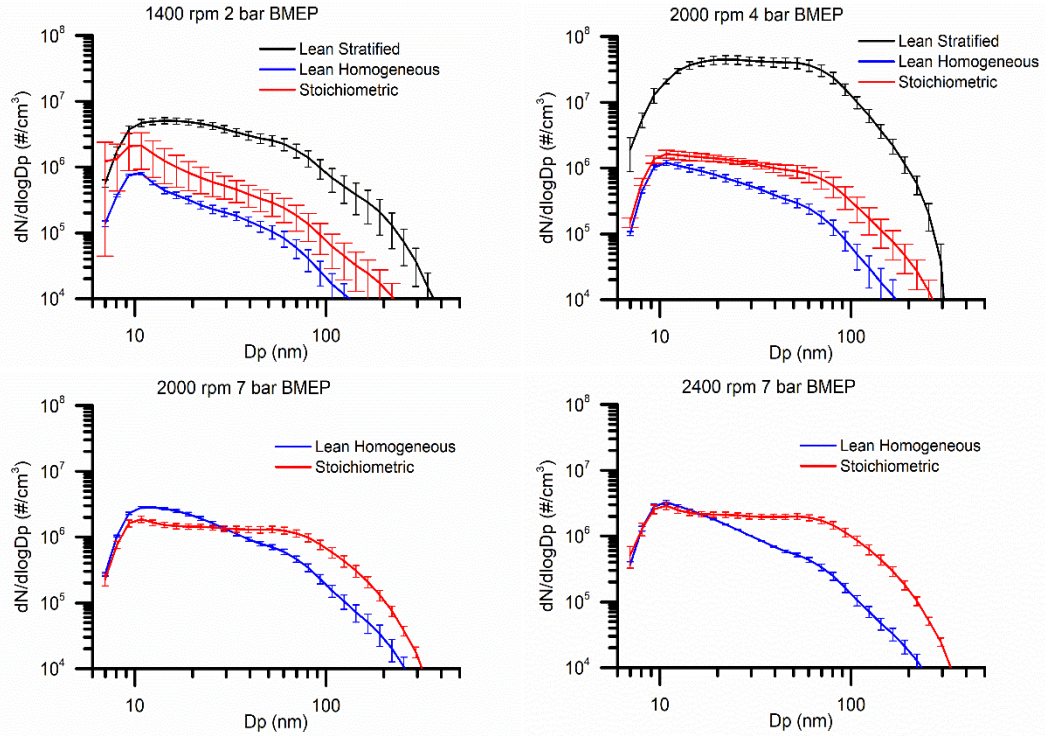

Figure 12: Solid particle size distributions for all engine conditions

Interestingly, the three higher speed and load stoichiometric conditions exhibited a very flat and broad PSD shape. The EEPS measurements were in good agreement with SMPS scans, not shown for brevity, taken at the same conditions. This flat distribution is not consistent with the well-recognized lognormal bimodal distributions traditionally associated with diesel and GDI engine combustion. This unusual feature may be characteristic of this engine model as Parks et al. reported similar size distributions from the same engine [109,110]. Ongoing work is aimed at understanding the formation mechanisms that underlie these results. The modal structure of diesel exhaust size distributions is associated with formation processes distinct in space and time. The soot mode is formed in a small number of rather well-defined burning fuel jets. It may be that

in the engine tested here, the temperature, composition histories of burning fuel packets are more heterogeneous, leading to a broader range of soot particle diameters.

Figure 13 shows the correlation between soot emissions measured by the MSS and PM emissions calculated from the EEPS volume measurement assuming a constant particle density of 0.7 g/cm^3. The results of a linear regression with the equation of the fit and R-squared value are shown for each mode. There is good agreement between the MSS and EEPS for the lean homogeneous modes. However, the MSS reported higher mass than the EEPS for all stoichiometric conditions, suggesting that the density estimate of 0.7 g/cc is too low for the stoichiometric conditions. This may be due to soot agglomerates with more compact structures for this mode. Conversely, the MSS reported lower mass than the EEPS for the lean stratified condition, suggesting that the density estimate was too high and that the soot particles from this mode are composed of more loosely packed core particles.

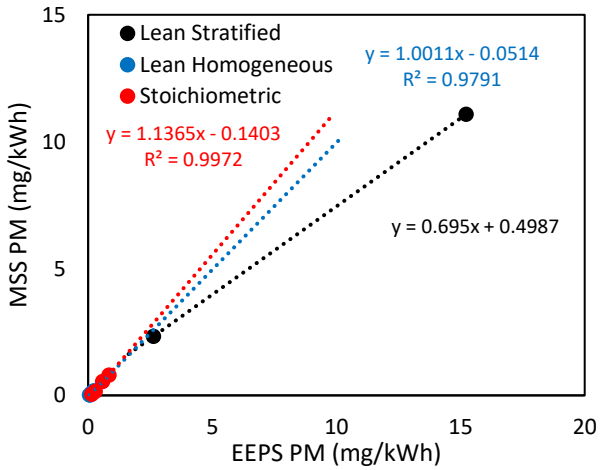

Figure 13: Correlation between MSS and PM calculated by EEPS.

Figure 14 shows the correlation between SPN and PM emissions calculated from the aerosol volume measured by the EEPS assuming constant particle density of 0.7 g/cm^3. Khalek et al. [17] reported a solid PN to PM ratio of 3.16 x 10^{12} with an R-squared value

of 0.957 for a stoichiometric GDI engine using an EEPS with a catalytic stripper, the same method used in this study. This line is shown in Figure 14 for reference. The results of the current study show a similar PN to PM slope of 2.51 x 10^{12} #/mg for the stoichiometric mode though, the regression shows poor correlation with a linear fit. This can be attributed to the large ash mode of the 1400 rpm 2 bar BMEP condition. When SPN > 23 nm was plotted against PM measured by the EEPS, the slope was 3.30 x 10^{12} #/mg with an R-squared value of 0.970, which is very close to that reported by Khalek et al.

Although the steady state stoichiometric cases have PN to PM ratios similar to those found in literature for GDI engines, lean combustion modes exhibited much higher ratios than the stoichiometric combustion modes, indicating a higher number of small particles per unit mass. This is confirmed by examination of the lean homogeneous PSDs, which exhibit a prevalent ash mode followed by a steep drop in concentration as particle size increases, and by the plot in Figure 11 showing the lean homogeneous mode had the highest fraction of particles between 10 and 23 nm. For the lean stratified case, this result can also be observed in the PSD of the 2000 rpm 4 bar BMEP condition, although it is subtler. The PSD of this condition is very flat between 20 and 100 nm before dropping very sharply at higher particle sizes where most of the aerosol mass exists. Additionally, the lean stratified modes may produce particles of lower density as was mentioned previously. Due to the limited number of lean stratified operating points examined in this study, the number to mass correlation for this combustion mode is less than definitive. Effective density measurements from each mode to confirm this is of interest for future work.

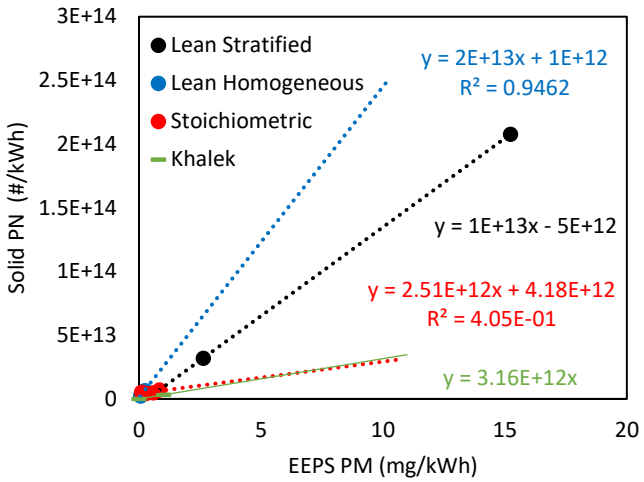

Figure 14: Correlation between SPN and PM calculated by EEPS compared to that of Khalek et al. for stoichiometric GDI [17].

Figure 15 shows the correlation of SPN > 23 nm and soot mass emissions measured by the MSS. Maricq et al. reported a PN to PM ratio of 2 x 10^{12} #/mg using a condensation particle counter (CPC) for PN measurement and a Dekati Mass Monitor for PM measurement [111]. This line is shown in Figure 15 for reference. When SPN > 23 nm was plotted against MSS PM, the slope was 3.09 x 10^{12} #/mg with an R-squared value of 0.939. Kirchner et al. reported a PN to PM ratio of 1.81 x 10^{12} #/mg for diesel exhaust particle emissions using an AVL APC489 for PN measurement and an MSS for soot mass measurement [112]. The stoichiometric number to mass ratio calculated using the EEPS and MSS is in good agreement with previous studies for PN > 23 nm, showing that the test engine has similar particle emissions characteristics to different GDI engines when the ash mode is neglected. However, it is apparent that lean combustion in the same engine results in more particles per unit mass than for stoichiometric modes.

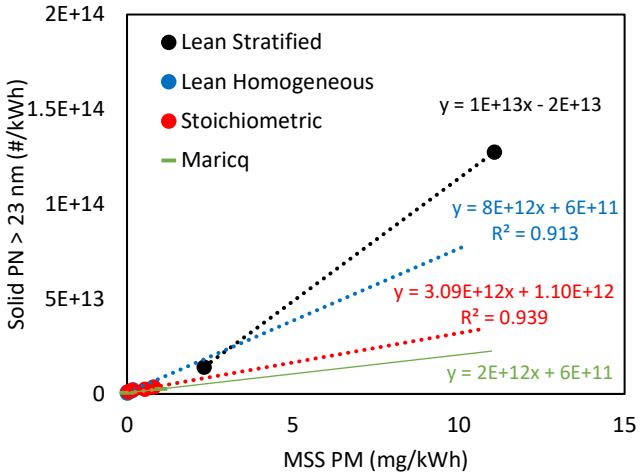

Figure 15: Correlation between SPN > 23 nm and soot emissions measured by MSS compared with the PN to PM reported by Maricq et al. for stoichiometric GDI [111].

Chapter 4 Effects of fuel properties on engine-out and GPF-out GDI PM emissions

This chapter discussed the effects of fuel properties on PM emissions from various GDI engine operating conditions. The chapter is broken down into 3 sections:

4.1 Effects of Fuel Properties on Particle Number and Particle Mass Emissions from Lean and Stoichiometric Gasoline Direct Injection Engine Operation

4.2 Influence of Fuel Properties on GDI PM Emissions over First 200 Seconds of WLTP Using an Engine Dynamometer and Novel "Virtual Drivetrain" Software

4.3 Effects of ethanol concentration on the effective density of GDI PM

4.1 Effects of Fuel Properties on Particle Number and Particle Mass Emissions from Lean and Stoichiometric Gasoline Direct Injection Engine Operation

With the effects of the various injection on PM emissions established using a baseline fuel, the effects of fuel properties were investigated under the same engine conditions (stoichiometric, lean homogeneous, and lean stratified). Fuel property effects on GDI PM has recently been extensively study, however, little to no published research exists on fuel property effects using non-conventional lean combustion modes, like the ones described here. This work was previously published in a conference paper [113].

4.1.1 Experimental

Seven different fuel formulations were tested in the current study to determine the impact of fuel physical properties and chemistry on particle emissions from the three different GDI combustion modes. None of the fuels contained a detergent additive package. The fuels tested are shown in Table 3 with their fuel identification name, aromatic

concentration, the distillation temperature T90, the octane number, the ethanol concentration, and the calculated PM Index based on ref [15]. The distillation temperature T90 is defined as the temperature at which 90% of the fuel would evaporate during a temperature ramp. All fuels except the baseline fuel were analyzed by gas chromatography-mass spectrometry (GC-MS) to quantify the concentration of more than 300 chemical species. With this analysis, PM Index was calculated for each component present in concentrations greater than 0.1 wt. %. The vapor pressure at 443 K was calculated for each component using the correlation with boiling point described by Aikawa et al. [15].

Table 3: Fuel property data and PM Index (PMI)

Fuel ID (-)	Aromatics (%)	T90 (°C)	EtOH (%)	RON/MON (-)	PMI (-)
Baseline	27.0	162	9.9	96.2/85.4	NA
A-1	22.4	160	9.9	95.2/86.5	1.2
A-2	42.9	166	9.9	97.9/87.3	1.8
V-1	29.4	129	9.9	95.1/86.5	0.7
V-2	29.4	187	10.0	96.2/87.2	2.2
E15	28.5	160	15.2	99.1/88.0	1.4
E50	16.7	160	50.0	103.8/88.8	1.1

The distillation curves for each of the analyzed fuels are shown in Figure 16. The most notable feature is the flat section of the E50 fuel from 30% to 80% at ~ 78 °C corresponding to the boiling point of ethanol. Another feature worth noting is that the high aromatics, A-2, and the low volatility fuel, V-2, have nearly identical distillation curves up to 80% volume evaporated, at which point they diverge. All fuels except the low volatility fuel, V-2, have approximately the same T95 temperatures, which were between 171 °C and 176 °C.

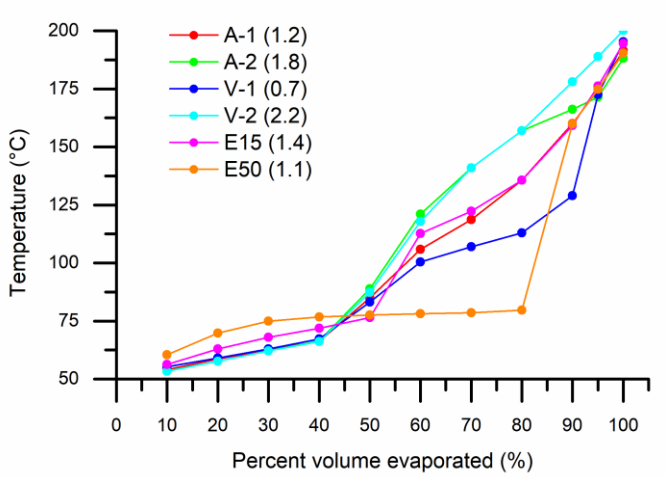

Figure 16: Distillation curves for each of the fuels analyzed

The test engine used in this study was the same as the one previously described in Chapter 3, but with the addition of a catalytic GPF with a three-way catalyst (TWC) washcoating. The engine was operated under the same testing conditions listed in Table 2 of Chapter 3. One fuel was tested per day at each of the engine conditions with a total of three rounds of fuel testing performed (1 fuel test per day x 7 fuels x 3 rounds of testing = 21 testing days). For the first round of testing, the fuels were tested in the order in which they appear in Table 3. In the second round of testing, the fuels were tested in the reverse order. In the third and final round of testing, the fuels were tested in a randomized order, provided no two fuels were tested in the same order as in the first or second round of testing. Between each day of testing (i.e. between each fuel tested) the fuel injectors were removed from the engine and the tips were submerged in an ultrasonic cleaner bath of ethanol to remove the injector deposits from the tips. This was done in effort to eliminate the injector fouling propensity of one fuel from influencing the PM emissions of the subsequent fuel tested. Before each round of testing, the lubrication oil was changed to reduce any effects that may have arisen due to oil degradation or oil dilution throughout the testing campaign.

After the oil was changed, it was conditioned for 18 hours using the steady state conditions to reduce any effect caused by fresh oil.

The order in which the engine conditions were tested, and the duration spent at each of the engine conditions was identical for each test day using an automated engine controller program. This was done in effort to promote repeatability. Each engine condition was run for 15 minutes, except for the LS1 condition which was run for 45 minutes. A GPF regeneration condition was run for 2 minutes after each condition so that each condition would begin with a clean GPF for GPF loading comparisons between engine conditions and fuels. The stoichiometric conditions were run first in the order: S2, S3, S1, S4; then, the lean homogeneous conditions were run in the order: LH2, LH3, LH1, LH4; and lean stratified conditions were run last in the order: LS2, LS1.

The emissions sampling system and measurement instrumentation are shown in Figure 17. It is essentially the same as the sampling system used in the previous study, with the addition of a catalytic GPF and a second EEPS and CS to measure post-GPF particle size distributions. Emissions for each engine condition were averaged over a five- minute period after a ten-minute stabilization time at that condition. As each fuel was tested three times, all emissions reported are the mean of those three, five-minute averages with error bars representing the standard deviation from the mean of the three, five-minute averages.

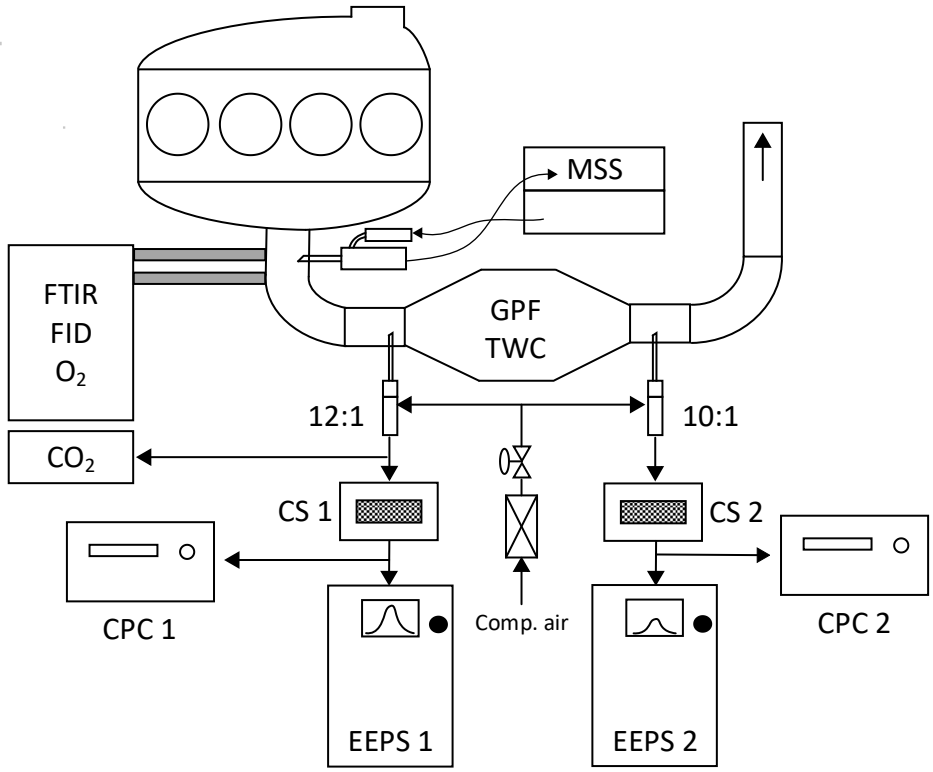

Figure 17: Engine and instrumentation schematic showing dilution system and instruments used in the experimental study

4.1.2 Results and discussion

Figure 18 shows the engine-out particle size distributions for the lean homogeneous conditions at each engine condition and for each fuel. The fuel ID is listed in the legend with the PM Index of that fuel in parentheses. As with all emissions to be reported, the particle size distributions represent the mean of three, five-minute averages taken on the three different test days for each fuel. The error bars are standard deviation of that mean, and thus represent the day-to-day repeatability of the engine condition and fuel.

The high ethanol content fuel (E50) repeatably produced the highest PM emission for three of the four engine conditions in the lean homogeneous mode. For the LH1 condition, the E50 distribution is similar to that of the other fuels, with a large 10 nm solid nucleation mode and a moderate accumulation mode. At the LH2 condition, the E50 fuel produced

significantly lower PM emissions than any other fuel. All other fuels produced similar distributions and concentrations at this condition. However, at the two higher load lean homogeneous conditions, LH3 and LH4, the E50 fuel produced almost an order of magnitude higher accumulation mode concentrations than any other fuel. This is likely a consequence of the late injection employed by the lean homogeneous mode coupled with the high heat of vaporization (HOV) of ethanol. Because of the greater fuel demand at the higher load conditions, a large quantity of fuel is injected in the late injection and there is not enough time or enough heat in the cylinder to fully vaporize the fuel prior to combustion. The ethanol is not the source of the high concentration of accumulation mode particles. Rather the high HOV of the ethanol in the fuel inhibits the evaporation of the fuel, leaving the remaining fuel components with high sooting tendencies in the liquid phase or as highly rich vapor regions as combustion commences.

It can be seen from the particle size distributions that the magnitude of the solid nucleation mode, near 10 nm, trends with the magnitude of the accumulation mode. The 10 nm mode particles are thought to be composed of ash derived from metallic lubrication oil additives. It could be expected that, if the formation of these 10 nm ash particles occurred independently from the mechanism through which the accumulation mode soot particles were formed, the large accumulation mode particles would scavenge the ash particles and the two modes would be inversely related. Since this is not the case, the mechanisms responsible for the formation of these two modes are likely related; namely, wall-wetting induces the formation of both the solid nucleation mode and the accumulation mode. Fuel impingement on cylinder surfaces would dissolve oil films, reducing the viscosity and surface tension of the film, and encourage the ejection of oil droplets from

the cylinder wall or piston ring. When the oil is burned during combustion, the metallic ash remains suspended in the gas and forms the 10 nm ash particles. Wall wetting would also produce soot forming diffusion flame pool fires, resulting in accumulation mode particles, thus linking the formation of the two modes.

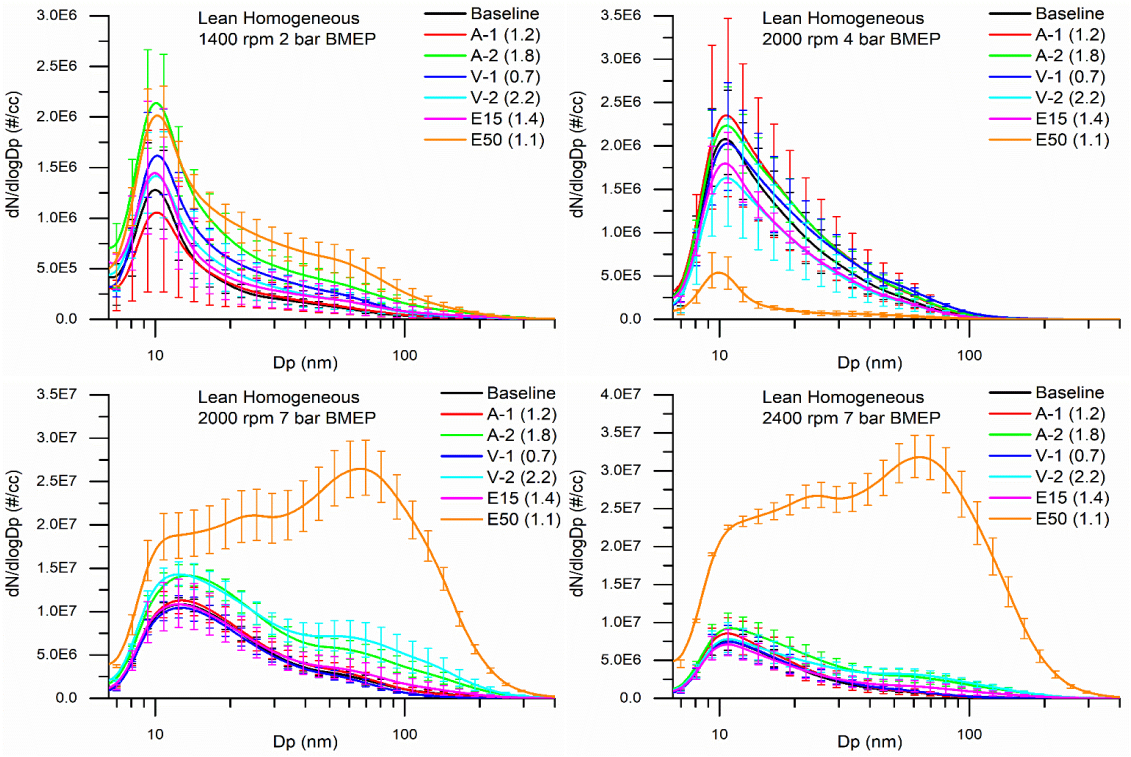

Figure 18: Engine-out particle size distributions for the lean homogenous combustion mode at the four different engine conditions for each of the seven fuels tested. From top left to bottom right: LH1, LH2, LH3, and LH4.

Wall wetting has also been linked to low-speed pre-ignition (LSPI), which is currently a major obstacle for highly boosted, down-sized engines [114–118]. The mechanism linking wall wetting to increased occurrence of LSPI is the same mechanism that links wall wetting to increased ash particle emissions. When fuel impinges on the cylinder wall, the oil is diluted, and oil droplet detachment is likely. The oil droplet then auto-ignites, initiating combustion prior to the spark event. The link between wall wetting, accumulation

mode particles, solid nucleation mode ash particles, and LSPI allows for the opportunity to utilize a synergistic approach to reduce the greatest barriers to GDI technology advancement. In other words, investigating injection strategies that minimize wall wetting and ash particle emission will have the added benefit of reducing the occurrence of LSPI.

When PN and PM mass concentrations were examined at the LH3 and LH4 conditions and the E50 fuel was omitted, the PN and PM mass emissions correlated well with the fuel PM Index. Figure 19 and Figure 20 show the correlation between PN and the PM Index and PM mass and the PM Index for the LH3 condition respectively. The same can be seen for the LH4 condition in Figure 21 and Figure 22. PN and PM mass emissions from the lower load lean homogeneous conditions, LH1 and LH2, showed little to no correlation with the PM Index. The R square values for the LH1 and LH2 conditions were less than 0.1 and are not shown here for conciseness. These lower load lean homogeneous conditions appear relatively insensitive to fuel formulation.

Note the magnitude of the lean homogenous PSDs. The higher load conditions are approximately an order of magnitude greater than the lower load conditions. The strong correlation between the PM Index and PN and PM mass emitted from the high load lean homogenous conditions indicate that fuel properties play a larger role in PM formation under engine conditions which produce higher particle concentrations. This can be explained by the nature of the charge composition. If the charge mixture is homogenous and lean or stoichiometric, fuel properties will have limited impact on particle formation because combustion of a homogenous mixture will result in little incomplete combustion and pyrolysis of the fuel components, regardless of the fuel composition. By comparing the PSDs of the lower load and higher load lean homogenous conditions, it could be

assumed that the lower load conditions produce a homogeneous and near stoichiometric charge mixture near the spark plug within a globally lean mixture, resulting in relatively low particle formation. However, at the higher load conditions with a greater quantity of fuel delivered in the late injection, a rich region remains at the start of combustion resulting in fuel pyrolysis and soot formation. Under these conditions, the fuel effect is seen; the high aromatics fuel and low volatility fuel produce a marked increase in PM emissions compared to the other fuels. In the case of the E50 fuel, it is possible that liquid droplets remain at the start of combustion due to the high quantity of high HOV fuel injected. This leads to the distinctly different PSD of the E50 fuel at the higher load conditions.

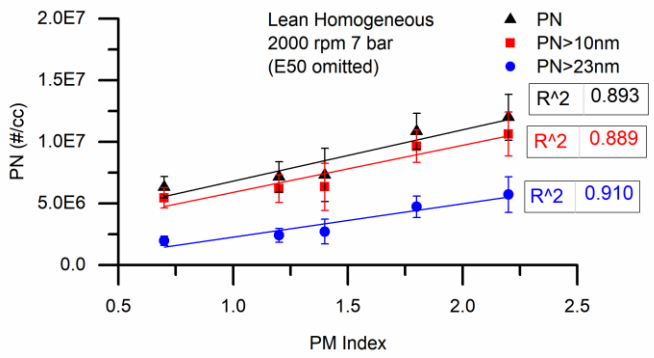

Figure 19: Correlation between PN and the PM Index for the lean homogenous combustion mode at the 2000 rpm 7 bar BMEP engine condition with the E50 fuel omitted

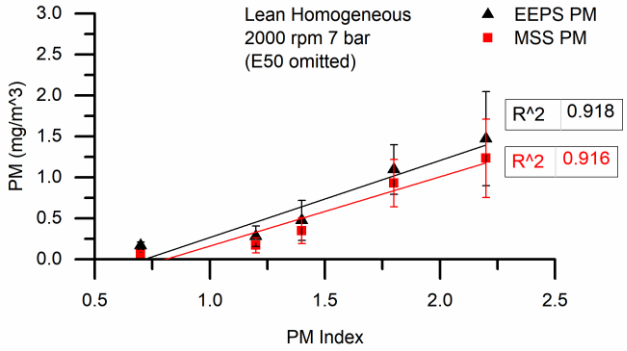

Figure 20: Correlation between PM mass and the PM Index for the lean homogenous combustion mode at the 2000 rpm 7 bar BMEP engine condition with the E50 fuel omitted

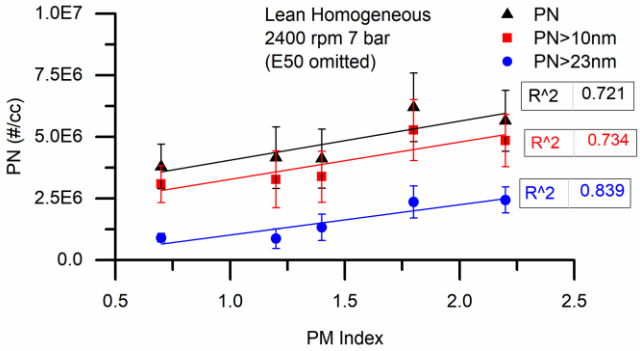

Figure 21: Correlation between PN and the PM Index for the lean homogenous combustion mode at the 2400 rpm 7 bar BMEP engine condition with the E50 fuel omitted

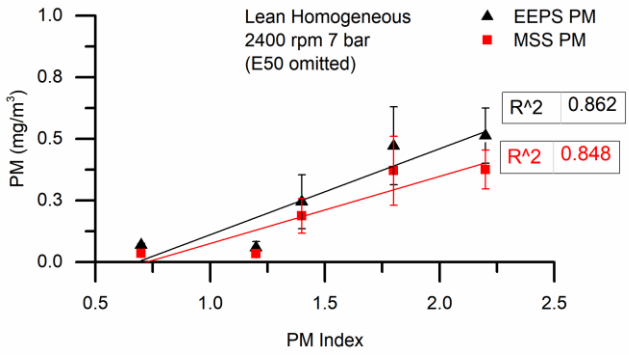

Figure 22: Correlation between PM mass and the PM Index for the lean homogenous combustion mode at the 2400 rpm 7 bar BMEP engine condition with the E50 fuel omitted

Figure 23 shows the engine-out solid particle size distributions for the lean stratified conditions for each fuel. Apart from the high aromatics fuel, V-2, at the LS1 condition and the E50 fuel at both conditions, all fuels produced similar particle size distributions. The A-2 fuel exhibited an increase in PM concentration over the 45-minute test segment of the LS1 condition that did not occur at the same rate from test to test, which accounts for the large variability seen in the particle size distribution from run to run. The E50 fuel produced significantly lower PN and PM mass emissions than any of the other fuels. At these conditions, the ethanol effect of diluting the soot forming aromatics appears to have been dominant, and the effect of the delayed evaporation caused by its high HOV was reduced due to the low fuel quantity injected.

The high particle concentrations found in the lean stratified conditions contrast with what was observed for the high load lean homogenous conditions where high particle concentrations correlated with the PM Index. An explanation for this, again, requires investigation of the charge composition. Because the lean stratified conditions deliver all of the fuel in close temporal proximity to the spark event, the charge mixture is highly stratified. Under these conditions, it is possible that liquid fuel droplets survived evaporation prior to combustion for all the fuels. This would result in droplet burning and pyrolysis of the fuel comprised within the droplet leading to similar particle formation events for each fuel, except for the E50 fuel. It is clear from the sharp drop in the E50 distillation curve (Figure 16) that all of the components below T90 are ethanol and components with lower boiling points than ethanol. The comparatively low particle concentrations for the E50 fuel for the lean stratified conditions may be a result of pyrolysis of the 10% of the fuel components with higher boiling points than that of ethanol. The other

fuel formulations have significantly higher concentrations of low volatility and/or high aromaticity components in the range from T60 to T90 which may be contributing to the observed high particle concentrations by droplet burning and/or flame propagation through rich vapor regions.

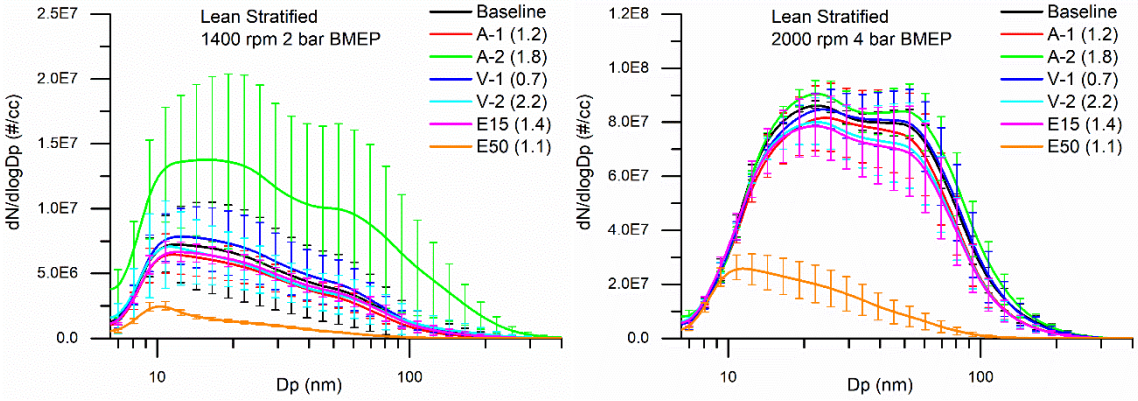

Figure 23: Engine-out particle size distributions for the lean homogenous combustion mode at the two different engine conditions for each of the seven fuels tested

Figure 24 shows the difference between a clean injector tip before testing and dirty injector tip after one run of fuel testing. These deposits develop when liquid fuel remains on the injector tip as combustion proceeds. Because the liquid fuel cannot be oxidized, it undergoes pyrolysis, leaving behind carbonaceous deposits. Fuels without deposit control additives cause excessive deposit formation [119–121]. Injector deposits may have influenced the results of the lean stratified conditions, which were tested last after the stoichiometric and lean homogeneous conditions. If fuels with lower PM Index resulted in increased rate of injector deposits, the PM emissions could have been similar for each fuel as a result of this, after some deposits had formed. However, because all fuels showed approximately the same concentrations for the lean stratified conditions (except E50 and A-2 for LS1), the injector deposit formation rate would have to be inversely and proportionally related to the PM Index, which seems unlikely. It is more likely that the

highly stratified nature of lean stratified mode caused liquid fuel droplets to remain for all fuels; i.e., all the fuels have low enough volatility that this occurs.

Figure 24: Clean injector tip (left) and dirty injector tip (right)

Figure 25 shows the solid engine-out particle size distributions for the stoichiometric conditions for each fuel. The first aspect to note is the low particle concentrations. The stoichiometric conditions produced orders of magnitude lower concentrations than the lean conditions. Because the stoichiometric conditions were the first to be tested each run, and the injectors began each run clean, there were little to no injector deposits present for these conditions. In the work of Chapter 3, testing the same conditions with the baseline fuel and no injector cleaning, the stoichiometric conditions produced flat distributions on the order of 1E6 #/cc [104]. It is evident that the PM emissions seen in that work were a result of injector fouling, as the stoichiometric conditions in this work generally produced accumulation mode concentrations around 1E5 #/cc. Injector deposits disrupt the fuel spray distribution leading to poor fuel atomization which leads to larger fuel droplets which do not evaporate as readily, resulting in diffusion flames or flame propagation through rich

vapor regions. Injector deposits, composed of carbonaceous material, also allow a porous surface on which fuel can adsorb, leaving liquid droplets or rich fuel regions that result in fuel pyrolysis and soot formation. Under these conditions, the fuel volatility and aromaticity effects may be exacerbated; however, with clean injectors and a homogeneous stoichiometric mixture, the fuel has little influence as the charge mixture is nearly ideal. It appears that the injector deposits seen in Figure 24 formed under the lean conditions, because the last stoichiometric condition tested, S4, has an order of magnitude lower accumulation mode particle concentrations than when tested with uncleaned injectors.

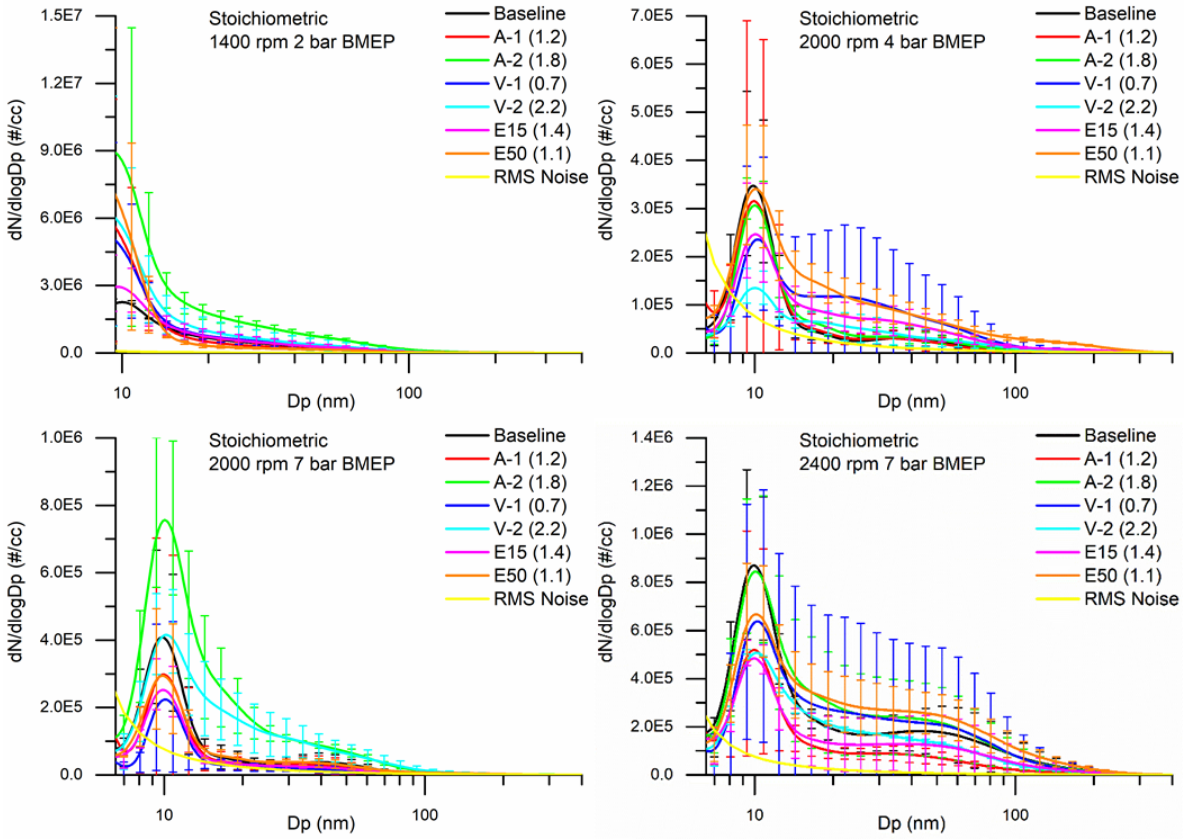

Figure 25: Engine-out particle size distributions for the stoichiometric combustion mode at the four different engine conditions for each of the seven fuels tested

In the absence of injector deposits, the stoichiometric particle size distributions exhibited a large solid nucleation mode and a modest accumulation mode. For many of the

particle size distributions, the particle concentrations were close to the noise level of the EEPS (shown in Figure 25 and corrected for dilution and CS loss). As particles deposit on the electrometer column of the EEPS, the offset and noise level of those electrometer channels increase, and the accuracy of the particle concentration calculation decreases. This is not an issue at higher particle concentrations where the signal-to-noise ratio is much higher. However, this could explain the high level of variability in the concentrations, specifically of the 2000 rpm, 4 bar BMEP condition (S2).

At low particle concentrations, a small perturbation event has a significant impact on the total fraction of particle production. For example, a low level of injector fouling on one of the injectors that occurred during one run and not the others would present itself as a large difference in particle concentration. To that point, it was observed that the high volatility fuel, V-1, caused injector deposits that required additional cleaning time to remove compared to the other fuels. This fuel also had largest variability for the S2 and S4 conditions. Ultimately, because the particle concentrations are so low from stoichiometric conditions with clean injectors, these small effects should be of little concern in regard to regulatory compliance. However, these results demonstrate the reduction in particle emission that can be attained with clean injectors.

The S1 condition showed particularly high solid nucleation mode particle concentrations. At this low speed and load, there is likely poor charge motion which would allow greater fuel spray penetration and increased wall wetting, leading to higher ash particle concentrations.

Figure 26 and Figure 27 show the correlation of PN and PM mass to the fuel PM Index for the S3 condition. This was the only stoichiometric condition to show any correlation

between PN/PM mass and the PM Index. This is simply a result of the high volatility fuel (V-1) producing the lowest particle concentrations and the low volatility fuel (V-2) and high aromatic fuel (A-2) producing the highest particle concentrations. The other three fuels did not produce PN or PM mass concentrations statistically different than one another. Note the exceptionally low PM mass concentrations shown in Figure 27. These concentrations are near the background noise of the instrument (below 0.01 mg/m^3 with 10:1 dilution).

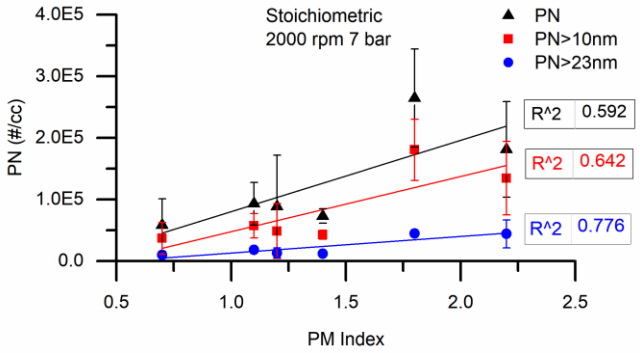

Figure 26: Correlation between PN and the PM Index for the stoichiometric combustion mode at the 2000 rpm 7 bar BMEP engine condition

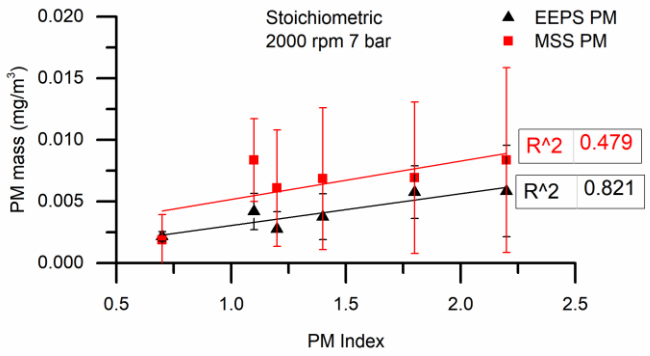

Figure 27: Correlation between PN and the PM Index for the stoichiometric combustion mode at the 2000 rpm 7 bar BMEP engine condition

4.1.3 GPF Filtration Efficiency

Figure 28 shows size-resolved filtration efficiency as a function of soot mass entering the GPF per filter substrate volume. The incoming soot was calculated using the MSS volumetric soot mass concentration and the volumetric exhaust flow rate. The filtration efficiency was calculated using the pre- and post-GPF particle size distributions measured by the EEPSs and is defined as $1 - PN(Dp)_{out}/PN(Dp)_{in}$ for all particle sizes. The most penetrating particle size (MPPS) for the GPF was between 100 and 150 nm. Particles smaller than that were efficiently trapped by diffusion, and particles larger than that were efficiently trapped by impaction and interception.

For the LS1 condition, the filtration efficiency reached over 95% at the MPPS with a soot loading 14 mg/L. The LS2 condition reached over 90% at the MPPS with 42 mg/L. The LH3 condition reached a similar filtration efficiency with 50 mg/L, and the LH4 condition only exceeds 70% at 50 mg/L. The main difference between these conditions is exhaust temperature and flowrate.

Comparing LS1 and LS2 at 14-15 mg/L, the filtration efficiency at 100 nm was ~95% for LS1 and ~70% LS2, and the GPF outlet exhaust temperature for was 235 °C for LS1 and 386 °C for LS2. The difference in these conditions is largely due to the difference in flowrate. At a volumetric flowrate ~2.25 times higher than that of the LS1 condition, the LS2 condition had much higher penetration due to the higher space velocity, resulting in less time for diffusion filtration. This can be seen by the initial clean filter efficiency at the MPPS. There is much greater penetration at MPPS for the LS2 condition compared to the LS1 condition. There is likely very little to no soot oxidation occurring at this condition.

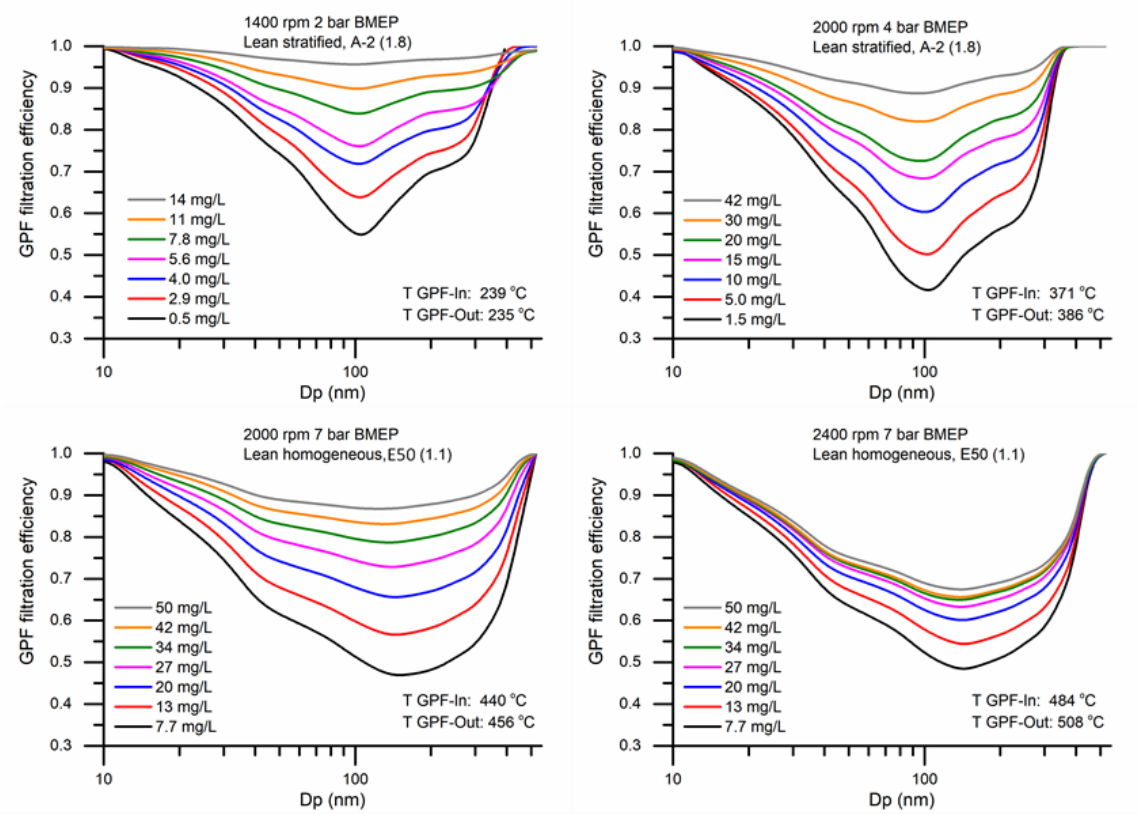

Figure 28: Size-resolved GPF filtration efficiency as a function of non-oxidized soot mass loading on the GPF per GPF volume for the A-2 and E50 fuels

Comparing the LH3 and LH4 conditions, results indicate soot oxidation occurring on the filter for the LH4 condition. These conditions are at the same load, and the exhaust flowrates are much closer to each other than those of the LS1 and LS2 conditions (only 26% higher for LH4). The LH3 and LH4 conditions have approximately the same filtration efficiencies at a soot into filter loading of 7.7 mg/L. However, the filtration efficiency of the LH4 condition stops increasing after about 30 mg/L into the filter. This indicates that the filter is no longer trapping soot and building a soot cake because the rate of soot oxidation is equal to the rate that soot is trapped on the filter. It should be noted that for conditions in which the GPF outlet exhaust gas temperature was greater than the inlet, CO

and HC conversion occurred on the catalyst, and the internal substrate temperature was likely higher than the outlet temperature.

The soot oxidation initiation temperature has been shown to occur near 400 °C, though the oxidation rate at this temperature is very low [122,123]. These rates, however, become significant above 500 °C. This supports what was observed in the GPF loading and filtration efficiency behavior. It should be noted that all these conditions are lean, therefore the exhaust provides an abundance of oxygen to convert the soot. Additionally, the GPF is wash-coated with a catalyst, which may contribute to soot oxidation reaction rates.

4.2 Influence of Fuel Properties on GDI PM Emissions over First 200 Seconds of WLTP Using an Engine Dynamometer and Novel "Virtual Drivetrain" Software

4.2.1 Motivation

Vehicles are certified to meet regulatory emission and fuel economy standards through driving cycle tests. Driving cycle testing is conducted with a vehicle on a chassis dynamometer, also known as a rolling dyno, with the vehicle following a prescribed speed trace of a regulatory driving cycle that approximates real-world driving. Emissions and fuel consumption are measured over the cycle to determine compliance. Thus, determining if a vehicle meets regulatory compliance requires a fully assembled vehicle. Because engine testing and calibration early in the development process is conducted on an engine dynamometer, testing driving cycles with an engine dynamometer could reduce the time required for in-vehicle calibration on a chassis dynamometer and in real world tests. Testing driving cycles on an engine dynamometer would allow engine control strategies and aftertreatment components to be modified before final vehicle assembly.

Testing driving cycles with an engine dynamometer requires a model of drivetrain components and vehicle specifications in order to operate the engine as if it was in a vehicle performing in the vehicle itself on the road. Literature review yielded few published works on testing driving cycles using an engine dynamometer. Kęder et al. proposed an engine dynamometer test stand for driving cycle simulation [124]. The authors outlined all necessary hardware and software, including a vehicle model, that would allow operation of an engine on an engine dynamometer as though it were operating in a vehicle performing a driving cycle. However, no experimental engine data were presented, so it is not known whether the system was successful at completing its objectives. In a master's thesis by Androne and Rao, a hardware-in-loop methodology was applied to an engine dynamometer and vehicle model to operate and engine over a the World-harmonized Light-duty Test Procedure (WLTP) and NEDC driving cycles [125]. They were able to control the engine to match calculated vehicle speed within 2 km/hr. of the driving cycle speed traces and showed comparable fuel consumption and CO_2 emissions to the engine in a vehicle running the driving cycles on a chassis dynamometer.

No previous published work was found on PM emissions from an engine on an engine dynamometer operating over a driving cycle. With PM emissions characterized for the test engine at steady state conditions with various fuel and combustions strategies, determining the impact of fuel properties on engine-out and GPF-out PM emissions of a GDI engine operating over critical portions of a relevant driving cycle was desired.

4.2.2 Experimental

A virtual drivetrain model was designed in LabView software to control the dynamometer in such a way that the engine would behave as if it were connected to a

transmission in a vehicle. A schematic/flowchart of the virtual drivetrain, the driving cycle controller, and the engine hardware are shown in Figure 29. The virtual drivetrain inputs were brake torque, engine speed, virtual gear "vGear", virtual brake "vBrake", and vehicle specifications to calculate an instantaneous acceleration. The drivetrain model loop was executed with a specified Δt value of 100 ms. Then, the calculated acceleration is multiplied by Δt to calculate the change in vehicle speed over the time step, which is added to the previously calculated vehicle speed, to obtain the new calculated vehicle speed. To determine vehicle acceleration, the net road force is calculated using Eq. 4.1.

$$F_{road} = F_{driveline} + F_d + F_{rr} + F_{brake} \quad \text{Eq. 4.1}$$

where F_{road} is the net road force, F_{drive} is the driveline force produced by the engine, F_d is the aerodynamic drag force, F_{rr} is the rolling resistance, and F_{brake} is the braking force. The driveline force produced by the engine is the product of the brake (crank) torque, the current gear ratio, the final drive ratio, the driveline efficiency, and the inverse of tire radius. The calculation for the driveline force is calculated using Eq. 4.2.

$$F_{driveline} = \tau_{crank} R_g R_{fd} \eta_{driveline} {r_{tire}}^{-1} \quad \text{Eq. 4.2}$$

where τ_{crank} is the crank torque produced by the engine, R_g is the gear ratio of the current gear, R_{fd} is the final drive ratio, $\eta_{driveline}$ is the driveline efficiency, and r_{tire} is the tire radius. The aerodynamic drag force is calculated using equation Eq. 4.3.

$$F_d = -\frac{1}{2} C_d \rho {V_{vehicle}}^2 A_f \quad \text{Eq. 4.3}$$

where C_d is the drag coefficient of the vehicle, ρ is the air density, $V_{vehicle}$ is the vehicle velocity, and A_f is the frontal area of the vehicle. The rolling resistance force is calculated

as the product of the coefficient of friction for the tires and road, C_f, the mass of the vehicle, m, and the acceleration due to gravity, g. The equation for the rolling resistance force is given by Eq. 4.4.

$$F_{rr} = -C_f mg \quad \text{Eq. 4.4}$$

The vehicle acceleration was calculated as the ration of the road force over the mass of the vehicle. The equation for vehicle acceleration, $a_{vehicle}$, is given as Eq. 4.5.

$$a_{vehicle} = \frac{F_{road}}{m} \quad \text{Eq. 4.5}$$

The vehicle velocity was calculated by adding the previous vehicle velocity, $V_{vehicle,o}$, to the product of the vehicle acceleration and loop execution time, Δt, and is shown in Eq. 4.6.

$$V_{vehicle} = V_{vehicle,o} + a_{vehicle}\Delta t \quad \text{Eq. 4.6}$$

A set of shift matrices within the virtual drivetrain controlled what virtual gear (vGear) the vehicle was in. The shift matrix inputs were engine speed and load, then it was determined if an "upshift" or "downshift" was required based on engine speed and percent load. There were unique shift matrices for gears 1,2, and 3-6. The virtual brake (vBrake) was a variable in the virtual drivetrain model representing a braking force from 0-10 kN. When the vBrake was be applied, the total road force became negative, which decreased the calculated vehicle speed, and thus the engine speed until a downshift was determined to be required. The driving cycle controller was a PID controller that took calculated vehicle speed and desired vehicle speed as inputs and output a signal to the throttle or the vBrake to either increase or decrease the vehicle speed. The set of described components

allowed the engine to operate over any predefined vehicle speed trace as if it were in a vehicle performing the speed trace.

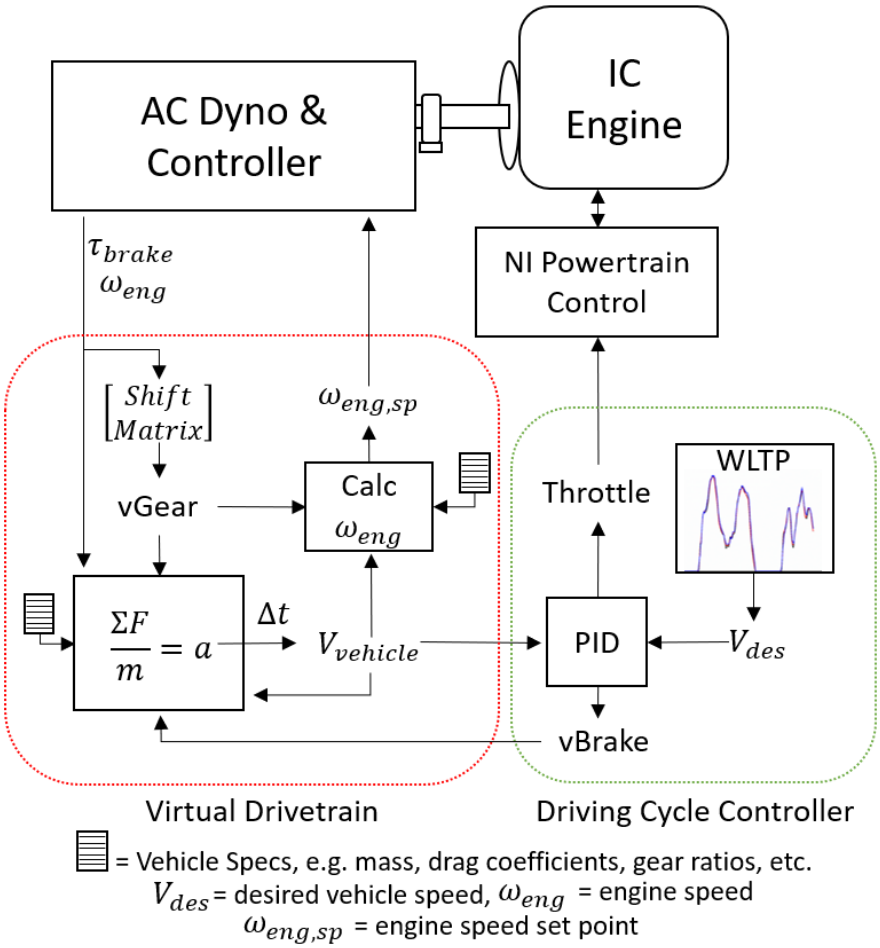

Figure 29: Schematic of virtual drivetrain, driving cycle controller and engine hardware

The first 200 seconds of the WLTP cycle was selected for evaluating PM emissions. This portion of the driving cycle is the most problematic for PM emissions due to cold start and cold drive off. Each fuel was tested under this portion of the driving cycle three times. The GPF was regenerated before each fuel was tested, so each fuel test started with a clean filter. The GPF loaded over the course of three runs for a specific fuel before it was regenerated for testing the next fuel. The engine was cold soaked before after each test such that all engine components were at ambient temperature (~20° C) before starting the next

test. The fuel system and engine were purged and flushed with new fuel prior to starting the testing the next fuel test. The same engine and exhaust sampling system were used as in the previous section.

4.2.3 Results and Discussion

Vehicle driving cycle data was provided by an automotive partner for a vehicle with a similar displacement, a naturally aspirated engine operating over the WLTP cycle on a chassis dynamometer. Vehicle speed traces are shown in Figure 30 for the target speed of the WLTP, the simulated vehicle speed using the virtual drivetrain and engine dynamometer, and for a medium sized vehicle on the chassis dynamometer. The maximum deviation from the speed trace for the engine dynamometer was less than 1 mph and the average deviation over the test was less than 0.1 mph. This is well within the test procedure speed deviation limit of less than 2 km/hr.

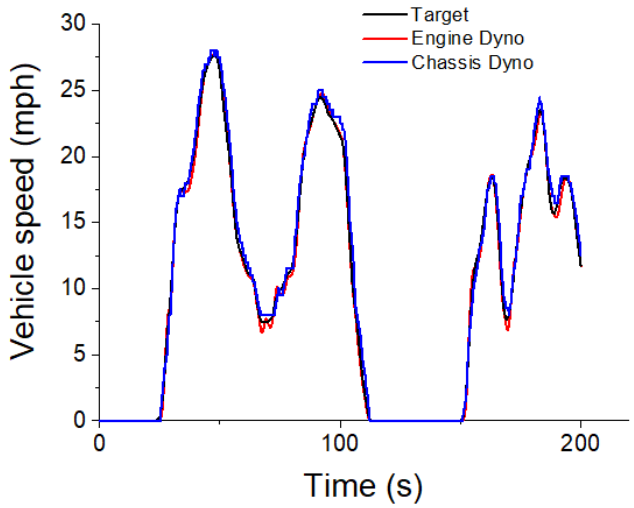

Figure 30: Simulated vehicle speed versus time over the first 200 seconds of the WLTP cycle compared to the manufacturer-provided data and the prescribed target speed for the cycle.

Figure 31 shows the test engine torque and speed compared to the engine in the vehicle over the first 200 seconds of the WLTP cycle. The speed and torque traces of the BMW

test engine were comparable to that of the actual vehicle. The torque output for the chassis dynamometer vehicle is a calculated crank toque from an ECU lookup table, which is likely why there are large spikes at throttle tip-in. However, the trends in toque are very similar between the chassis dynamometer and the engine dynamometer. The trends in engine speed for the engine dynamometer and chassis dynamometer also are in good agreement. The slight differences in toque and engine speed between the engine dynamometer test and the chassis dynamometer test can be attributed to differences in shift matrices. The shift matrix for the engine dynamometer tended to hold gears longer than the chassis dyno, resulting in slightly higher engine speed and lower brake toque for some portions of the cycle to attain the same acceleration.

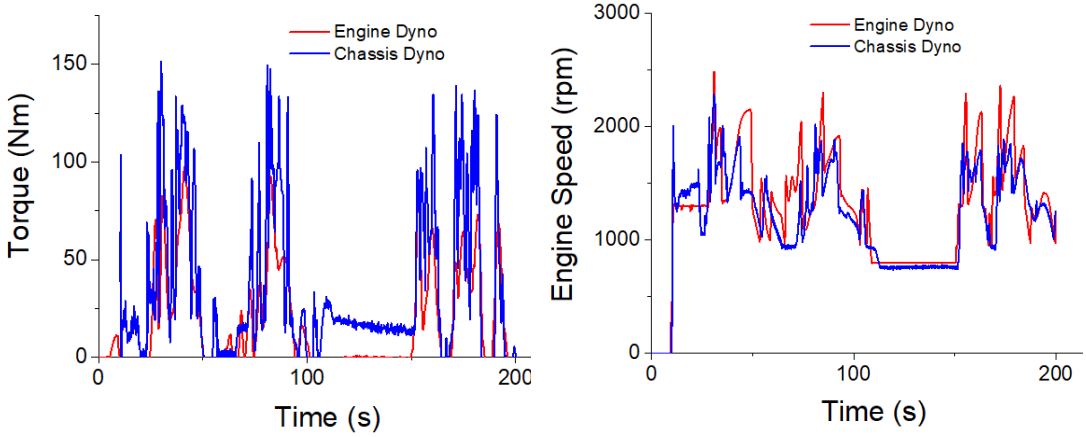

Figure 31: Engine torque (left) and engine speed (right) versus time over the first 200 seconds of the WLTP cycle compared to the manufacturer-provided engine data

Average particle size distributions (PSDs) are shown for the pre-GPF and post-GPF sampling location in Figure 32. These are average size distributions emitted for each fuel over three runs of the first 200 seconds of the WLTP. The standard deviation for each curve is approximately one order of magnitude due to spikes and dips in concertation due to fuel tip-in and fuel cut and is not shown so the individual curves can be clearly seen. The E50 fuel produced the lowest average particle concentrations of any fuel throughout the size

range. Under these conditions, the dilution of aromatics was dominant, outweighing the effect of delayed fuel evaporation caused by the high HoV of the ethanol. The high aromatic compound-containing fuel produced the highest average particle concentrations of any fuel throughout the entire size range. It appears under these conditions the pathway from aromatics to soot precures is dominant in producing compared to the volatility effect, because the low volatility fuel has the highest PM Index but produced few particles on average.

All fuels produced large 10 nm ash modes thought to originate from lubrication oil additives. This is consistent with the observed high oil consumption of the engine. The peaks of the ash mode generally followed the trend of the ~80 nm accumulation (soot) mode. If the accumulation and ash mode formation mechanisms were independent from one another, it would be expected that the ash mode would decrease as the accumulation mode increased due to the large soot particles scavenging the small ash particles. However, because this is not the case, it appears that the ash and soot mode are linked. As discussed in previous work, there may be fuel impingement on the cylinder walls which partially washes away the oil film and allows it to detach, atomize, and eventually be burned, leaving behind only the noncombustible ash particles [113].

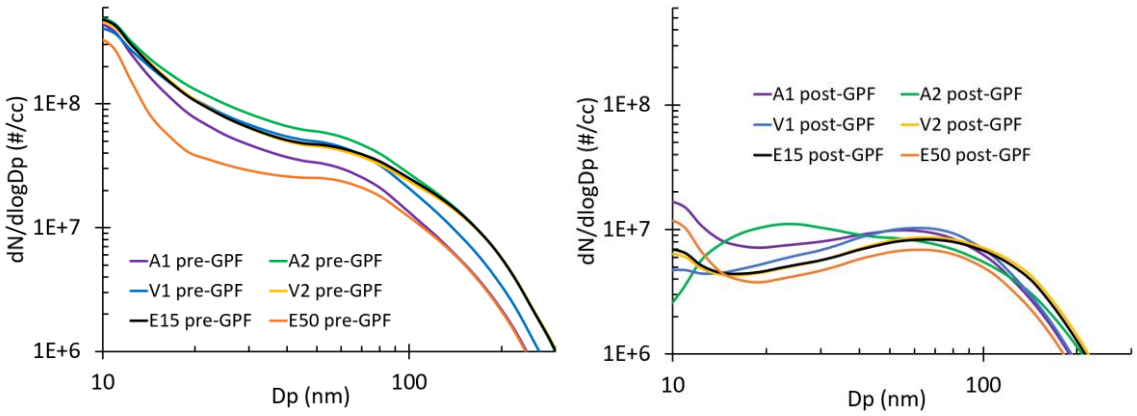

Figure 32: Average pre- and post-GPF PSDs over the first 200 seconds of the WLTP

The post-GPF size distributions show the GPF was very effective at removing the 10 nm ash mode. The concentration of 10 nm ash particles was reduced by two orders of magnitude for most fuels, corresponding to a filtration efficiency of 99% at this size. However, because such a large ash mode was emitted from the engine-out location, a significant amount of 10 nm ash particles slipped through the GPF. Current PN emission limits are for particles greater than 23 nm under the European Particle Measurement Programme (PMP) [126]. Due to the high toxicity of very small particles, it is possible that the PN regulatory limits will be reduced to include 10 nm particles in the future. Because many GPFs can capture more than 99% of 10 nm particles, they may not be thought to a concern with GPF implementation. However, with a clean GPF and high oil consumption, these results show that there can be considerable 10 nm particle penetration. This could be addressed by optimizing filter pore size for > 99% filtration efficiency with a clean filter. On the other hand, an engine with very high ash emissions will eventually load the filter with ash and increase the filtration efficiency, mitigating the ash slip problem.

Figure 33 shows the pre- and post-GPF solid PN > 23 nm and PM emissions for three fuels over three runs with error bars representing one standard deviation. The fuels

highlighted here are the highest emitter (the high aromatics fuel A-2), the lowest emitter (E50), and one in between the two (the low volatility fuel V-1). The pre-GPF emissions were very repeatable with each fuel showing distinct traces. For the first 200 seconds of the WLTP cycle, the high aromatics fuel produced the highest cumulative pre-GPF emissions and the high ethanol fuel producing the lowest cumulative pre-GPF emissions. However, there was high run-to-run variability in the post-GPF emissions. The highest variability was seen for the A-2 fuel. The A-2 fuel had the highest post-GPF emissions of the three fuels on the first run with a clean GPF, however, the A-2 fuel had the lowest post-GPF PM emissions of any fuel on the third run. The high engine-out PM emissions from the A-2 fuel loaded the GPF over the first two runs and increased its filtration efficiency to a high level. Even though the engine-out emissions stayed high during the third run, because the GPF filtration efficiency was sufficiently high, the post-GPF emissions were lower than any fuel. This shows the significance of the state of loading of the GPF. The E50 fuel produced the lowest average cumulative post-GPF PM emissions. However, the A-2 fuel produced the second lowest average cumulative post-GPF PM emissions, even though the average pre-GPF emissions were much high than the V-1 fuel.

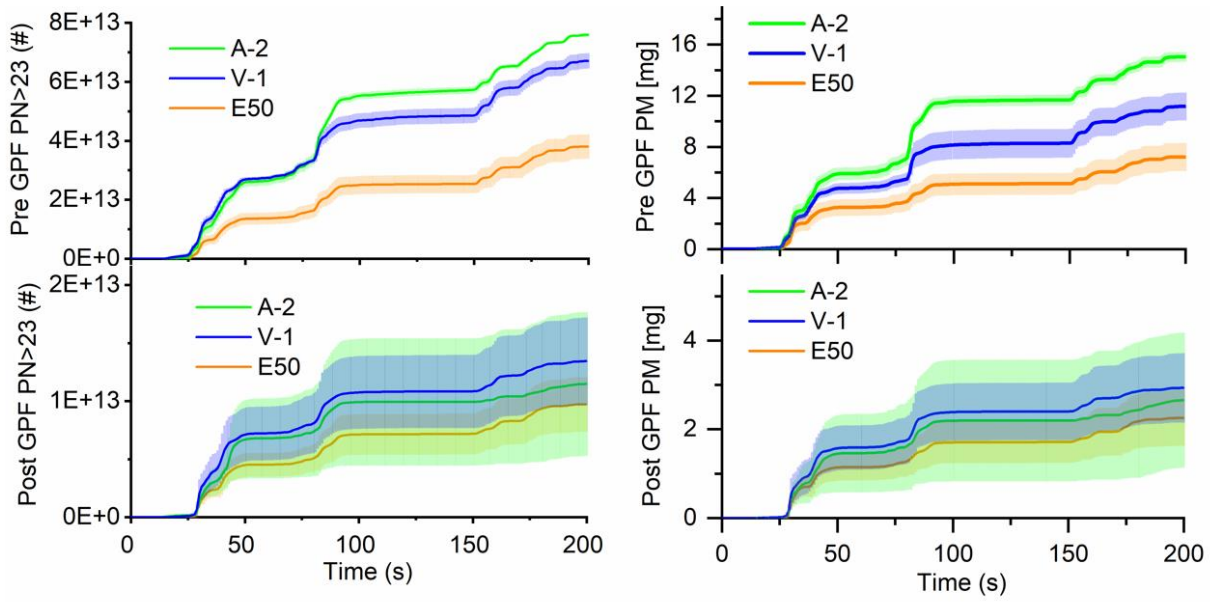

Figure 33: Cumulative solid PN > 23 nm pre- and post-GPF (left) and cumulative PM pre- and post-GPF (right) over the first 200 seconds of the WLTP

The effect of the soot loading on GPF filtration efficiency over the three runs are shown in Figure 34. Again, fuels A-2, V-1, and E50 are highlighted to show the trends with a high, mid, and low emitting fuel, respectively. For each fuel, the filtration efficiency curve increased for each subsequent run as soot was loaded over the three runs. For each fuel, the most penetrating particle size (MPPS) was near 70 nm and for each run (ignoring downward slopes around 500 nm for now), and for each fuel, the filtration efficiency at MPPS on the first run was just under 60%. This shows each round of fuel testing started with a clean filter. For the A-2 fuel, the filtration efficiency reached exceeded 90% at 70nm on the third run, whereas the A-2 fuel and E50 fuel only reached 82% and 73% respectively at 70 nm on their third runs. This illustrates how the highest engine-out emitting fuel, A-2, produced low GPF-out emissions than the lowest engine-out emitting fuel, E50.

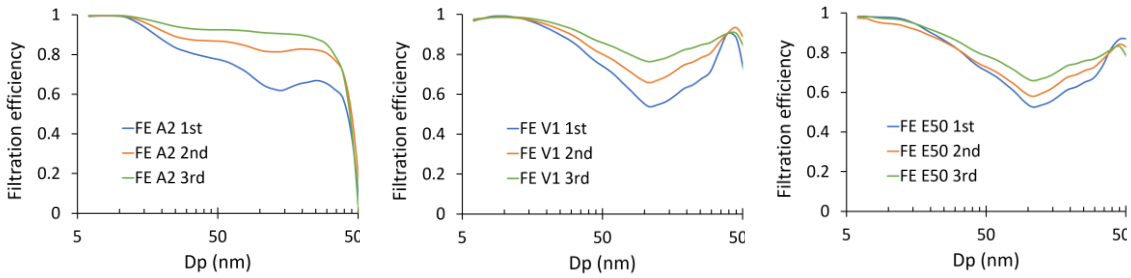

Figure 34: Average size resolved filtration efficiency over each 200 second run of the WLTP for fuels A-2, V-1, and E50

The filtration efficiency curves all showed an unusual drop in filtration efficiency near 500 nm. This is unusual because for most filter media the MPPS is near 100-200 nm. Particles smaller than the MPPS are effectively trapped by diffusion, and particles larger than that are effectively trapped by impaction and interception [127]. From examining the time resolved PSD data for each run, there are very few ~500 nm particles emitted from the engine out location. However, at around 180 seconds elapsed time into the cycle, there was a large spike in ~500 nm particles from the post-GPF location for all fuels, with no emission of particles of this size at the pre-GPF location. During this period, the engine goes from high load to a fuel-cut condition. Initially, the post-GPF spike in PM was thought be due to a partial regeneration. However, the GPF temperature reached approximately 150 °C, a temperature too low for regeneration. It is currently unclear what caused this throughout the experiments. Particles of this size could be catalyst material from the GPF releasing during a sudden change in filter flowrate; suspended soot particles of this size are very rare. Another explanation could be the release of coagulated soot particles at the back of the filter. This would be an interesting area to explore in future work, but because the relative concentration of the ~500 nm particles is order of magnitudes less than particles in

the 10 -100 nm size range, the tail in the filtration efficiency curve does not significantly affect the total filtration efficiency.

Comparisons between cumulative soot mass emitted and cumulative PN > 23 nm emitted over the first 200 seconds of the WLTP cycle with the PM Index and fuel aromatics concentration at the engine-out location are shown in Figure 35. The soot concentration measured by the MSS correlated about equally well with the aromatics concentration as it did with the PM Index, with an r-squared value of ~0.5. The engine out PN > 23 correlated fairly well with the aromatic concentration of the fuel, but poorly with the PM Index. This may be explained by looking at the soot and PN > 23 nm concentrations. There should be a strong linear correlation between soot mass and PN > 23 nm if particle density and the particle size distribution remain constant.

A discrepancy can be seen between the PN > 23 and soot concentration in the order of the relative magnitudes for each fuel. The low volatility fuel, V-2, produced the highest soot concentrations but the high aromatics fuel, A-2, produced the highest PN > 23 nm concentrations. From examining the particle size distributions in Figure 32, the A-2 fuel emitted a higher fraction of particles between 23 nm and 100 nm than the V-2 fuel. Above 100 nm, the PSDs from the two fuels converge. If the soot mass emitted was equal for the A-2 and V-2 fuels, it could be explained that most of the particle mass is in the distribution above 100 nm. However, because the V-2 has higher soot mass than V-2, it would seem to indicate that it also has higher soot density.

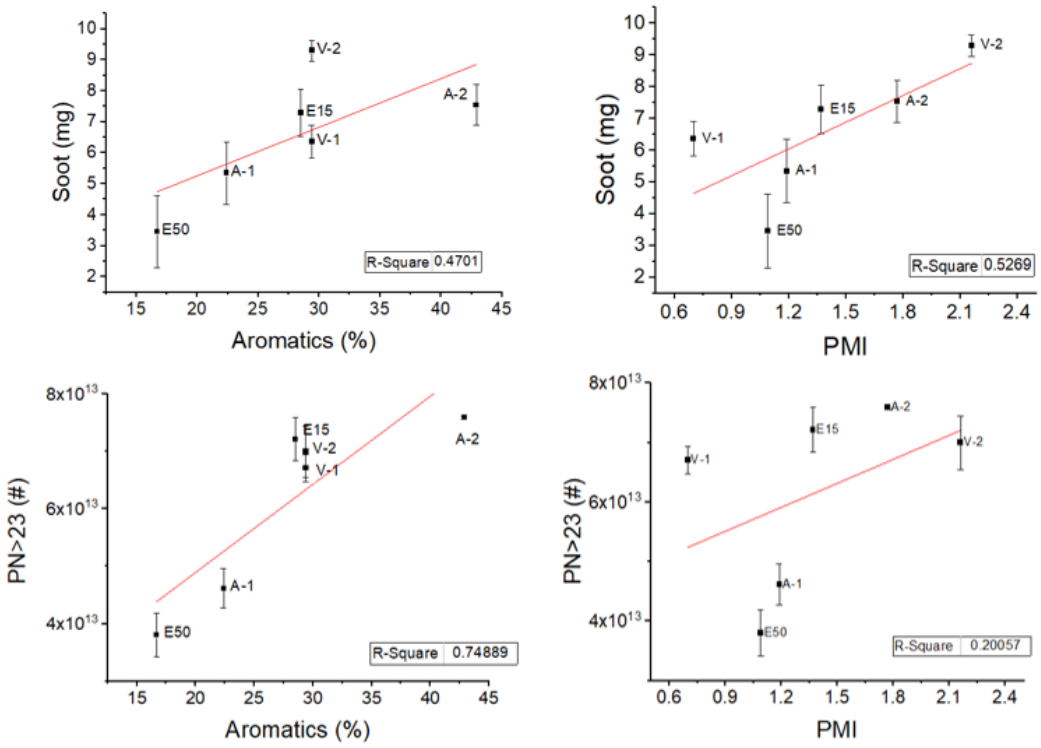

Figure 35: Correlation between cumulative soot mass and fuel aromatics concentration (top left), cumulative soot mass and PMI (top right), cummulative solid PN > 23 nm and fuel aromatics concentration (bottom left), and cummulative solid PN > 23 nm and PM Index (bottom right) over the first 200 seconds of the WLTP. All emissions are pre-GPF.

4.3 Effects of ethanol concentration and combustion strategy on the effective density of GDI PM

As discussed in Chapter 2, particle effective density can provide information on particle morphology as well as enable real-time mass emission measurements. In this section, the effects of fuel properties and combustion mode on GDI PM emissions are further explored with effective density measurements. Specifically, the interesting trend discussed in section 4.1 that highly oxygenated fuels having opposing effects on PM emissions from the lean stratified and lean homogeneous conditions is explored. Effective density was measured for these conditions to understand the underlying mechanisms.

4.3.1 Experimental

The engine used in this study was the same as discussed in previous chapters. The exhaust sampling system was also essentially the same as discussed previously, except for the addition of a centrifugal particle mass analyzer (CPMA) and a scanning mobility particle sizer (SMPS). Figure 36 shows a schematic of sampling system used for this experimental study.

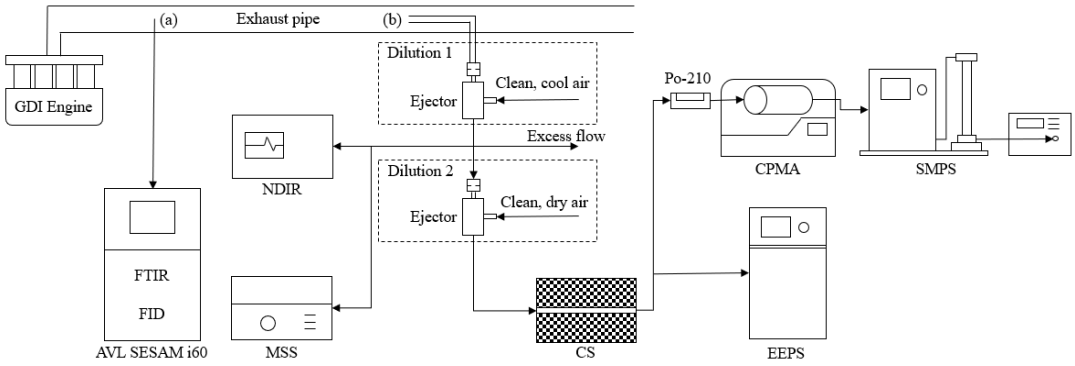

Figure 36: Sampling system schematic for density measurements

The CPMA is an instrument that classifies particles by their charge-to-mass ratio. Particles that enter the CPMA flow through the annulus of two rotating cylinders charged with a variable electrical potential. The particles experience both an electrostatic and centrifugal force. Particles of only a specific charge-to-mass ratio exit the CPMA. A charge neutralizer was placed upstream of the CPMA to impart a known charge distribution on the aerosol. The SMPS measured the PSD of the aerosol exiting the CPMA, which consisted of only particles of a selected mass. From this, the mean mobility diameter for a given particle mass was determined.

Three steady state engine conditions tested in this study and are detailed in Table 4. They were all run at 2000 rpm and included the three GDI combustion modes previously

discussed operated at 7 bar BMEP for the stoichiometric and lean homogeneous conditions, and 4 bar BMEP for the lean stratified condition. Three fuels of varying ethanol concentration were tested with each engine condition. The fuels tested were the E10 certification fuel (referred to as the baseline fuel in previous sections) and E30 and E50 fuels that were splash blended using ethanol and the E10 baseline fuel. Each fuel and engine condition combination were run three times on separate days. The stoichiometric condition was not tested with the E50 fuel because the particle concentrations were too low to measure. The CPMA-SMPS system was calibrated using polystyrene latex (PSL) particles of diameters 100, 125, 152 and 203 nm.

Table 4: Engine conditions tested. S=stoichiometric, LH=Lean homogenous, LS=lean stratified

Mode	Speed [RPM]	BMEP [bar]	φ
S	2000	7	1
LH	2000	7	0.69
LS	2000	4	0.65

4.3.2 Results and discussion

Particle size distributions are shown for each of the engine conditions and fuels in Figure 37. The same trend appeared as was discussed in section 4.1: as the ethanol concentration increased, the accumulation mode greatly decreased for the lean stratified condition and greatly increased for the lean homogeneous condition. In this experiment, the addition of the E30 fuel further confirmed this trend. Both PSDs for the LH and LS conditions with the E30 fuel showed concentrations in between those of the E10 and E50 fuels for the respective conditions. Additionally, because these fuels were splash blended, it confirms that this is an effect of the ethanol, and not high-end hydrocarbons added to the match blended E50 fuel used in the experiment of section 4.1.

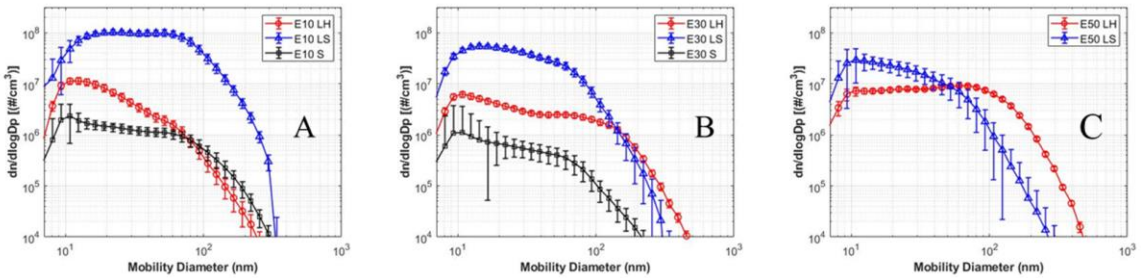

Figure 37: Particle size distributions for each engine condition and fuel

The density functions for each engine condition and fuel are shown in Figure 38. For all cases, the effective density decreases with particle size, which is consistent with the fractal structure of soot agglomerates. For the lean stratified condition, the effective density moderately decreased with increasing ethanol concentrations. This can be explained by the relative concentrations of ash and soot. It can be seen in Figure 37 that the accumulation mode for the lean stratified condition decreases faster than the ash mode with increasing ethanol. This would result in a greater amount of ash embedded in the soot agglomerates, and higher densities.

The effect of ethanol concentration on the density of soot from the lean homogeneous condition was strong and differed from that of the lean stratified condition. The E30 and E50 fuels produced soot with similar densities that were significantly higher than the soot density produced by the E10 fuel. This may be a result of a change in soot formation mechanisms involved with a late injection delivering a fuel with a high heat of vaporization at high load (i.e. high quantity of fuel). As discussed in section 4.1, for the lean stratified condition, the dominant effect of increased ethanol was the dilution of aromatics, leading to lower soot, but the soot formation mechanism is assumed to be the same for E10-E50. However, for the lean homogeneous condition, the soot formation mechanism changes with an increase in ethanol. The dominant effect of ethanol for the lean homogeneous condition

was inhibiting the evaporation of fuel. The large quantity of high HoV fuel injected late in the combustion cycle may lead to liquid fuel droplets suspended in the combustion chamber at the start of combustion. This could lead to greater fuel pyrolysis, more tightly bound primary particles, with higher densities and sphericity.

The stoichiometric engine condition produced the highest density soot particles and exhibited a moderate decrease in density when the fuel ethanol concentration increased. The possible cause for this will be discussed later in this section.

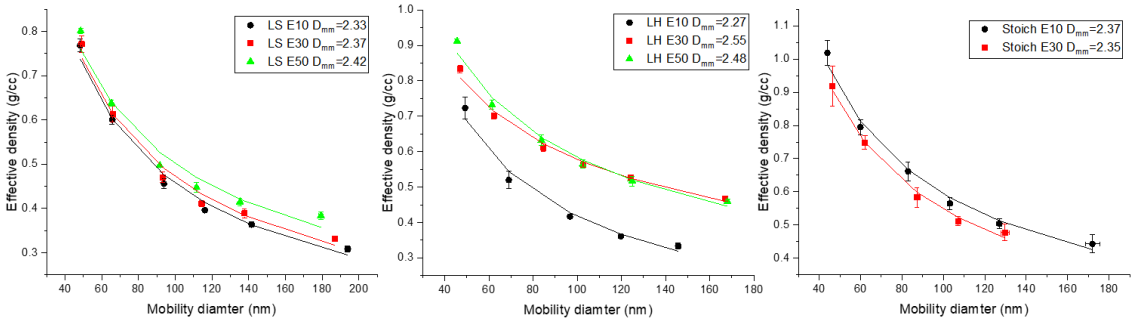

Figure 38: Measured effective density functions for each engine condition and fuel

Particle mass concentrations were calculated using the effective density functions and integrated particle size distributions (IPSD). Figure 39 shows the comparison between the IPSD method and the soot concentration measured by the MSS for each engine condition and fuel. The first notable observation is that the addition of ethanol decreased the soot mass concentration by an order of magnitude for the lean stratified condition and increased it by an order of magnitude for the lean homogeneous condition. This, as previously discussed, underscores how influential fuel formulation is and how its effect is not always the same across engine conditions.

The IPSD method indicates PM mass concentrations 50-100% higher than what was reported by the MSS for the lean stratified condition. However, for the other conditions,

there is good agreement between the IPSD and MSS. Work is currently underway to determine the cause of the disagreement between the IPSD and MSS for the lean stratified condition. One theory is that the lean stratified condition produces soot with tightly bound heavy hydrocarbons that are not removed by the catalytic stripper. An experiment for future work is to evaluate this by sampling PM onto a filter and performing and elemental carbon (EC)/organic carbon (OC) balance. If a substantial amount of OC is present after the CS, it is likely the source of the disagreement between IPSD and MSS.

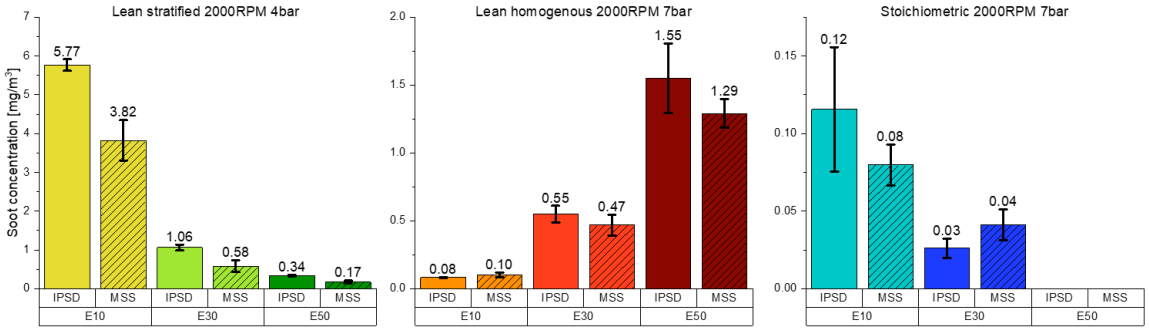

Figure 39: Comparison of total soot concentration measured by MSS and those calculated from ISPD methods using the corresponding measured effective density functions

Chapter 5 A Novel, In Situ Soot Oxidative Reactivity Measurement Method: The Effects of Lube Oil Ash on GDI Soot Oxidative Reactivity in a Catalytic GPF

As discussed in Chapter 2, characterizing soot oxidation kinetics is crucial to understanding how GPFs perform in terms of filtration efficiency and pressure drop. The filtration efficiency and pressure drop across a GPF are dependent on the level of soot loading on the filter. The most common method for measuring soot oxidative reactivity is TGA. Because TGA is an offline method, it may not be the most accurate in predicting how soot is oxidized on a GPF, especially when using a catalytic GPF. The catalytic washcoating of a GPF may enhance oxidation rates through surface interactions as the soot loads on the filter. In this work, a novel in-situ soot oxidative reactivity measurement was developed. The method involved loading a catalytic GPF under high temperature conditions conducive to soot oxidation and measuring the filtration efficiency of 100 nm particles. A correlation was made between filtration efficiency and loaded soot mass on the filter in order to allow calculation of the soot oxidation rate.

5.1 Operating Conditions and Setup

The engine used in this experiment was the same as was used in Chapter 3 and Chapter 4. The exhaust sampling system and engine setup for the oxidation experiments were nearly identical as in the fuel properties experiments described in Chapter 4.1. The sampling system schematic is shown again in Figure 40. The dilution ratios for the pre-GPF and post-GPF particle sampling were approximately 100:1 and 10:1, respectively. The tandem EEPS upstream and downstream of the catalytic GPF measured particle size distributions at a rate

of 1 Hz to enable calculation of size resolved GPF filtration efficiency as the GPF was loaded with soot.

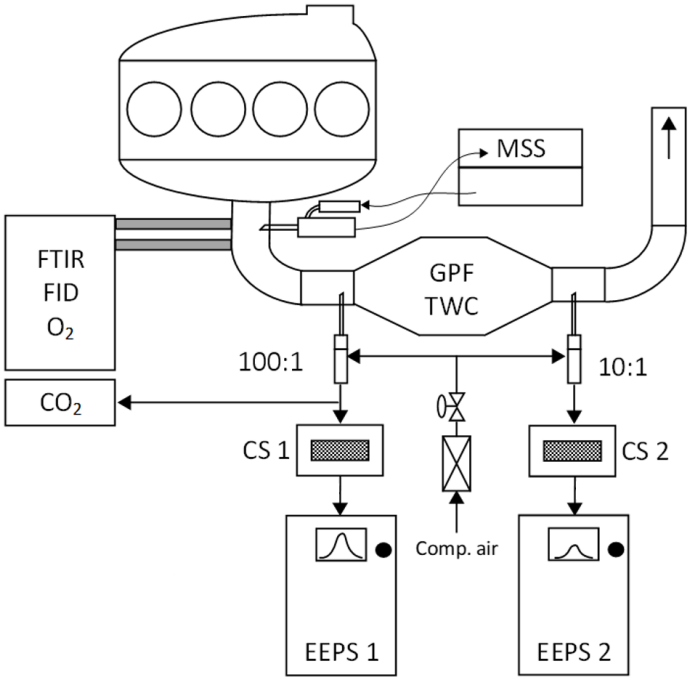

Figure 40: Engine setup and sampling schematic for GPF loading oxidation experiments

Three oil formulations, shown in Table 5, were tested over four GPF loading engine conditions. The three oil formulations were blended from 100% polyalphaolefin (PAO) base stock and varied only in the additives that were blended into the oil. The first oil contained 10,000 ppm of zinc dialkyldithiophosphate (ZDDP), which is an anti-wear additive that is known to inhibit oxidation. The second oil contained no additives and is referred to as the non-detergent or Non Det oil. The third oil contained 5,000 ppm of calcium sulfonate, which is an oil additive that is known to promote oxidation. The oil additive formulations were selected to such that one oil would inhibit soot oxidation, one oil would have no effect on soot oxidation, and one oil would enhance soot oxidation. The oils were tested in the order that they appear in the table.

Table 5: Oil formulations used for the

Oil	Additives (Concentration)
ZDDP	ZDDP (10,000 ppm)
Non Det	None
Ca	Calcium (5,000 ppm)

The four GPF loading engine conditions are detailed in Table 6. The first condition, Non-Ox Ref, was a low temperature condition that was used as a reference condition in which no soot oxidation would occur on the GPF. The remaining three engine conditions were oxidizing conditions in which soot oxidation occurred on the GPF due to high exhaust temperatures and excess oxygen. The oxidizing conditions included a mid-temperature condition with moderate soot, a high temperature condition with lower soot, and a high temperature condition with higher soot. All conditions have relatively high soot concentrations compared to baseline conditions from previous sections for the purpose of loading the GPF with soot more quickly (1-2 hours per run). All conditions were run with lean equivalence ratios. The oxidizing engine conditions equivalence ratios were of 0.79-0.80 which corresponds to an engine-out oxygen concentration of ~3.8%. Soot has been shown to undergo oxidation on catalytic GPFs at temperatures as low as 500 °C [59].

Table 6: Engine conditions for GPF loading oxidation experiments

Condition [-]	Eng. Speed [rev./min]	BMEP [bar]	φ [-]	T GPF [° C]	Soot [mg/m^3]
Non-Ox Ref	2000 ± 0	4.00 ± 0.08	0.70 ± 0.01	414 ± 4	1.78 ± 0.25
Mid Temp	2000 ± 0	6.34 ± 0.05	0.80 ± 0.00	524 ± 4	2.46 ± 0.44
High Temp	2000 ± 0	7.79 ± 0.05	0.79 ± 0.00	563 ± 4	1.93 ± 0.16
High Temp/Soot	2000 ± 0	7.75 ± 0.05	0.79 ± 0.00	566 ± 4	2.98 ± 0.24

The non-oxidizing reference condition was the LS2 condition discussed in Chapter 3 and Chapter 4. The oxidizing engine conditions were calibrated by combining the injection

strategies of the lean homogeneous and lean stratified combustion modes. A primary injection during the intake stroke delivered most of the fuel and a very late secondary injection near the spark event delivered the remaining fuel. This enabled operation at higher loads to create high exhaust temperatures conducive for soot oxidation and the high soot concentrations required to load the GPF. The injection strategy and equivalence ratio were adjusted to reach the desired soot concentration. The load and spark timing were adjusted to reach the desired exhaust temperature. Table 7 details the injection and spark timings for the oxidizing conditions.

Table 7: Injection strategy and spark timing for the oxidizing GPF loading conditions

Condition [-]	SOI 1 [°bTDC]	SOI 2 [°bTDC]	Split 1 [-]	Split 2 [-]	Spark [°bTDC]
Mid Temp	350	28	0.80	0.20	18
High Temp	270	15	0.93	0.07	18
High Temp/Soot	270	15	0.90	0.10	18

Each engine condition was run three times for each of the oil formulations. The duration of each GPF loading run was between 45 and 90 minutes in order to challenge the GPF with 100 to 200 mg of soot. The GPF was regenerated between each engine condition using the method described in Chapter 4. One set of engine conditions was run per day. When switching oil formulations, the engine was "rinsed" with the next oil to remove residual oil of the previous test. To do this, the old engine oil was drained, the engine was filled with the next test oil, run up to operating temperature, then drained again, and finally, a new oil filter was installed and the engine was filled with the fresh test oil. The fuel used was one batch of commercially available summer blend 91 AKI E10 gasoline.

5.2 Experimental Methods: Oxidation Rate Calculation

To determine the soot oxidation rate for each condition, first, a soot mass balance was defined with the GPF as the control volume:

$$\dot{m}_{ox} = \dot{m}_{in} - \dot{m}_{out} - \dot{m}_{filter} \quad \text{Eq. 5.1}$$

where $\dot{m}_{ox}$ is the soot oxidation rate on the filter, $\dot{m}_{in}$ is the rate of soot mass that is incoming to the filter, $\dot{m}_{out}$ is the rate of soot mass that penetrates and exits the filter, and $\dot{m}_{filter}$ is rate of soot mass that loads on the filter. The soot mass rate into the filter is calculated from:

$$\dot{m}_{in} = C_{in}\dot{V} \quad \text{Eq. 5.2}$$

where C_{in} is the soot mass concentration at the inlet of the filter and $\dot{V}$ is the exhaust volumetric flowrate. The rate of soot mass out of the filter is the product of $\dot{m}_{in}$ and the particle mass penetration, P_m:

$$\dot{m}_{out} = \dot{m}_{in}P_m = C_{in}\dot{V}P_m \quad \text{Eq. 5.3}$$

$$P_m = \frac{C_{out}}{C_{in}} = 1 - E \quad \text{Eq. 5.4}$$

where C_{out} is the mass concentration at the outlet of the filter, and E is the filtration efficiency. The rate of soot loading on the filter is

$$\dot{m}_{filter} = \frac{d}{dt}m_{filter}(t) \quad \text{Eq. 5.5}$$

where m_{filter} is the cumulative soot mass loaded on the filter.

With the available information, i.e. the difference between incoming and outgoing soot, the soot trapped on the filter cannot be distinguished from the soot that is lost due to oxidation. However, because filtration efficiency depends on soot loading, a correlation was able to be developed to determine soot mass on the filter using the filtration efficiency

over the GPF loading period. To do this, the GPF was first loaded using a non-oxidizing, reference condition while measuring real time filtration efficiency. With no oxidation occurring on the filter, the soot mass on filter can be calculated at any time in the loading period as the difference of cumulative soot mass in to and out of the filter. Combining Eq. 5.1 through Eq. 5.4:

$$m_{filter,non-ox}(t) = \int_0^t C(t)\dot{V}(t)dt - \int_0^t C(t)\dot{V}(t)P(t)dt \qquad \text{Eq. 5.6}$$

Using Eq. 5.6 and the measured filtration efficiency as the GPF loaded over the non-oxidizing reference condition, a curve of filtration efficiency versus filter soot loading was obtained. However, because filtration mechanisms depend on several factors such as particle diameter, filter porosity, filter fiber diameter, face velocity, and gas properties, this curve could not be used to directly determine soot loading from the filtration efficiency curves of the oxidizing conditions. Instead, the filtration efficiency curves of oxidizing conditions were corrected to values that represented what the filtration efficiency would be if the filter was under the same conditions as the non-oxidizing reference condition.

Relations between filtration efficiency and parameters that differed between the reference condition and the oxidizing conditions, such as temperature and face velocity, were required to correct for these effects. From Hinds [127], the minimum single fiber filtration efficiency, $\hat{E}_\Sigma$, of a filter can be calculated by

$$\hat{E}_\Sigma = 1.44\left[\left(\frac{1-\alpha}{Ku}\right)^5\left(\frac{\sqrt{\lambda}kT}{\eta}\right)^4\left(\frac{1}{U_o^4 d_f^{10}}\right)\right]^{1/9} \qquad \text{Eq. 5.7}$$

where α is filter solidity or packing density, Ku is the Kuwabara hydrodynamic factor which is a function of only α, λ is the mean free path, k is the Boltzmann constant, T is gas

temperature, η is the dynamic viscosity, U_0 is the face velocity, and d_f is the filter fiber diameter. This assumes that the only important filtration mechanisms at this particle size, near the MPPS, are interception and diffusion. Using filter properties and the single fiber filtration efficiency, the filter penetration for a given particle size can be calculated using [127]:

$$\hat{P} = \exp\left(\frac{-4\alpha\hat{E}_{\Sigma}t}{\pi d_f}\right) \quad \text{Eq. 5.8}$$

By assuming filter solidity, thickness, and fiber diameter are constant for a given level of soot loading, the ratio of $\hat{P}$ at the reference condition and $\hat{P}$ at the oxidizing condition gives:

$$\frac{\ln(P_{cor})}{\ln(P)} = \frac{\hat{E}_{\Sigma,\mathrm{ref}}}{\hat{E}_{\Sigma}} \quad \text{Eq. 5.9}$$

where P_{cor} is the penetration corrected to the non-oxidizing reference condition. Simplifying:

$$P_{cor} = P^{\frac{\hat{E}_{\Sigma,\mathrm{ref}}}{\hat{E}_{\Sigma}}} \quad \text{Eq. 5.10}$$

Combining Eq. 5.4 and Eq. 5.10 gives the filtration efficiency corrected to the non-oxidizing reference condition:

$$E_{cor} = 1 - (1-E)^{\wedge}\left(\frac{\left[\left(\frac{\sqrt{\lambda}kT}{\eta}\right)^4\left(\frac{1}{U_0^4}\right)\right]^{1/9}}{\left[\left(\frac{\sqrt{\lambda_{ref}}kT_{ref}}{\eta_{ref}}\right)^4\left(\frac{1}{U_{o,ref}^4}\right)\right]^{1/9}}\right) \quad \text{Eq. 5.11}$$

It should be noted that only the filtration efficiency of 100 nm particles was used for these calculations. This is important because total number filtration efficiency and total

mass filtration efficiency depend on the particle size distributions, so differences in PSDs between the reference condition and the oxidizing conditions would create an invalid comparison. Additionally, Eq. 5.7 was derived assuming the only important filtration mechanisms are diffusion and interception, due to the minimum single fiber filtration efficiency being at the MPPS. As previously reported, 100 nm is very close to the MPPS of this filter, thus the assumptions are considered valid.

The mass of soot on filter can be determined using the corrected filtration efficiency and the reference filtration efficiency versus soot mass on filter curve. The mass of soot on filter at all points during the loading period for the oxidizing condition were determined by using the reference condition as a look-up table. In other words, the values of the corrected filtration efficiency were found on the loading curve of the reference condition, then, the points in the oxidizing loading period were assigned the corresponding values for soot mass on filter. With soot mass on filter known, the soot oxidation rate with units of mg/min, can be calculated using:

$$\dot{m}_{ox} = C_{in}\dot{V} - C_{in}\dot{V}P_m - \frac{d}{dt}m_{filter} \qquad \text{Eq. 5.12}$$

Finally, the specific soot oxidation rate, $\hat{r}_{ox}$, with units of (mg/mg)/min or min^{-1}, can be calculated using:

$$\hat{r}_{ox} = \frac{\dot{m}_{ox}}{m_{soot,filter}} \qquad \text{Eq. 5.13}$$

5.3 Results and Discussion

The non-oxidizing reference condition produced a very repeatable filtration efficiency loading curve, shown in Figure 41. The curve represents the average of nine loading runs (three runs for each of three oils) with error bars showing one standard deviation. The non-

oxidizing condition starts with a clean filter filtration efficiency at 100 nm of ~67% and reaches over 99% with just 60 mg of soot on the filter.

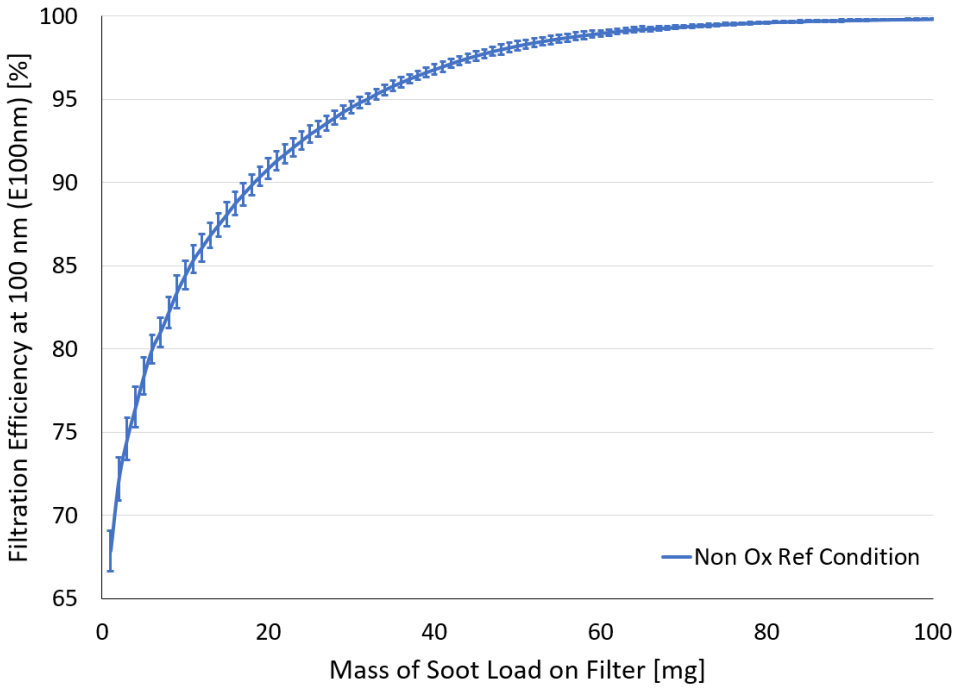

Figure 41: Reference non-oxidizing loading condition: average filtration efficiency at 100 nm as a function mass of soot on filter for three oil formulations tested and a non-oxidizing loading condition

Pre-GPF particle size distributions emitted from the oxidizing GPF loading engine conditions for each of the oils are shown in Figure 42. These conditions produced the similar broad distributions of the lean stratified conditions described in Chapter 3 and Chapter 4. As previously discussed, the broad distributions are hypothesized to form from the wide range of local, in-cylinder equivalence ratios caused by multiple stratified injections. These zones result in a gradient of soot formation zones that produce soot particles of a broad size range. The Mid Temp condition produced a larger fraction of particles near the 20 nm mode compared to the High Temp conditions which produced flatter distributions between 20 nm and 70 nm. This is likely due to the different injection

strategy used by the Mid Temp condition compared to the High Temp conditions. Because the calculations used to for determining soot oxidation in this experiment were based on the filtration efficiency at 100 nm, the slight differences in PSDs did not affect the results.

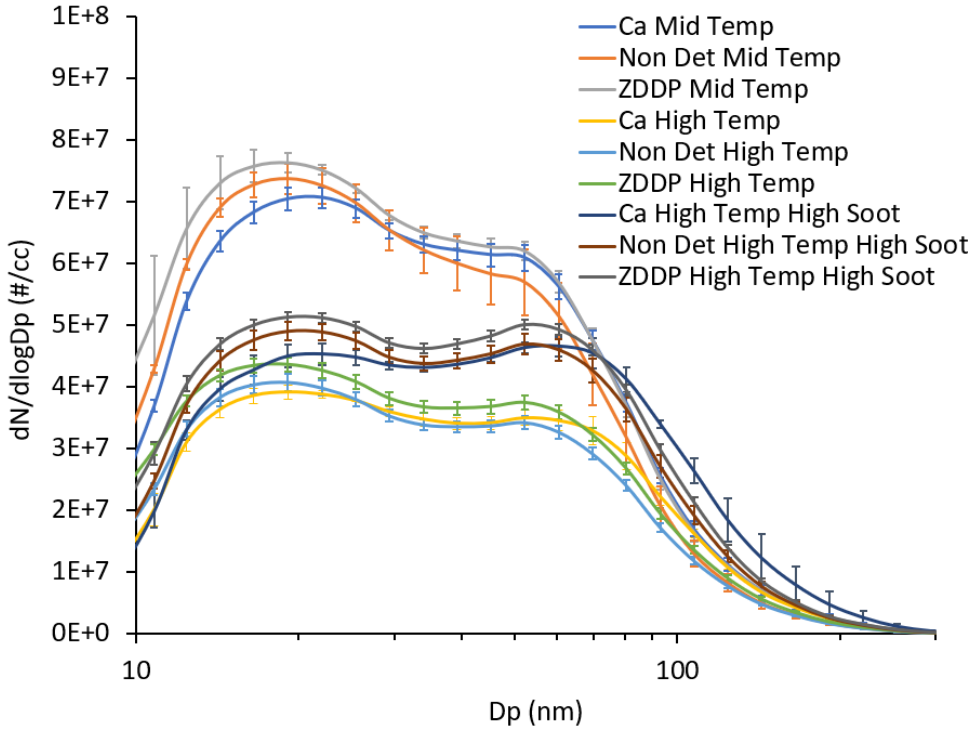

Figure 42: Pre-GPF particle size distributions for each of the oxidizing GPF loading engine conditions and each of the oils

Calculated soot oxidation rates over the GPF loading period are shown for the Mid Temp, High Temp, and High Temp High Soot conditions in Figure 43, Figure 44, and Figure 45, respectively. These plots also include the E100nm curves for the respective conditions. The E100nm curves are the average of three runs for a given oil with error bars representing one standard deviation from the mean. The oxidation rates are calculated from the mean E100nm of the three runs and are plotted as a moving average over 10 mg of cumulative soot load into the filter (not to be confused with soot on the filter).

For each condition, the Ca oil caused the GPF to load at a much slower rate than the Non Det oil, indicated by a lower and shallower E100nm curve (fast/slow loading rate is inferred by the change in filtration efficiency relative to the amount of soot challenged). Conversely, the ZDDP oil generally caused the GPF to load at a faster rate than the Non Det oil. These trends are explained by the soot oxidation rates. The difference in filtration efficiency curves between oil formulations was caused by a difference in soot mass on the filter. Because the clean filter efficiencies were approximately the same for each oil but the E100nm curves diverged as the filter was challenged with soot, it indicates that, for certain oils more than other, more soot was oxidized, and not trapped, on the filter. This is confirmed by the oxidation rate curves. The oxidation rate curves appear as inverted E100nm curves. The calcium oil caused the slowest loading rates because it caused the highest soot oxidation rates, and the ZDDP oil had the fastest loading rates because it caused the slowest soot oxidation rates.

For the Mid Temp condition, shown in Figure 43, all the oxidation curves decrease from their initial values to an asymptote. This suggests that the catalyst washcoating on the GPF is playing a role in soot oxidation. At the beginning of the loading period, as soot starts to load on the filter, free soot particles that impact the catalyst washcoating oxidize faster than soot particles that impact the layer of soot that builds up on the filter as it loads. The observed soot oxidation rate decreases until the surface to volume ratio becomes sufficiently small that the observe oxidation rate is equal to the intrinsic oxidation rate of the soot cake, or the soot cake stops forming and the soot loading and oxidation reach equilibrium.

At the Mid Temp condition, the equilibrium Ca soot oxidation rate is almost three times higher than that from the ZDDP or Non Det oils. The oxidation behavior of the ZDDP oil varied from the other two oils. It was initially higher than the Non Det oil, slowed to less than the Non Det oil, and then eventually equaled the rate produced by the Non Det oil.

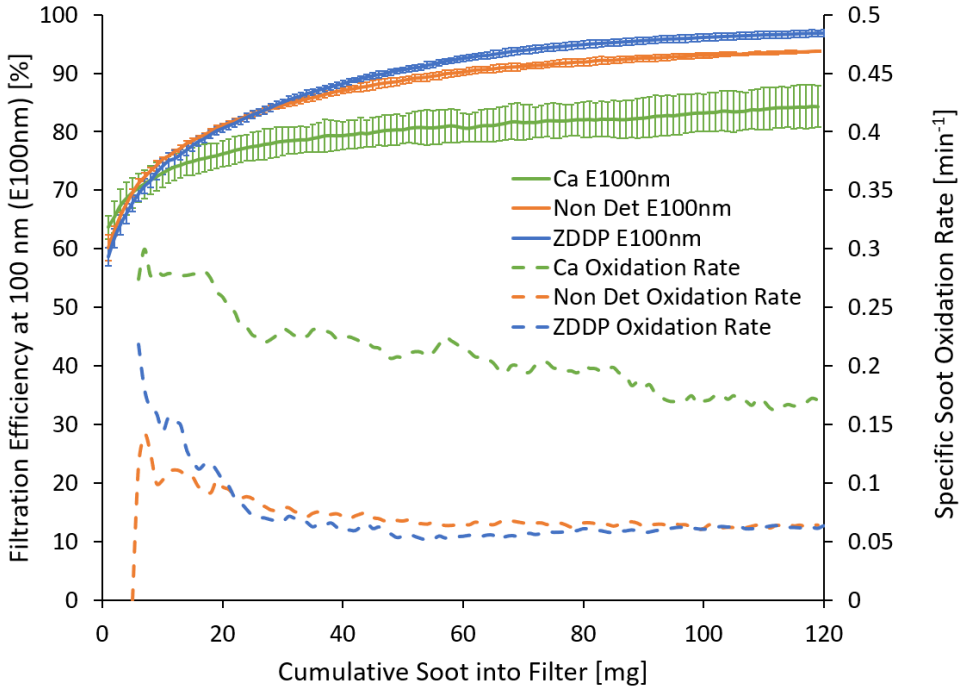

Figure 43: Filtration efficiency at 100 nm and specific soot oxidation rates for each oil at the Mid Temp condition

The ZDDP and Non Det oil produced very repeatable E100nm curves, but the Ca had significantly higher variation. It was determined that this was caused by ash loading on the GPF because the initial clean filter E100nm monotonically increased for each run. The concentration of Ca used in this study is higher than would be used in a commercial oil, which resulted in accelerated ash loading. Because the Ca was the last oil tested, the ash loading did not affect results from the Non Det or ZDDP tests. The ZDDP likely did not cause ash loading because of its relatively low melting point of 420 °C.

As expected, the High Temp condition, shown in Figure 44, resulted in higher soot oxidation rates than the Mid Temp Condition for all oils. The Ca soot oxidation rates were much higher than the other two oils. For this condition a soot cake never formed when using the Ca oil. This resulted from the flat E100nm curve. The soot mass on filter only reached ~ 2 mg. Consequently, the Ca soot oxidation at this condition represents mostly free particle oxidation on the catalyst surface. The ZDDP soot oxidation rate was a slightly less than half that of the Non Det oil. This would indicate that the ZDDP soot oxidation inhibitor mechanism favors high temperature, because the ZDDP and Non Det rates were very similar for the Mid Temp condition.

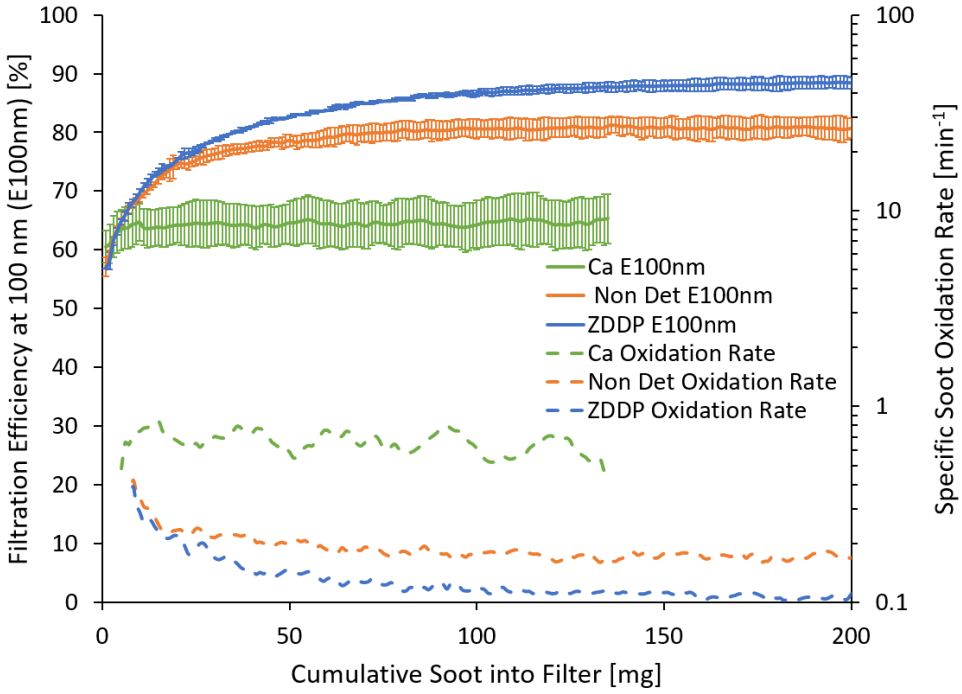

Figure 44: Filtration efficiency at 100 nm and specific soot oxidation rates for each oil at the High Temp condition

The results of the High Temp High Soot condition, shown in Figure 45, were very similar to the High Temp condition. Differing from the High Temp condition, the Ca oil at

this condition resulted in modest filter loading, as opposed to almost none. The filter loaded with ~8 mg of soot for the Ca condition. For the Ca and Non Det oils, the E100nm curves reached higher values and the oxidation rates were lower. This is a result of the ~50% higher engine-out soot concentration.

Higher soot concentrations lead to more soot loading on the filter and a lower surface to volume ratio causing a larger fraction of soot to be in contact with the oxidation promoting catalyst surface of the GPF. Additionally, for the Ca oil, the higher soot concentration lead to a lower ash fraction in the soot, diminishing the influence of the catalytic effect of the Ca. Soot from the ZDDP oil at the High Temp High Soot condition exhibited approximately the same oxidation rate as the High Temp condition. This was a result of the effects of lower ZDDP ash fraction and the higher soot surface to volume opposing each other. The lower ZDDP ash fraction diminished the influence of the ZDDP-inhibiting soot oxidation, while lower surface to volume ratio of the soot diminished the influence of the GPF catalyst promoting oxidization.

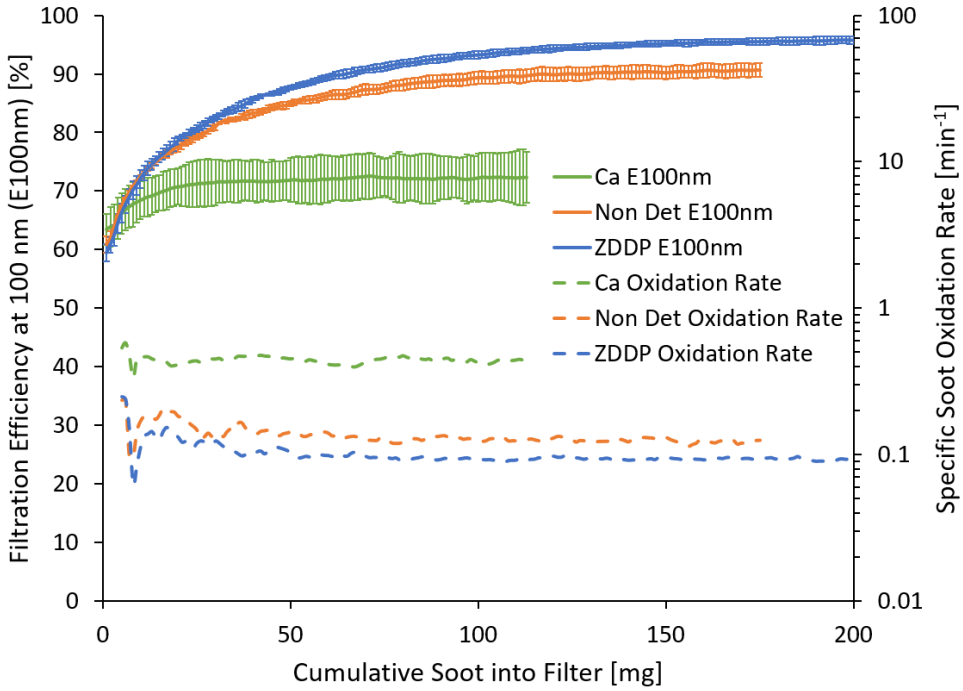

Figure 45: Filtration efficiency at 100 nm and specific soot oxidation rates for each oil at the High Temp High Soot condition

Figure 46 shows a comparison of the equilibrium soot oxidation rates for each oil at each condition. Because oxidation rates for all oils tested appear to near an asymptote by the end of the loading period, the equilibrium rate was calculated as the average specific soot oxidation rate over the last 20 mg of cumulative soot into the filer. The catalytic effect of the Ca oil was clearly demonstrated by oxidation rates ~2.5-3.5 times higher than the Non Det oil. Mostly free particle soot oxidation resulted in a 41% higher soot oxidation rate for the Ca oil at the High Temp condition compared to the High Temp High Soot condition. The oxidation inhibiting effect of the ZZDP oil was shown for the High Temp conditions but did not appear to have a definitive effect at the Mid Temp condition. The effect of the catalyst surface was shown by the Non Det oil for the High temp conditions. If there was no effect from the catalyst on the GPF, the specific soot oxidation rate would be constant for a non-detergent oil with no ash influence. However, because the soot

oxidation rate has and inverse relationship with the engine-out soot concentration, it suggests the catalyst increases soot oxidation rate through surface interaction.

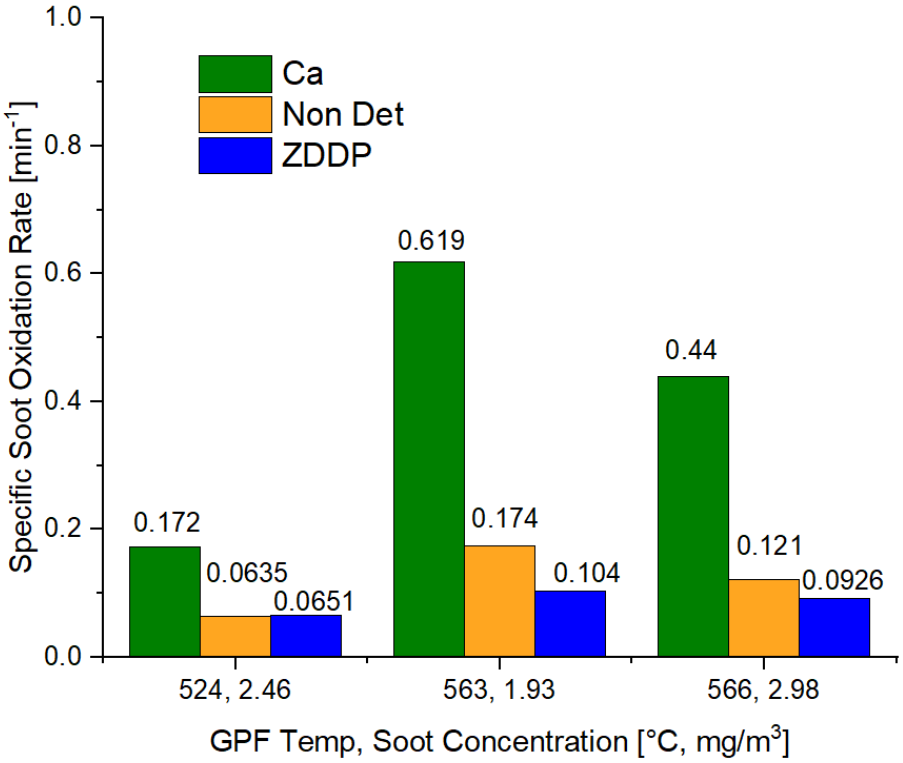

Figure 46: Equilibrium specific soot oxidation rates for each engine condition and oil

Choi and Seong measured GDI soot oxidation rates using isothermal TGA at 600 °C of soot from a GDI engine running with fuels doped with calcium sulfonate, non-detergent oil, and ZDDP [23]. They reported specific soot oxidation rates of 0.1 to 0.5 min^{-1} for the soot from the Ca doped fuel, ~0.03 min^{-1} for the soot from the non-detergent oil doped fuel, and 0.01 to 0.02 for soot from the ZDDP doped fuel. The results from the current study using a novel oxidative reactivity method showed similar trends and rates on the same orders of magnitude as the TGA study. However, soot oxidation in the current work occurred at much lower temperatures than the 600 °C used in the TGA study. For the non-detergent oil, oxidation rates in the current study are ~2 to 6 times greater than what is

reported for soot at 600 °C in a TGA, for the Mid Temp and High Temp conditions respectively. The Ca soot in the current study exhibited oxidation rates in the same range as reported for 600 °C TGA oxidation, but at the temperature range of 524-566 °C. The ZDDP soot oxidation rates in the current study were ~3 to 10 times higher than what is reported for TGA at higher temperature. These findings further indicate that the catalytic surface of the GPF plays an important role in soot oxidation.

The novel soot oxidative reactivity measurement method reported in this section offers a clear advantage over TGA for understanding practical oxidation rates in GPFs because it can demonstrate the influence of a catalytic GPF. Additionally, because it is an in-situ method, it does not require soot samples removed from the environment in which the oxidation rates interest. However, there are some difficulties inherent to the current method. The developed approach is an indirect measurement method, and significant post-processing is required for calculating filtration efficiencies, converting to soot mass on filter, and finally oxidation rate. TGA benefits in this regard as being a direct measurement of mass, of which oxidation rate is simply the time derivative. A reference condition must be established for this method, which creates an additional experimental step. Additionally, ash loading causes the clean filter efficiency to drift. This could cause error over long periods of testing. Correction for ash loading would need to be performed, either by periodically establishing a new reference curves or by starting with a new GPF for each run.

Chapter 6 Dicarboxylic Acid Emissions from Aftertreatment Equipped Diesel and Catalyzed GPF Equipped GDI Engines

The work detailed in previous chapters focused on the emission of solid particulate matter regulated under PN limits. However, this chapter focuses on currently unregulated emissions that are influential to the formation atmospheric aerosols. The limited existing research on IC engines as a primary source of dicarboxylic acids does not address whether modern engines equipped with exhaust aftertreatment systems are also a primary source. This question is answered in the current experimental study by evaluating various engine conditions and fuel formulations to determine their potential influence on secondary atmospheric aerosols. To make this investigation more complete, a diesel engine was also tested in addition to the GDI test engine previously described. The contents of this section were previously published in peer-reviewed journals [128,129].

6.1 Dicarboxylic Acid Emissions from Aftertreatment Equipped Diesel Engines

This section presents the quantification of monocarboxylic and dicarboxylic acids in both the gas and particle phase in diesel engine exhaust sampled from before and after an ATS consisting of an oxidation catalyst and diesel particulate filter. The goal of the work was to definitively prove whether dicarboxylic acids are generated in diesel engine combustion and whether they can be eliminated using a modern ATS. Engine conditions with excessively high engine-out HC emissions were tested to determine the efficacy of ATS to eliminate dicarboxylic acids from the engine-out exhaust.

6.1.2 Experimental methods

Exhaust was sampled from an automotive 2.0 L common rail direct injection turbodiesel engine on an engine dynamometer. The engine was equipped with a factory exhaust ATS consisting of a diesel oxidation catalyst (DOC) and diesel particulate filter (DPF). Three diesel combustion modes were tested. They included an early low temperature combustion (ELTC) mode, a conventional diesel combustion (CDC) mode, and an active DPF regeneration (Regen) mode. Full control of all engine parameters was enabled by a National Instruments Powertrain Controls software that replaced the factory ECU. The software was developed with the factory ECU to closely match the factory calibration. The CDC mode employed two fuel injections, the ELTC mode employed a single early injection, and the regen mode employed a similar injection strategy to CDC with the addition of a post top dead center injection for catalyst heating. shows engine parameters for the three combustion modes. Nominal engine parameters for the three combustion modes tested are shown in Table 8. More complete details regarding the engine experimental setup and operating conditions are given in previous work [103].

One round of testing was conducted per day and included sampling all three engine modes at steady state conditions. Three rounds of testing were conducted in total. Prior to the start of data collection, the engine was started and run until the coolant reached a steady value. The engine was then operated at high speed and load (2500 rpm, 8 bar BMEP) for five minutes. This was done to produce high in-cylinder temperatures to oxidize injector fowling and deposits that contribute to soot formation. The DPF was then regenerated following the procedure described by Prinkhodko and Parks [60]. This set a baseline engine state from which filter sampling proceeded. The sequence of the combustion modes tested

was the same as that shown in Table 8. Stabilization periods were run prior to sampling from each combustion mode. Stabilization periods included 15 minutes of DPF regeneration prior to sampling the Regen mode, 30 minutes of CDC prior to sampling the CDC mode to allow a soot cake to form on the DPF, and 15 minutes of ELTC prior to sampling the ELTC mode to allow emissions to stabilize.

Table 8: Nominal engine parameters for the three combustion modes tested. BMEP = brake mean effective pressure in bar, ET = energizing time in ms, SOI = start of injection in degrees before top dead center (°bTDC), EGR = exhaust gas recirculation rate in %.

Mode		Regen	CDC	ELTC
Speed	[rpm]	1500	1500	1500
BMEP	[bar]	4	4	2
Torque	[Nm]	64	64	32
BSFC	[g/kWhr]	385	240	340
ET Pilot	[ms]	0.285	0.290	0
SOI Pilot	[°bTDC]	21.6	17.6	-
ET Main	[ms]	0.610	0.625	0.475
SOI Main	[°bTDC]	7.3	7.0	28
ET Post	[ms]	0.650	0	0
SOI Post	[DATDC]	80	-	-
Rail Press.	[bar]	600	675	1000
EGR	[%]	0	25	45

Gaseous emissions measurement instruments used in these experiments included an AVL (Graz, Austria) SESAM i60 FT multi-component exhaust measurement system composed of a Fourier Transform infrared spectrometer (FTIR), separate CO_2 non-dispersive infrared (NDIR) analyzer, and flame ionization detector (FID). The FTIR was used for gas phase emissions quantification and speciation prior to and after the ATS. The FID measured total hydrocarbon concentrations before and after the ATS, and the separate NDIR analyzer measured CO_2 concentration of the intake manifold to allow calculation of EGR fraction. Soot mass concentration was measured using an AVL (Graz, Austria)

Microsoot Sensor (MSS) analyzer. Size distributions of total particulate matter (PM), which includes both soot and semi-volatile materials, were measured using a scanning mobility particle sizer (SMPS) spectrometer (Model 3936, TSI Inc, Shoreview, MN). PM mass concentration was calculated from SMPS size distributions assuming particles of unit density.

Figure 47 shows a diagram of the exhaust dilution and filter loading system. Pre- and post-ATS exhaust gas was diluted and aged in 1.3 m long dilution tunnels at a dilution ratio of 10:1 with a residence time of approximately three seconds. All dilution was achieved with ejector pump (EP) dilutors with critical orifices upstream of the sample flow. The dilution tunnels featured a 15-degree conical entrance region to mitigate flow separation caused by an abrupt change in cross sectional area followed by two concentric hollow cylinders. Chilled, compressed air was sent through the outer cylinder to maintain a sample temperature of 20 °C. The dilution conditions were chosen to enhance semi-volatile particle growth as would occur in a primary exhaust plume. Specifically, the results of Abdul-Khalek et al.[35] were referenced to select a primary dilution ratio, dilution tunnel temperature, and residence time that would be conducive to nucleation mode growth. A three-way-valve at the tunnel inlet was used to take periodic particle size distribution and soot concentration measurements pre- and post-ATS. Secondary dilution of 100:1 was required to keep the particle concentration within the measurement range of the SMPS at the engine-out sampling location.

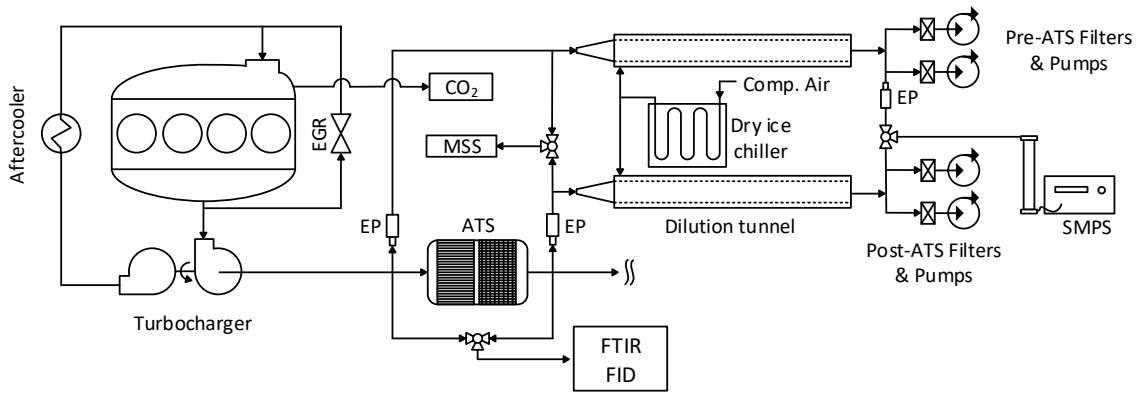

Figure 47: Diagram of the test setup used in the experiments including sampling train and instrumentation. MSS = Micro-soot sensor, EP = Ejector pump diluters, FTIR = Fourier Transform Infrared analyzer, FID = Flame ionization detector, SMPS = scanning mobility particle sizer.

Sample pumps (AirChek XR5000, SKC Inc., Eighty Four, PA) were used to flow dilute exhaust through quartz fiber filters (37 mm, cat. no. 225-1822, SKC, Inc.) at a rate of 3 L/min and a sample period of 60 minutes. A total of four filters were sampled at a time for each engine condition; two filters, KOH impregnated and plain, were positioned pre-ATS and post-ATS. Both KOH and plain filters captured particle phase emissions while the KOH impregnated filter also captured gas phase acid emissions.

The KOH-impregnated filters were prepared according to a modified version of the method used by Kawamura and Kaplan [130]. Quartz fiber filters were supported on Teflon rings and KOH solution (0.1 M, 1 mL) in high purity water (> 18 MΩ cm^{-1}) added to the surface. The filters were dried at 80°C in a convection oven for 1 h. The dry filters were loaded on polypropylene support pads (cat. no. 225-2902, SKC, Inc.), mounted in a SureSeal certified leak-free, clear plastic cassette (cat. no. 225-401, SKC, Inc.), and the seal was then secured with electrical tape to ensure cassettes only be opened by inlet caps, and not disassembled.

Non-impregnated filters were arranged directly atop polypropylene supports and sealed in sampling cassettes with no further handling. All manipulations involving filters, except for heat treatment, were performed in a designated laboratory space free of carboxylic acids and protected by particle-free, laminar air flow. Carboxylic acids were excluded from the laminar flow hood. Sealed filter assemblies were stored at -20°C. Four blank filters were analyzed. Two of which, one KOH and one plain, were installed in sampling cassettes and were handled and stored as previously described with all other filters. These are designated simply as "blank filters". The other two blanks, also one KOH and one plain, were exposed to the engine test cell environment with the cassette caps off for ~ 4 hours and were then handled and stored as previously described with all other filters. These are designated as "test cell blank filters". Additionally, samples of engine diesel fuel and lubricating oil were analyzed to determine fuel-borne dicarboxylic acid concentrations *via* direct derivatization of their organic extracts using the same derivatization and analytical methods detailed below.

Used filter assemblies were stored at -20°C prior to analysis. The quartz filters were removed from their cassettes with forceps and placed into 15 mL polypropylene centrifuge tubes containing high purity water (4 mL). The filters were allowed to swell and mix by vortex agitation for 30 s, followed by sonication for 5 min. The pH of the extracts from impregnated filters varied between 8.3 and 9.0. Extracts from non-impregnated filters were adjusted to the 8.5-9.0 pH range with 10 N NaOH solution. Aliquots of the filter extracts (1 mL) were transferred to 1.5 mL microfuge tubes and concentrated to ca. 10 μL volumes in a SpeedVac system (SVC-100H, Savant Instruments, Inc., Farmingdale, NY) without heating. *O*-terphenyl in *n*-hexane (2 mg mL^{-1}, 5 μL) was added to the dried residue,

followed by 10% w/w BF_3 in *n*-butanol (75 µL). The solutions were mixed by vortex agitation for 15 s and then heated in a water bath at 80°C for 45 min.

Derivatized samples were cooled to room temperature, quenched with 2% w/v sodium bicarbonate solution (500 µL) and extracted with 1:1 v/v diethyl ether:*n*-hexane (400 µL). An aliquot of the organic phase (300 µL) was transferred into a new microfuge tube, the extraction of the aqueous phase repeated two more times, and the combined extracts (900 µL) dried over sodium sulfate. An aliquot (300 µL) of the dried organic extracts was transferred to an HPLC vial directly followed by automated injection onto the GC column.

Samples were analyzed by gas chromatography-mass spectrometry (GC-MS) using a 7890A gas chromatograph with 5975C Inert XL EI/CI mass selective detector (Agilent Technologies) operating in EI mode under the following conditions: column, DB-5ms (Agilent); column dimensions, L, 30 m, ID, 0.25 mm, DF, 0.5 µm; injection volume, 1 µL; injector temperature, 225°C; injection mode, split (5:1); temperature profile, 35°C for 5 min, 20°C min^{-1} to 300°C, maintained at 300°C for 4 min, for a total run time of 22.23 min; MSD source temperature, 230°C; MSD quadrupole temperature, 150°C; carrier gas, helium; carrier gas flow rate, 1.0 mL min^{-1}. The instrument was operated in synchronous SIM and Scan mode.

Peak areas were normalized using *o*-terphenyl the internal standard. Quantitation was performed using calibration curves of *n*-butyl ester derivatives of each acid of interest prepared in tandem with samples. The calibration curves consisted of at least six standards per analyte, typically spanning the 0-100 µg mL^{-1} range. The lower limit of detection (LOD) of the method, defined as three times the noise level, varied as a function of the acid is given in Table 9.

Table 9: Lower limit of detection (LOD) for all acids measured in the experimental study including emissions index (mg/kg-fuel) for each engine mode.

Mode/ Acid	(μg/ml)	(ng/inj.)	ELTC (mg/kg-fuel)	Regen (mg/kg-fuel)	CDC (mg/kg-fuel)
Formic	0.224	0.224	0.314	0.247	0.355
Acetic	0.189	0.189	0.265	0.208	0.300
Propionic	0.180	0.180	0.252	0.198	0.285
Butyric	0.159	0.158	0.222	0.175	0.251
Oxalic	0.240	0.240	0.336	0.265	0.380
Malonic	0.109	0.108	0.152	0.120	0.172
Maleic*	0.151	0.151	0.211	0.166	0.239
Succinic	0.185	0.185	0.259	0.204	0.293
Fumaric**	0.207	0.207	0.289	0.228	0.327
Glutaric	0.093	0.09328	0.130	0.103	0.147
Adipic	0.0916	0.09155	0.128	0.101	0.145

* *Z*-butenedioic acid; ***E*-butenedioic acid

6.1.3 Results and Discussion

Exhaust emissions of gas-phase species, total PM mass and soot mass concentration varied widely between the three combustion modes and the two sampling locations as shown in Table 10. The table provides the average emissions measured for each combustion mode in fuel based emission factors (EF) as mass of component emitted per mass fuel consumed [131]. Error is represented by one standard deviation of collected data. The EF of a component *i* is given by:

$$EF_i = \frac{[i]}{\left(\frac{[CO]}{MW_{CO}} + \frac{[CO_2]}{MW_{CO2}} + 3\frac{[C_3H_{3y}]}{MW_{C_3H_{3y}}}\right) MW_C} C_F \qquad \text{Eq. 6.1}$$

where [i], [CO], [CO_2], and [C_3H_{3y}] are mass concentrations of the component of interest, CO, CO_2, and THC respectively, MW represents the molecular weight of each component, y is the H/C ratio of the fuel, and C_F is the carbon mass fraction of the fuel.

Due to the post top dead center fuel injection used in the Regen mode, total hydrocarbon (THC) emissions from the engine-out sample location over-ranged the FTIR, thus gas phase emissions data could not be collected for this mode and sample location. During testing, the FID reported THC concentrations above 6500 ppm (232 g/kg), but extended sampling of such high concentrations was undesirable.

The ATS was effective in oxidizing THC for the Regen and CDC combustion modes due to sufficiently high catalyst inlet temperatures (260 °C and 266 °C, respectively). Table 10 shows THC concentrations for the Regen DPF Out and CDC DPF below detectable limits of the FID analyzer. However, the ELTC mode shows poor THC conversion and had a catalyst inlet temperature of approximately 184 °C.

Soot emissions were highest for the CDC mode at the engine out sample location, with an emission factor of 331 mg/kg fuel. Soot emissions at the DPF out sample location were below the detection limit of the MSS, indicating high filtration efficiency from an adequate soot cake built up on the DPF. The soot emissions from Regen DPFO out show that most of the soot was either oxidized or collected on the DPF, but because the soot cake on the DPF had been oxidized, the filtration efficiency dropped to 91.8%. The advantage of the ELTC mode is realized from the near-zero engine-out soot emissions and very low NO_x at the cost of high unburned THC emissions. The ELTC combustion mode is described further in other work [103].

Total PM emissions were highest for engine-out Regen, which were largely eliminated through the ATS indicating that the PM consisted of unburned organic species. Total PM and total soot loaded on the filters was calculated from the exhaust concentrations combined with the filter flowrate.

Table 10: Average gas phase and particulate phase emissions factors for the three engine modes and two sampling locations, engine out (EO) and DPF out (DPFO) including one standard deviation from the mean as uncertainty estimate. Soot and PM loaded on filters calculated using filter gas flowrate. ND = not detected and NM = not measured.

Mode		Regen	CDC	ELTC
THC EO	[g/kg]	>232	4.92 ± 1.22	23.6 ± 1.68
THC DPFO	[g/kg]	ND	ND	19.4 ± 2.29
NO_x EO	[g/kg]	NM	10.5 ± 0.329	1.06 ± 0.0365
NO_x DPFO	[g/kg]	15.6 ± 0.662	10.8 ± 0.368	1.42 ± 0.0361
Soot EO	[mg/kg]	87.0 ± 8.51	331 ± 74.1	ND
Soot DPFO	[mg/kg]	7.06 ± 0.614	ND	ND
PM EO	[mg/kg]	5046 ± 747	523 ± 133	485.4 ± 75.1
PM DPFO	[mg/kg]	9.90 ± 0.683	0.0958 ± 0.0163	7.45 ± 8.00
Soot Load EO	[µg]	791 ± 77.3	2090	ND
Soot Load DPFO	[µg]	64 ± 5.6	ND	ND
PM Load EO	[µg]	$4.59x10^4$±$6.79x10^3$	$3.31x10^3$±841	$3.47x10^3$±537
PM Load DPFO	[µg]	90.0 ± 6.21	0.606 ± 0.10	53.3 ± 5.73
ATS In Temp.	[°C]	260 ± 3.0	266 ± 3.0	184 ± 2.1
ATS Out Temp.	[°C]	622 ± 10.0	251 ± 2.4	176 ± 4.1

Figure 48 shows engine-out particle size distributions for the three tested engine conditions. The concentrations shown represent the number of particles formed in the dilution tunnel per unit of exhaust gas volume which is determined by multiplying the dilution tunnel particle concentration by the total dilution ratio. Most the particles that make up the curve for ELTC consist of semi-volatile species created through gas to particle conversion in the dilution tunnel as described in our previous work [132]. This is confirmed by noting that ELTC mode had very high particle number concentrations, but the lowest soot emissions. The CDC mode had a distribution that more closely resembled the typical bi-modal distributions for mainly solid particles in diesel exhaust [19]. The Regen mode also had a large soot mode that includes a large fraction of semi-volatile species condensed onto the solid particles. The DPF largely eliminated semi-volatile particles, thus distributions from these modes are not shown.

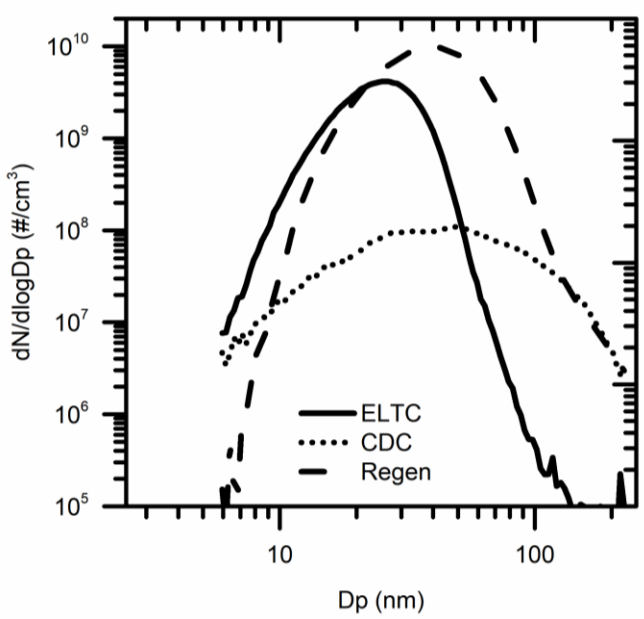

Figure 48. Engine-out particle size distributions for each engine condition tested in the experiments.

Figure 49A shows the average emission factors of monocarboxylic (formic – butanoic) and dicarboxylic (oxalic – fumaric) acids calculated from the KOH impregnated filters and Figure 49B shows the average emission factors calculated from un-impregnated (plain) filters. The difference in detected mass between the two filter types indicate the quantity of collected acids in the gas phase. The results clearly show that KOH filters had significantly more collected material than the plain filters. Therefore, we can conclude that dicarboxylic acids emitted from the engine remained in the gas phase after primary dilution. Interestingly, the concentrations for malonic acid were approximately equal for both the KOH and plain filters for the Regen engine out condition. Furthermore, malonic acid was the only dicarboxylic acid detected on the plain filter. These results indicate that either engine out malonic acid was in the particle phase, or that it adsorbed on to the quartz filter media.

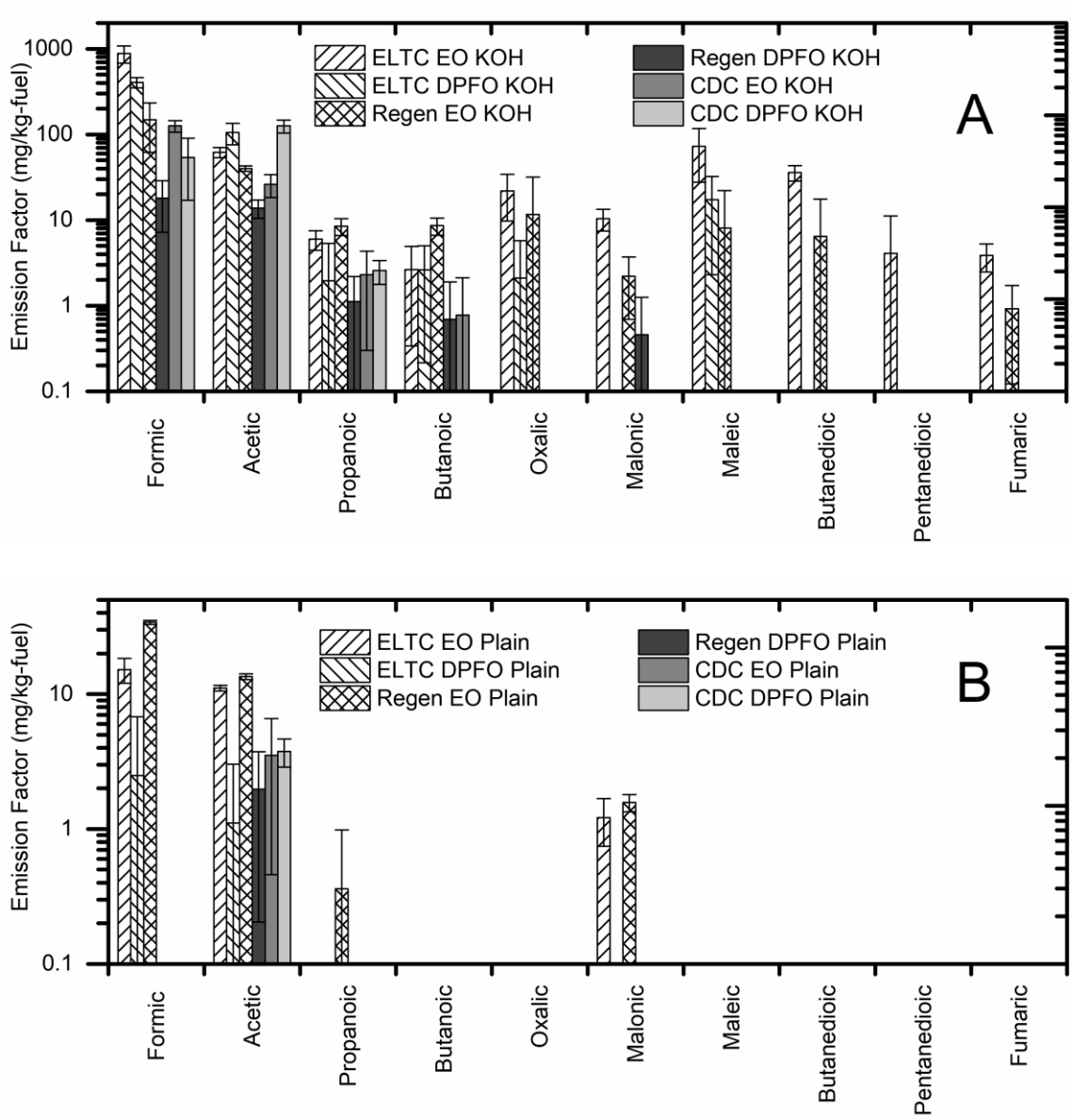

Figure 49: Gas phase and particle phase organic acid emission factors for the three engine conditions and two sampling locations for; A) KOH impregnated filters, and B) un-impregnated (plain) filters. Adipic acid was not measured for any condition and is omitted from the figure.

Monocarboxylic acids were detected in all CDC samples with no dicarboxylic acids measured. However, the other two modes had significant dicarboxylic concentrations, especially in the engine-out sample position. Given the high unburned hydrocarbon emissions and semi-volatile particle fraction for the ELTC condition, it was expected that

dicarboxylic acids would be present in relatively higher concentrations than the other two modes; this trend is confirmed in Figure 49. Six dicarboxylic acids were detected from the ELTC condition and were quantified from the KOH impregnated filters. Maleic acid was the most abundant dicarboxylic acid with an emission factor of 72.6 mg/kg fuel. Of the seven organic acids measured, six were present in the ELTC engine out condition and five were present in the regen engine out condition. No oxalic acid was collected on the plain filter indicating that the newly formed dicarboxylic acid was neither in the particle phase nor was it prone to adsorption on the filter. This is further evidence that Huang et al.[97] would not have detected oxalic acid via their collection method even if it were present since they only sought acids in the >56 nm particle phase using un-impregnated filters.

The dicarboxylic acid concentrations measured in this study are at most between 14 times (fumaric) and 57 times (malonic) greater than the concentrations measured Kawamura and Kaplan [30]. Additionally, malonic acid was the only acid collected on the plain filter in this study, while 35% of the oxalic acid was collected on the plain filter in the Kawamura and Kaplan study. Wentzel et al.[99] reported an emission factor of 1 mg lactic/oxalic acid per kg-fuel from a LDD equipped with a DOC. This is compared to a range of 2.11 to 21.9 mg oxalic acid per kg fuel measured in this study. Additionally, Wentzel el al.[99] reported a range of 3 - 60 mg propanoic acid per kg fuel, Friedman et al.[133] reported 0.3 – 0.76 mg propanoic acid per kg fuel from a non-ATS-equipped diesel heavy duty diesel, and this study measured 1.12 – 5.99 mg propanoic acid per kg fuel. Both Wentzel et al. and Freidman et al. used chemical ionization mass spectrometry (CIMS) for acid quantification. At this time, the cause of the wide variance of acid emission factors

from various engines and collection methods cannot be explained other than to say acid emissions are highly dependent on engine operating condition.

Compared to emission factors of polycyclic aromatic hydrocarbons (PAH), which are typically on the order of 10 to 100 µg/kg fuel[134–136], the acid emissions reported in this study are orders of magnitude higher. The sum of all acid collected from the KOH filters was 1100, 536 ,235, 34.1, 155, and 182 mg acid per kg fuel for ELTC EO, ELTC DPFO, Regen EO, Regen DPFO, CDC EO, and CDC DPFO respectively. The total acids collected on the KOH filter from the ELTC EO and Regen EO conditions represent 4.67% and 0.10% of the THC emissions respectively.

The ATS reduced or did not significantly change the gas phase acid concentration for all acids and conditions except for acetic acid. Interestingly, the DPF out acetic acid emission factor was higher than the engine out sample location for both ELTC and CDC. The average removal efficiencies for formic acid was 88%, 57%, and 54% for Regen, CDC, and ELTC modes respectively. The only condition that allowed a significant quantity of dicarboxylic acids to survive the ATS was the ELTC mode where catalyst light-off had not occurred. Overall, the ATS largely eliminated gas phase dicarboxylic acids when above the light-off temperature (≈ 250 °C).

No dicarboxylic acids were detected on the either the plain blank filter or plain test cell blank filters. Acids were also not detected on the KOH impregnated blank or test cell blank filters; however, propanoic acid was detected on the KOH blank filter in an amount that would equate to 2.09 mg/kg fuel. Formic and acetic acid were detected on the KOH test cell blank in amounts that would equate to 14.2 and 28.42 mg/kg fuel respectively (1.61% and 3.23% of max measured). Neither the fuel nor the lubricating oil contained detectable

dicarboxylic acids, showing that exhaust concentrations did not originate from unburned fuel and oil present escaping the engine combustion chamber.

Our results definitively illustrate the formation of dicarboxylic acids in diesel engine combustion, especially when engines are operated in low temperature combustion modes where gas phase hydrocarbon emissions are high. Current combustion kinetic mechanisms used in modeling do not incorporate dicarboxylic acids, though monocarboxylic acids are essential to combustion chemistry. The presence of additional oxygenated species like dicarboxylic acids could have implications for research in combustion chemistry. For example, synthesized oxygenated organic species have been hypothesized as possible soot particle inception precursors in combustion [137].

6.2 Dicarboxylic Acid Emissions from a GDI Engine Equipped with a Catalytic Gasoline Particulate Filter

With dicarboxylic acid emission shown for both engine-out and ATS-out sampling locations from a diesel engine, the current study sought to answer the question of whether dicarboxylic acids were emitted at similar concentrations from modern a GDI engine and if a catalyzed GPF effectively would remove them from the exhaust. Both oxygenated and nonoxygenated gasoline blends were used in the study to determine if acid emissions were influenced by fuel oxygenates. Finally, the study sought to determine if fuel injection strategy and charge mixture preparation from nonconventional GDI strategies, like lean operation, would influence carboxylic acid emissions.

6.2.1 Experimental Methods

The same GDI engine and catalytic GPF discussed in previous chapters was used in this experimental study. Two engine conditions, two fuels, and two exhaust sampling locations were studied. The details of the engine conditions are listed in in Table 11. The experiments included a stoichiometric condition (Stoich.), featuring two fuel injections during the intake stroke, and a lean stratified condition (Strat.), featuring three fuel injections during the compression stroke. The two fuels tested were commercial, summer blend nonoxygenated (E0) pump gasoline with an anti-knock index (AKI) of 91 and 10% ethanol (E10) gasoline splash blended using anhydrous ethanol and the E0 pump gasoline. Two exhaust sampling locations were used in the work; pre-GPF and post-GPF.

A diagram of the emissions sampling and measurement equipment is shown in Figure 50. The sampling system was essentially the same as the setup used in section 4.1 with the addition of filter loading for acid quantification.

Table 11: Nominal engine parameters for the two engine conditions tested. Where values differ between the two fuels, E0 and E10 is denoted. BMEP = brake mean effective pressure, BSFC = brake specific fuel consumption, ET = injector energizing time, SOI = start of injection in degrees before top dead center (°bTDC), and φ = fuel/air equivalence ratio.

Mode		Stoich.	Strat.
Speed	[rpm]	2000	2000
BMEP	[bar]	4	4
Torque	[Nm]	64	64
BSFC	[g/kWhr]	272 (E0) 279 (E10)	249 (E0) 255 (E10)
ET 1	[ms]	0.49	0.36
SOI 1	[°bTDC]	318	39
ET 2	[ms]	0.30	0.30
SOI 2	[°bTDC]	223	29
ET 3	[ms]	-	0.11
SOI 3	[°bTDC]	-	20
φ	[-]	1	0.625
Spark	[°bTDC]	38	22
Rail Press.	[MPa]	15	15
Pre-GPF T	[°C]	418 (E0) 422 (E10)	379 (E0) 384 (E10)
Post-GPF T	[°C]	487 (E0) 497 (E10)	395 (E0) 401 (E10)

Since very few particle phase acids were found in the previous study with diesel exhaust, only KOH impregnated filters were used for the GDI study to capture both gas and particle phase species. Exhaust gas was pulled through a sample line heated to 60 °C and then through a KOH impregnated filter at both the pre- and post-GPF diluter locations. Flowrates of 6 SLPM were pulled through the KOH filters with mass flow controllers and a vacuum pump. Moderate dilution was achieved with injection of 3 SLPM of clean, dry air into the heated line prior the KOH filters using additional MFCs for a filter dilution ratio of ~2:1. Because only the sample lines, and not the filter housing, were actively temperature controlled, moderate dilution assured no condensation occurred on the KOH

filters or their enclosures. Erlenmeyer flasks in a chilled water bath at 10 °C were positioned between the filter and the downstream MFCs for water removal prior to metering. Flowrates of the partially dried exhaust were corrected using the exhaust water concentrations and assuming 100% relative humidity at 10 °C after the Erlenmeyer flasks.

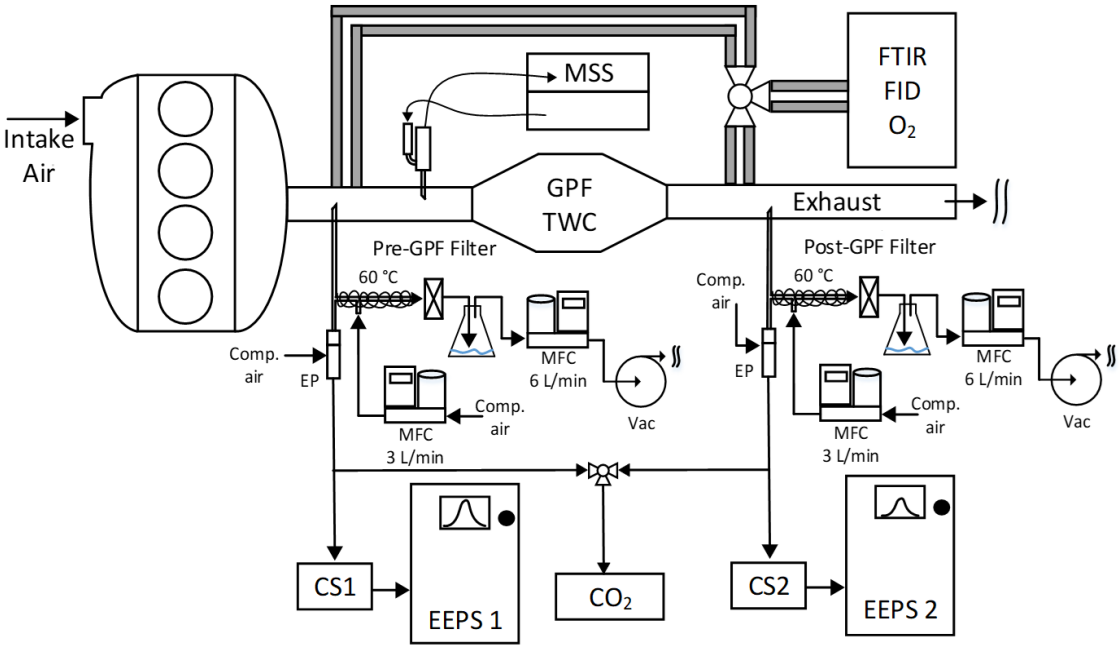

Figure 50: Diagram of emissions sampling and measurement equipment. MSS = micro soot sensor, FTIR = Fourier transform infrared spectrometer, FID = flame ionization detector, GPF = gasoline particulate filter, TWC = three-way catalyst, EP = ejector pump diluter, MFC = mass flow controller, Vac = vacuum pump, CS = catalytic stripper, EEPS = engine exhaust particle sizer.

Two KOH filters (pre- and post-GPF) were loaded simultaneous for each engine condition and fuel. Each engine condition was tested three times for each fuel for a total of 24 filters loaded (2 filter sample locations x 2 engine conditions x 2 fuels x 3 runs = 24 filters). One testing campaign was performed for each fuel. A testing campaign consisted of an engine start and warm-up, a GPF regeneration, three KOH filter loadings for the stoichiometric condition, and three KOH filter loadings for the lean stratified condition

with a GPF regeneration and 15-minute stabilization period between each loading. Filters were loaded for 45 minutes at a flowrate of 6 SLPM. GPF regenerations were performed by operating the engine at high speed and load (3000 rpm, 10 bar BMEP) until the GPF inlet and outlet gas temperatures were > 600 °C followed by a fuel cut to oxidize soot loaded on the GPF.

Filter impregnation, extraction, and carboxylic acid derivatization and analysis were performed as in the diesel study, with the following modifications. All filters were impregnated with KOH. Following derivatization, the samples were treated with sodium bicarbonate solution (2% w/v, 500 μL) and extracted with diethyl ether-*n*-hexane (1:1 v/v, 300 μL). The two layers were gently mixed by inversion, venting any pressure build up, followed by further mixing by vortex agitation (30 s). The samples were centrifuged (14,000 RPM, 3 min) to separate the layers and aliquots (2×100 μL) from the organic (top) layer transferred into prelabeled microfuge. The combined organic extracts (200 μL) were dried over anhydrous sodium sulfate. The dry extracts (100 μL) were transferred to glass inserts (200 μL) in an HPLC vial (2 mL), which was capped and stored at -20°C prior to analysis by gas chromatography-tandem mass spectrometry (GC-MS), unless they were analyzed immediately after derivatization. The mass spectrometer was operated in “Scan mode”; mass range, 40-500 amu. The lower limit of detection (LOD) of the method, defined as three times the noise level, varied as a function of the acid is given in Table 12.

Table 12: Lower limit of detection (LOD) for all acids measured in the experimental study including emissions index (mg/kg-fuel) for each engine condition.

Mode Acid	(µg/ml)	(ng/injection)	Stoich (mg/kg_fuel)	Strat (mg/kg_fuel)
Formic	4.04	16.2	1.59	2.47
Acetic	2.94	11.8	1.16	1.80
Propanoic	1.15	4.59	0.451	0.700
Butanoic	4.73	18.9	1.86	2.88
Oxalic	0.657	2.63	0.258	0.401
Propanedioic	0.0812	0.325	0.0319	0.0495
2-Butenedioic (Z)	1.08	4.33	0.425	0.660
Butanedioic	0.206	0.825	0.0810	0.126
2-Butenedioic (E)	0.683	2.73	0.268	0.417
Pentatedioic	0.162	0.650	0.0638	0.0991
Hexanedioic	0.168	0.672	0.0660	0.103

6.2.3 Results and Discussion

Gas phase emissions from each engine condition, fuel, and sample location are shown in Figure 51. The catalytic GPF converted greater than 97% of the hydrocarbon (THC) emissions for both fuels and for the stoichiometric condition and greater than 90 % for lean stratified conditions. It also converted more than 99 % of the CO emissions for all conditions. However, the GPF only removed approximately 50% of the NO_x emissions from the stoichiometric condition and did not convert NO_x emissions for the lean conditions. This was expected from the stoichiometric condition because the equivalence ratio was held constant instead of dithered for effective NO_x removal as is done in production engine calibration. It was also expected for the lean condition because TWCs rely on CO for the reduction of NO. Under lean conditions, the CO is oxidized in the TWC by the excess O_2 resulting in CO being unavailable for the reduction of NO. However, NO_x control was not the subject of this research, and as such, will not be considered further here.

There were no discernable differences between gas phase emissions of E0 and E10 for any given engine mode.

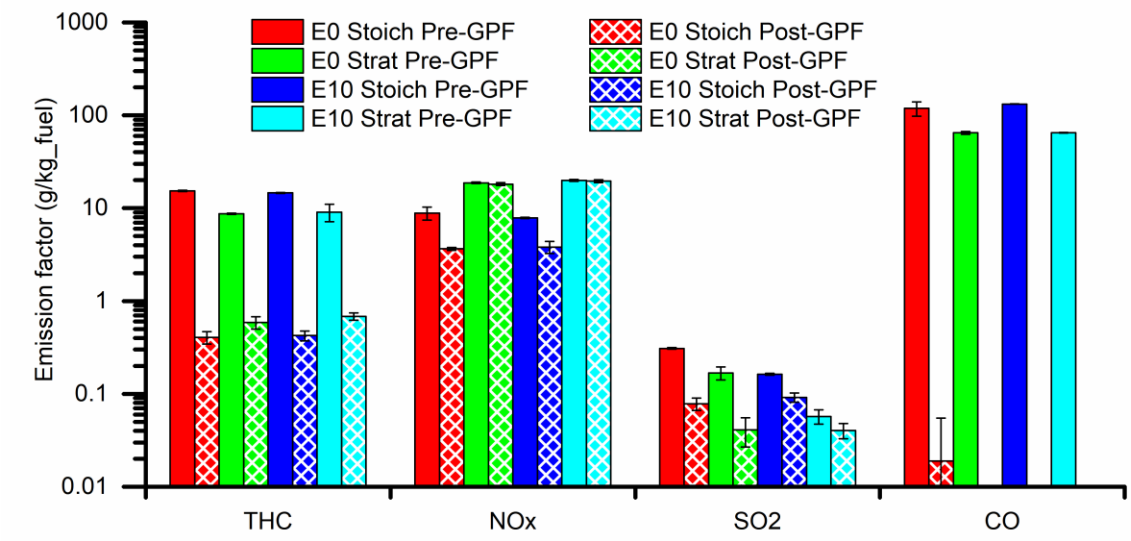

Figure 51: Gas phase emissions from each engine condition, fuel, and sample location measured by the AVL emissions bench. Error bars represent one standard deviation from the mean of the three runs.

Particle size distributions from each engine condition, fuel, and sample location are shown in Figure 52. The lean stratified engine condition produced high accumulation mode (soot) particles, two orders of magnitude higher than the stoichiometric condition running at the same speed and load, as detailed in previous chapters. The E0 and E10 lean stratified conditions had similar pre-GPF PSDs. However, the deviation in the curves from particle diameter (Dp) = 80 nm to Dp = 300 nm represents 50% particle mass emissions increase for the E0 fuel at this condition. The soot emissions from the lean stratified conditions were 45.9 ± 14.8 mg/kg_{fuel} and 30.6 ± 5.36mg/kg_{fuel} for the E0 and E10 fuels respectively. This is a predictable fuel effect of the ethanol diluting the soot producing aromatics and is described in previous chapters. An interesting consequence of this is that the average post-GPF concentrations were higher for the E10 fuel over the 45 minute KOH filter loading

period. Correspondingly, since the E0 pre-GPF soot concentrations were higher, the GPF loaded faster, the GPF filtration efficiency increased, and the E0 post-GPF concentrations dropped. This resulted in the E10 fuel having higher average post-GPF particle concentrations than E0 even though the E10 pre-GPF concentrations were lower.

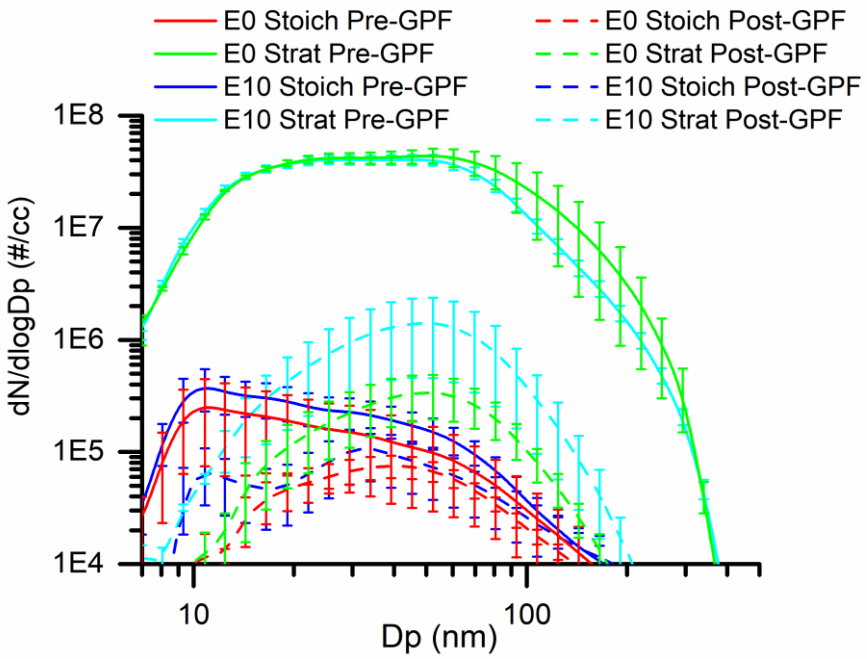

Figure 52: Solid particle size distributions for each engine condition, fuel, and sample location measured by the two EEPS's. Error bars represent one standard deviation from the mean of three runs.

The acid emissions from each condition, fuel, and sample location are shown in Figure 53. Butanoic and hexanedioic are omitted from the figure because all concentrations for these acids were below the LOD. The first thing to note is that there are detectable monocarboxylic and dicarboxylic acids from all conditions tested. The simplest carboxylic acid, formic acid, was in the highest abundance of the carboxylic acids for all conditions with the exception that it was not detected from the E10 Stoich Post-GPF condition. The simplest dicarboxylic acid, oxalic acid, was in the highest abundance of the dicarboxylic

acids and was detectable for all conditions. The dicarboxylic acids likely form through similar mechanisms as monocarboxylic acids: during the combustion event in the presence of acid precursors such as aldehydes, OH radicals, H atoms, and opened aromatic rings. Investigation of detailed pathways for these acids should be studied to fully understand their formation.

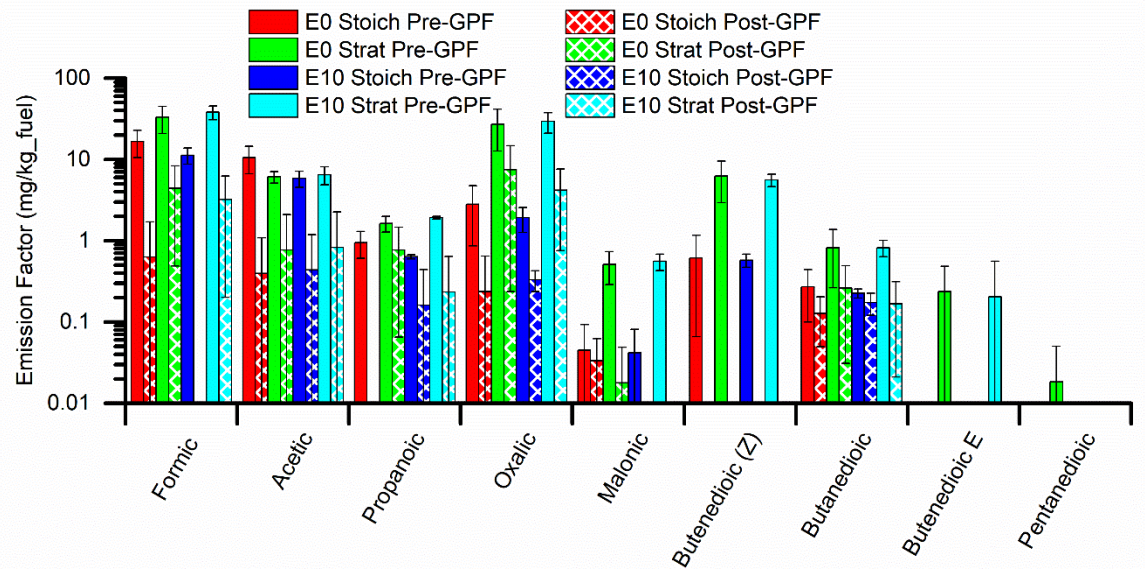

Figure 53: Acid emissions in emission factors (EF) for each engine condition, fuel, and sample location from the GC-MS analysis. Error bars represent on standard deviation from the mean of three samples.

Compared to results of the diesel study, the carboxylic acid emissions from the GDI were generally one order of magnitude below the concentration emitted by the diesel engine. Formic acid emission factors ranged from 10 to 1000 mg/kg$_{fuel}$ for diesel, while in the current study, the formic acid concentrations from the GDI engine ranged from 1 to 100 mg/kg$_{fuel}$. The trend is the same for acetic and propanoic acids. Dicarboxylic acid concentrations from the GDI engine were also an order of magnitude lower than what was previously measured from the diesel engine, except for oxalic acid. Oxalic acid was emitted from the diesel engine at a rate of 21.9 ± 12.2 mg/kg$_{fuel}$ for the early low temperature

combustion (ELTC) mode. In the current study, oxalic acid was found to be emitted from the GDI engine at rates of 27.1 ± 14.4 mg/kg_{fuel} and 29.4 ± 8.26 mg/kg_{fuel} for the E0 and E10 fuels, respectively from the lean stratified condition.

The comparable oxalic acid concentrations of the ELTC and lean stratified modes is interesting because of the similarities in fuel delivery strategy between these modes. The ELTC mode employed a single fuel injection at 28 °bTDC, which is much earlier than the main injection for conventional diesel. The lean stratified GDI condition employed three injections between 39 and 20 °bTDC, with the two main injections at 39 and 29 °bTDC. However, in the diesel study, both maleic and butanedioic acids were in higher concentration that oxalic, whereas oxalic was the highest from GDI. Still, similarities appear between the diesel ELTC and lean stratified conditions in terms of the type of acids formed.

Kawamura and Kaplan measured oxalic acid concentrations that would correspond to emission factors in the range of 0.22 to 0.34 mg/kg_{fuel} for a gasoline vehicle and 0.58 to 0.89 mg/kg_{fuel} for a diesel vehicle, assuming the same conditions as in the current study. In the current work, emission factors ranged from 0.24 to 29.4 mg/kg_{fuel} for oxalic acid and 0.16 to 1.64 mg/kg_{fuel} for propanoic acid. The wide range of acid emission rates indicates high sensitivity to both engine condition and sampling method, factors not considered in earlier studies.

Table 13 shows the ratios of lean stratified to stoichiometric acid emission factors for each fuel and sample location. Acid emission factors were generally much higher for the lean stratified condition compared to the stoichiometric condition for both fuels and sample locations. The exceptions were E0 Pre-GPF for acetic acid, E0 Post-GPF for malonic acid,

and E10 Post-GPF for butanedioic acid. The ratio is generally higher for dicarboxylic acids with many ratios corresponding to an order of magnitude increase in diacid emissions. The monoacids showed lower strat/stoich ratios, ranging from 1.43 to 4.50, while the diacid ratios ranged from 6.77 to 11.37, indicating that diacid emissions are more sensitive to engine condition than monoacids. Zervas et al. showed that decreasing the equivalence ratio increased the emission of formic acid from a SI engine, while acetic acid emissions where highest at stoichiometry for oxygenated fuels [93]. These findings agree with the results of the current study.

Table 13: Ratio of the acid emission factors for lean stratified engine condition to the stoichiometric engine condition for both fuels and both sample locations. Inf. = detectable strat concentration but stoich concentration below LOD, - = both strat and stoich below LOD.

Strat/Stoich	E0 Pre-GPF	E0 Post-GPF	E10 Pre-GPF	E10 Post-GPF
Formic	1.98	7.06	3.38	inf.
Acetic	0.58	1.94	1.11	1.89
Propanoic	1.72	inf.	3.02	1.45
Butanoic	-	-	-	-
Oxalic	9.65	31.57	15.27	12.58
Malonic	11.38	0.53	13.27	-
Butenedioic (Z)	10.16	-	9.69	-
Butanedioic	3.03	2.06	3.64	0.96
Butenedioic (E)	inf.	-	inf.	-
Monoacid Avg.	1.43	4.50	2.50	1.67
Diacid Avg.	8.55	11.39	10.47	6.77
Total Avg.	5.50	8.63	7.05	4.22

The link between the lean stratified condition and higher acid emissions is likely related to the charge mixture preparation. The same mechanism for high soot production from the lean stratified could be the cause of higher acid emissions. Inhomogeneity of the fuel and air charge mixture and the presence of fuel rich regions in the cylinder leads to fuel

pyrolysis, soot formation, incomplete combustion, and potentially increased acid production.

The ratio of E0 to E10 acid emission factors are shown in Table 14 for each engine condition and sample location. The E0 fuel produced higher acid concentrations for all acids for the stoichiometric pre-GPF condition compared to the E10 fuel. The E0 fuel produced on average 60% and 20% higher emission factors of carboxylic acids and dicarboxylic acids respectively compared to the E10 fuel for the stoichiometric condition pre-GPF. However, for the lean stratified pre-GPF condition, almost all emission factors were slightly lower for the E0 fuel. All monoacid emissions were lower for the E0 fuel for the lean stratified pre-GPF condition. The effect of the fuel ethanol concentration was mixed for the lean stratified pre-GPF condition, with the E0 pre-GPF emission factors not deviating more than 15% from the E10 pre-GPF emission factors. These results show that pre-GPF acid emissions are much more sensitive to engine condition than they are to fuel ethanol concentration, at least up to the E10 blending level.

The varying trend in acid emissions between stoichiometric and lean conditions for oxygenated and non-oxygenated fuels may be explained by the total unburned hydrocarbon emissions. The THC emissions for the stoichiometric condition were 15.4 ± 0.24 g/kg-fuel for the non-oxygenated fuel and 14.6 ± 0.18 g/kg-fuel for the oxygenated fuel (5% higher for non-oxygenated fuel). This indicates that there was more complete combustion for the oxygenated fuel. Because acids are formed from products of incomplete combustion, it explains why the acid concentrations were higher for the non-oxygenated fuel for the stoichiometric condition. For the lean stratified condition, the THC emissions were 8.71 ± 0.16 and 9.09 ± 1.92 g/kg-fuel for the non-oxygenated and oxygenated fuel respectively

(4% higher for the oxygenated fuel). This explains why the oxygenated fuel had generally higher acid emissions than the non-oxygenated fuel for the lean stratified condition. The large variance in THC emissions from the oxygenated fuel for the lean stratified condition may explain why the E0/10 ratios were mixed for the diacids.

Table 14: Ratio of E0 acid emission factor to E10 acid emission factor for each engine condition and sample location. inf. = detectable E0 concentration but E10 concentration below LOD, - = both E0 and E10 below LOD.

E0/E10	Stoich Pre-GPF	Stoich Post-GPF	Strat Pre-GPF	Strat Post-GPF
Formic	1.48	inf.	0.87	1.37
Acetic	1.81	0.91	0.94	0.93
Propanoic	1.50	-	0.85	3.27
Oxalic	1.46	0.71	0.92	1.79
Malonic	1.07	inf.	0.92	inf.
Butenedioic (Z)	1.07	-	1.12	-
Butanedioic	1.20	0.73	1.00	1.57
Butenedioic (E)	-	-	1.15	-
Monoacid Avg.	1.60	0.91	0.89	1.86
Diacid Avg.	1.20	0.72	1.02	1.68
Total Avg.	1.37	0.79	0.97	1.79

Fuel ethanol concertation has opposite effects for the stoichiometric and lean stratified post-GPF conditions. As shown in Table 14, the E0 fuel produced lower acid emissions post-GPF for the stoichiometric condition but higher acid emissions for the lean stratified condition. Table 15 shows the GPF acid conversion efficiency for each fuel and engine condition. The GPF acid conversion efficiency is defined as

$$\eta_{GPF} = 1 - {EF_{x,post-GPF}}\Big/{EF_{x,pre-GPF}} \qquad \text{Eq. 6.2}$$

where η_{GPF} is the GPF conversion efficiency, $EF_{x,post\text{-}GPF}$ is the emission factor of acid x at the post-GPF location, and $EF_{x,pre\text{-}GPF}$ is the emission factor of acid x at the pre-GPF location. For the E0 stoichiometric condition, the GPF converted a much higher fraction of

monoacids (97%) than diacids (67%). However, for the E0 lean stratified condition, the GPF converted a higher fraction of diacids than monoacids. The trend continued for the E10 conditions.

It is currently unclear what is causing the opposing trends between the monoacids/diacids and stoichiometric/lean stratified conditions on the catalyzed GPF. The differences of interest in engine condition as they relate to GPF conversion efficiency are catalyst temperature and exhaust oxygen concentration. For the stoichiometric conditions, the oxygen concentration is ~0%, and the GPF inlet and outlet gas temperatures are ~ 420 °C and 492 °C respectively. For the lean stratified conditions, the oxygen concentration is ~8.2%, and the GPF inlet and outlet gas temperatures are ~ 382 °C and 398 °C respectively. These are temperatures and oxygen concentrations are well within normal operating conditions of a catalytic GPF. It appears that conversion of the monoacids is favored at the higher GPF temperature, low oxygen concentration condition, and conversion of the diacids is favored at the lower GPF temperature and higher oxygen concentration.

Table 15: GPF acid conversion efficiency for each fuel and engine condition.

GPF Conversion Eff.	E0 Stoich	E0 Strat	E10 Stoich	E10 Strat
Formic	0.96	0.87	1.00	0.92
Acetic	0.96	0.87	0.93	0.87
Propanoic	1.00	0.53	0.75	0.88
Oxalic	0.92	0.72	0.83	0.86
Malonic	0.26	0.97	1.00	1.00
Butanedioic	0.53	0.68	0.23	0.80
Butenedioic (E)	-	1.00	-	1.00
Pentanedioic	-	1.00	-	-
Monoacid Avg.	0.97	0.76	0.89	0.89
Diacid Avg.	0.67	0.89	0.76	0.93
Total Avg.	0.80	0.85	0.82	0.92

Chapter 7 Conclusions and Suggested Future Work

The continued effort to reduce both particulate matter and greenhouse gas emissions poses a challenge for GDI engine designers because efficiency boosting injection strategies of GDI engines also results in increased particulate matter production. Synergies between fuel formulation, fuel injection strategy, and GPF implementation must be identified and systematically applied to meet emissions reduction goals. The current body of work identified both problematic and promising GDI operating conditions that can be used to meet these goals.

7.1 Engine-out PM Emission from Lean and Stoichiometric GDI

Steady state engine conditions were evaluated using stoichiometric, lean homogeneous, and lean stratified operation modes in a GDI engine. The steady state lean stratified conditions produced an excessive amount soot and PM/PN emissions and only offered an efficiency advantage over lean homogeneous at very low load. The steady state stoichiometric conditions showed broad, flat particle size distributions which are unique compared to the traditional bimodal distribution commonly associated with engine combustion. The steady state lean homogeneous conditions showed favorable fuel efficiency across the operation range and relatively low PN and PM emissions, but a very high fraction of unregulated solid PN between 10 and 23 nm. Stoichiometric PN to PM ratio were in good agreement to previous studies. However, both lean combustion modes showed higher particle number to mass ratios indicating more small particles per unit aerosol mass.

High ash particle concentrations found in all engine modes, but especially in lean homogeneous operation demonstrates that oil control is important for mitigating impacts

on downstream gasoline particulate filters (GPF) from which ash particles are cannot be removed during filter regeneration. Because sub-23 nm particles are not regulated under current legislation, the high ash particle concentrations are of even greater concern if lean homogenous modes are to be employed in non-GPF equipped engines. The results of this study illustrate that ash particles need to be considered and better characterized in support of designing and operating lean GDI engines. Suggested future work includes conducting elemental analysis on the solid nucleation mode produced by GDI engines.

7.2 Fuel Effects on Lean and Stoichiometric GDI PM Emissions

Solid, engine-out PN and PM mass emissions were measured from steady state stoichiometric, lean homogenous, and lean stratified engine conditions from a GDI engine fueled by seven different fuel formulations using clean fuel injectors. The E50 fuel showed exceptional sensitivity to engine operating condition, producing the highest PM emissions of any fuel for high load, lean homogeneous conditions and the lowest PM emissions of any fuel for lean stratified conditions. This can be attributed to its high HOV and low aromatics concentrations. For flex-fuel vehicles equipped with on-board ethanol concentration sensors, the results of this study show that it would be beneficial to run high ethanol content fuel in the lean stratified condition at low load, and the stoichiometric at high load

The dominant influence on particle formation is charge composition, which is influenced by fuel properties. However, at either end of the mixture formation spectrum, fuel properties are overshadowed by the prevailing engine conditions. In this work, aside from the E50 fuel, there was minimal fuel influence observed on PM emissions when the charge mixture was homogenous, resulting in little particle formation, such as in the

stoichiometric conditions and the lower load lean homogeneous conditions. There was also minimal fuel influence on the other end of the mixture spectrum, when there was so much fuel stratification that liquid droplets existed when combustion began, resulting in droplet burning or pool fires. With a moderately stratified charge composition, like in the higher load lean homogeneous conditions, there was a clear correlation between PN and PM mass and the PM Index. This indicates that the PM Index is only applicable when there is significant accumulation mode particle concentration and only when the mixture is not so stratified that it results in fuel droplet burning.

This work also illustrates the importance of mitigating injector fouling for low PN and PM emissions from GDI engines. Comparing the same engine conditions with uncleaned fuel injectors and the baseline fuel, the stoichiometric conditions produced an order of magnitude higher PN concentrations than with clean injectors. This indicates that injector fouling is the dominant source of PM emissions for stoichiometric conditions, where the mixture would otherwise be well-mixed and homogenous if not for the deposits. The lean homogeneous and lean stratified conditions produced similar concentrations as with uncleaned injectors, indicating that fuel stratification from the late injection was the primary source of the particle formation, or that the injector deposits formed rapidly under the lean conditions, reaching levels seen with uncleaned injectors. If the latter was the case, it would indicate that late injection accelerates injector fouling by leaving liquid fuel on the injector late in the engine cycle. Future work that studies injector fouling rates under early and late injection strategies would be useful to test this hypothesis.

Driving cycle testing was demonstrated with an engine on an engine dynamometer using a novel, software programmed virtual drivetrain. The virtual drivetrain commanded

the engine to operate under speed and load conditions as if it were performing the driving cycle. Calculated vehicle speed was well within the acceptable limits of the driving cycle, and engine speed and load traces were comparable to that of a similarly sized engine running the driving cycle on a chassis dynamometer. This development allowed PM emission testing and GPF performance evaluation over a driving cycle with the use of an engine dynamometer. The virtual drivetrain offers an option for testing driving cycles without the expense and footprint of a vehicle on a chassis dynamometer. This expands the limits for what can be done at certain research facilities and can reduce engine calibration and emission control development time in corporate engineering departments.

PM emissions were measured pre- and post-GPF with six different fuel formulations over the first 200 seconds of the WLTP cycle. The results showed high PM emissions from all fuels and illustrated why this challenging section of the regulatory cycle is important for mitigating emissions. Each fuel produced repeatable engine-out PM emissions. The high aromatics fuel produced the highest engine-out particle concentrations, approximately a factor of 2 higher than the E50 fuel. However, the average post-GPF PM emissions were not significantly different between fuels. The post-GPF emissions were more dependent on GPF loading state than engine-out PM emissions. Fuels that emitted high engine-out PM rapidly loaded the filter and increased its filtration efficiency, while the lower engine-out emitting fuels did not effectively load the filter over the test, and therefore did not benefit from increased filtration efficiency. These results show that current and future PM emission standards could be met more easily through optimized control of GPF loading state. It is not clear whether the loading state of the GPF will be a controlled parameter in regulatory testing of PM. Optimizing GPF loading state is a complicated control strategy. However,

with proper engine calibration, emissions limits are attainable irrespective of fuel type. Suggested future work includes testing the engine over the entire drive cycle and using lean strategies. This could include development of a combustion mode switching algorithm that determine the optimum mode based on engine load demand and GPF loading state.

7.3 A novel, in-situ soot oxidation measurement method

A novel, in-situ soot oxidative reactivity measurement method was demonstrated with a catalytic GPF using three oils to induce varying soot oxidation rates. The results showed that there is a strong catalytic effect of the GPF wash-coating on soot oxidation rates. Specifically, it showed that the soot oxidation rate is dependent on the soot concentration and level of soot loading on the filter due to the surface to volume ratio effects. The specific soot oxidation rates were on the same order of magnitude as the limited data that is reported in literature for GDI soot. However, oxidation rates in this study were equal or higher to literature-reported TGA oxidation rates at much higher temperatures, further demonstrating the influence of the GPF catalyst on oxidation rates. This online method can provide valuable information for soot loading models that optimize filter performance. Suggested future work includes analyzing soot samples from the same engine conditions and analyzing it with TGA to compare with the novel method. Additionally, this method could be applied over several GPF temperature ranges in order to obtain Arrhenius-type equations and calculate activation energies for soot containing specific oil additive ash. Furthermore, this method could be modified to determine ash loading on a GPF by tracking the change in clean filter filtration efficiency.

7.4 Dicarboxylic Acid Emissions from Aftertreatment Equipped GDI and Diesel Engines

Dicarboxylic acids were measured from both modern GDI and diesel engines equipped with after treatment systems. Engine-out GDI acid emissions were approximately one order of magnitude lower than engine-out diesel emissions. Acid emissions were very sensitive to engine condition; the lean stratified engine condition produced much higher acid emissions than stoichiometric conditions and the ELTC diesel mode produced much more acids than the conventional diesel mode, which produced no diacids. The difference in acid emissions from E0 gasoline was not significantly different than that of E10 gasoline. The catalytic GPF eliminated between 80 and 92 percent of all carboxylic and dicarboxylic acid emissions, depending on engine condition and fuel ethanol concentration. The stoichiometric condition had a worse GPF diacid conversion efficiency than the lean stratified condition. However, the high conversion efficiency of the lean stratified condition was not able to offset the high acid emissions from the condition, and the post-GPF diacid emissions were generally higher from the lean stratified condition.

This work definitively shows that dicarboxylic acids are emitted from both GDI and diesel engines. Although the aftertreatment systems eliminated most dicarboxylic acids, a significant fraction penetrated the emission control device under certain conditions. It is currently unclear if the ATS acid emission rates are at acceptable levels, or if there is substantial relative diacid contribution to atmospheric aerosols from primary sources such as GDI engines. Future work involving assessment of the contribution of these acids to atmospheric aerosols is required to understand if improvements in catalysts are warranted to mitigate these acid emissions.

Although dicarboxylic acids are known to affect secondary organic aerosol formation in the atmosphere, our results suggest that it is unlikely that they participate in primary particle nucleation in dilute engine exhaust because they were not measured in the un-coated filter samples. Further work is needed to understand the gas to particle conversion of dicarboxylic acids. Perhaps the timescale under which this process occurs is longer than that of the transit time in a traditional engine exhaust sampling system. Other future work includes measuring diacids at additional engine conditions, measuring higher molecular weight species, and proposing combustion mechanisms for formation of these acids.

Bibliography

[1] Liang B, Ge Y, Tan J, Han X, Gao L, Hao L, et al. Comparison of PM emissions from a gasoline direct injected (GDI) vehicle and a port fuel injected (PFI) vehicle measured by electrical low pressure impactor (ELPI) with two fuels: Gasoline and M15 methanol gasoline. J Aerosol Sci 2013;57:22–31. doi:10.1016/j.jaerosci.2012.11.008.

[2] Saliba G, Saleh R, Zhao Y, Presto AA, Lambe AT, Frodin B, et al. Comparison of Gasoline Direct-Injection (GDI) and Port Fuel Injection (PFI) Vehicle Emissions: Emission Certification Standards, Cold-Start, Secondary Organic Aerosol Formation Potential, and Potential Climate Impacts. Environ Sci Technol 2017;51:6542–52. doi:10.1021/acs.est.6b06509.

[3] Maricq MM, Podsiadlik DH, Chase RE. Examination of the size-resolved and transient nature of motor vehicle particle emissions. Environ Sci Technol 1999;33:1618–26. doi:10.1021/es9808806.

[4] Szybist JP, Youngquist AD, Barone TL, Storey JM, Moore WR, Foster M, et al. Ethanol blends and engine operating strategy effects on light-duty spark-ignition engine particle emissions. Energy and Fuels 2011;25:4977–85. doi:10.1021/ef201127y.

[5] Graskow B, Kittelson D. Exhaust Particulate Emissions from a Direct Injection Spark Ignition Engine. SAE Tech Pap 1999;1999-01–11. doi:10.4271/1999-01-1145.

[6] Chen L, Liang Z, Zhang X, Shuai S. Characterizing particulate matter emissions from GDI and PFI vehicles under transient and cold start conditions. Fuel

2017;189:131–40. doi:10.1016/j.fuel.2016.10.0550016-2361.

[7] Braisher M, Stone R, Price P. Particle Number Emissions from a Range of European Vehicles. SAE Int 2010. doi:10.4271/2010-01-0786.

[8] Zervas E, Dorlhene P, Daviau R, Dionnet B. Repeatability of fine particle measurement of diesel and gasoline vehicles exhaust gas. SAE Tech 2004;2004-01–19. doi:10.4271/2004-01-1983.

[9] Mathis U, Mohr M, Forss AM. Comprehensive particle characterization of modern gasoline and diesel passenger cars at low ambient temperatures. Atmos Environ 2005;39:107–17. doi:10.1016/j.atmosenv.2004.09.029.

[10] CARB. “LEV III” AMENDMENTS TO THE CALIFORNIA GREENHOUSE GAS AND CRITERIA POLLUTANT EXHAUST AND EVAPORATIVE EMISSION STANDARDS AND TEST PROCEDURES AND TO THE ON-BOARD DIAGNOSTIC SYSTEM REQUIREMENTS FOR PASSENGER CARS, LIGHT- DUTY TRUCKS, AND MEDIUM-DUTY VEHICLES 2012:1–161.

[11] COMMISSION REGULATION (EU) No 459/2012. Off J Eur Union 2012.

[12] Lippmann M, Ito K, Nádas a, Burnett RT. Association of particulate matter components with daily mortality and morbidity in urban populations. Res Rep Health Eff Inst 2000:5–72, discussion 73-82.

[13] Li P, Xin J, Wang Y, Li G, Pan X, Wang S, et al. Association between particulate matter and its chemical constituents of urban air pollution and daily mortality or morbidity in Beijing City. Environ Sci Pollut Res 2014;22:358–68. doi:10.1007/s11356-014-3301-1.

[14] Tanaka D, Uchida R, Noda T, Kolbeck A, Henkel S, Hardalupas Y, et al. Effects of

Fuel Properties Associated with In-Cylinder Behavior on Particulate Number from a Direct Injection Gasoline Engine. SAE Tech Pap 2017;2017-01–10. doi:10.4271/2017-01-1002.Copyright.

[15] Aikawa K, Sakurai T, Jetter JJ. Development of a Predictive Model for Gasoline Vehicle Particulate Matter Emissions. SAE Tech Pap 2010;3:610–22. doi:10.4271/2010-01-2115.

[16] Leach F, Stone R, Richardson D. The Influence of Fuel Properties on Particulate Number Emissions from a Direct Injection Spark Ignition Engine. SAE Int 2013:10. doi:10.4271/2013-01-1558.

[17] Khalek IA, Bougher T, Jetter JJ. Particle Emissions from a 2009 Gasoline Direct Injection Engine Using Different Commercially Available Fuels. SAE Int J Fuels Lubr 2010;3:623–37. doi:10.4271/2010-01-2117.

[18] Chan TW. The Impact of Isobutanol and Ethanol on Gasoline Fuel Properties and Black Carbon Emissions from Two Light-Duty Gasoline Vehicles. SAE Tech Pap 2015-01-1076 2015. doi:10.4271/2015-01-1076.

[19] Storey JM, Barone T, Norman K, Lewis S. Ethanol Blend Effects On Direct Injection Spark-Ignition Gasoline Vehicle Particulate Matter Emissions. SAE Int J Fuels Lubr 2010;3:2010-01–2129. doi:10.4271/2010-01-2129.

[20] Maricq MM, Szente JJ, Jahr K. The impact of ethanol fuel blends on PM emissions from a light-duty GDI vehicle. Aerosol Sci Technol 2012;46:576–83. doi:10.1080/02786826.2011.648780.

[21] FiorMarkets. Gasoline Particulate Filters Market by Type (Cordierite GPF , Ceramic GPF), Application (Passenger Cars , Commercial Vehicles , Off-Road

Vehicles , LCV (Light Commercial Vehicle)), Region , Global Industry Analysis , Market Size , Share , Growth , Tr. 2020.

[22] Lambert C, Chanko T, Dobson D, Liu X, Pakko J. Gasoline Particle Filter Development. Emiss Control Sci Technol 2017;3:105–11. doi:10.1007/s40825-016-0055-x.

[23] Choi S, Seong H. Lube oil-dependent ash chemistry on soot oxidation reactivity in a gasoline direct-injection engine. Combust Flame 2016;174:68–76. doi:10.1016/j.combustflame.2016.09.019.

[24] Choi S, Seong H. Oxidation characteristics of gasoline direct-injection (GDI) engine soot: Catalytic effects of ash and modified kinetic correlation. Combust Flame 2015;162:2371–89. doi:10.1016/j.combustflame.2015.02.004.

[25] Blando JD, Turpin BJ. Secondary organic aerosol formation in cloud and fog droplets: A literature evaluation of plausibility. Atmos Environ 2000;34:1623–32. doi:10.1016/S1352-2310(99)00392-1.

[26] Warneck P. In-cloud chemistry opens pathway to the formation of oxalic acid in the marine atmosphere. Atmos Environ 2003;37:2423–7. doi:10.1016/S1352-2310(03)00136-5.

[27] Ervens B, Feingold G, Clegg SL, Kreidenweis SM. A modeling study of aqueous production of dicarboxylic acids: 2. Implications for cloud microphysics. J Geophys Res D Atmos 2004;109:1–12. doi:10.1029/2004JD004575.

[28] Carlton AG, Turpin BJ, Altieri KE, Seitzinger S, Reff A, Lim H, et al. Atmospheric oxalic acid and SOA production from glyoxal : Results of aqueous photooxidation experiments. Atmos Environ 2007;41:7588–602.

doi:10.1016/j.atmosenv.2007.05.035.

[29] Deshmukh DK, Deb MK, Hopke PK, Tsai YI. Seasonal Characteristics of water-soluble dicarboxylates associated with PM10 in the urban atmosphere of Durg City, India. Aerosol Air Qual Res 2012;12:683–96. doi:10.4209/aaqr.2012.02.0040.

[30] Kawamura K, Kaplan IR. Motor Exhaust Emissions as a Primary Source for Dicarboxylic Acids in Los Angeles Ambient Air. Environ Sci Technol 1987;21:105–10. doi:10.1021/es00155a014.

[31] Brunt MFJ, Rai H, Emtage AL. The Calculation of Heat Release Energy from Engine Cylinder Pressure Data 1998. doi:10.4271/981052.

[32] Egnell R. Combustion Diagnostics by Means of Multizone Heat Release Analysis and NO Calculation. SAE Tech Pap 1998. doi:981424.

[33] Quader AA. Lean Combustion and the Misfire Limit in Spark Ignition Engines. SAE Tech Pap 741055 1974:23. doi:10.4271/741055.

[34] Kittelson D. Engines and Nanaoparticles: A Review. J Aerosol Sci 1998;29:575–88.

[35] Abdul-Khalek I, Kittelson D, Brear F. The Influence of Dilution Conditions on Diesel Exhaust Particle Size Distribution Measurements. SAE Tech Pap 1999:1–9. doi:10.4271/1999-01-1142.

[36] Liu ZG, Vasys VN, Dettmann ME, Schauer JJ, Kittelson DB, Swanson J. Comparison of strategies for the measurement of mass emissions from diesel engines emitting ultra-low levels of particulate matter. Aerosol Sci Technol 2009;43:1142–52. doi:10.1080/02786820903219035.

[37] Frenklach M. Reaction mechanism of soot formation in flames. Phys Chem Chem Phys 2002;4:2028–37. doi:10.1039/b110045a.

[38] Tree DR, Svensson KI. Soot processes in compression ignition engines. Prog Energy Combust Sci 2007:272–309. doi:10.1016/j.pecs.2006.03.002.

[39] Argachoy C, Pimenta AP. Phenomenological Model of Particulate Matter Emission from Direct Injection Diesel Engines. J Brazilian Soc Mech Sci Eng 2005;XXVII:266–73. doi:10.1590/S1678-58782005000300008.

[40] Friedlander SK. Dust, Smoke and Haze. Second Edi. New York: Oxford University Press; 2000.

[41] Gidney JT, Twigg M V., Kittelson DB. Effect of organometallic fuel additives on nanoparticle emissions from a gasoline passenger car. Environ Sci Technol 2010;44:2562–9. doi:10.1021/es901868c.

[42] Mamakos A, Martini G, Marotta A, Manfredi U. Assessment of different technical options in reducing particle emissions from gasoline direct injection vehicles. J Aerosol Sci 2013;63:115–25. doi:10.1016/j.jaerosci.2013.05.004.

[43] Mayer AC, Ulrich A, Czerwinski J, Mooney JJ. Metal-Oxide Particles in Combustion Engine Exhaust. SAE Int 2010. doi:10.4271/2010-01-0792.

[44] Giechaskiel B, Vanhanen J, Väkevä M, Martini G. Investigation of vehicle exhaust sub-23 nm particle emissions. Aerosol Sci Technol 2017;51:626–41. doi:10.1080/02786826.2017.1286291.

[45] Jung H, Kittelson DB, Zachariah MR. The influence of a cerium additive on ultrafine diesel particle emissions and kinetics of oxidation. Combust Flame 2005;142:276–88. doi:10.1016/j.combustflame.2004.11.015.

[46] Jung H, Kittelson DB, Zachariah MR. The Influence of Engine Lubricating Oil on Diesel Nanoparticle Emissions and Kinetics of Oxidation. SAE Tech Pap

2003;2003-01–31. doi:10.4271/2003-01-3179.

[47] Kittelson DB, Dolan DF, Diver RB, Aufderheide E. Diesel exhaust particle size distributions - Fuel and additive effects. SAE Tech Pap 1978;87:3011–22. doi:10.4271/780787.

[48] Kasper M, Sattler K, Siegmann K, Matter U, Siegmann HC. The influence of fuel additives on the formation of carbon during combustion. J Aerosol Sci 1999;30:217–25. doi:10.1016/S0021-8502(98)00034-2.

[49] De Filippo A, Maricq MM. Diesel nucleation mode particles: Semivolatile or solid? Environ Sci Technol 2008;42:7957–62. doi:10.1021/es8010332.

[50] Mayer AC, Ulrich A, Czerwinski J, Mooney JJ. Metal-Oxide Particles in Combustion Engine Exhaust 2010. doi:10.4271/2010-01-0792.

[51] Mayer A, Czerwinski J, Kasper M, Ulrich A, Mooney JJ. Metal Oxide Particle Emissions from Diesel and Petrol Engines. SAE Int 2012;2012-01–08. doi:10.4271/2012-01-0841.

[52] Giechaskiel B, Manfredi U, Martini G. Engine Exhaust Solid Sub-23 nm Particles: I. Literature Survey. SAE Int J Fuels Lubr 2014;7:2014-01–2834. doi:10.4271/2014-01-2834.

[53] Huang Y-W, Wu C, Aronstam RS. Toxicity of Transition Metal Oxide Nanoparticles: Recent Insights from in vitro Studies. Materials (Basel) 2010;3:4842–59. doi:10.3390/ma3104842.

[54] Oberdörster G, Sharp Z, Atudorei V, Elder A, Gelein R, Kreyling W, et al. Translocation of inhaled ultrafine particles to the brain. Inhal Toxicol 2004;16:437–45. doi:10.1080/08958370490439597.

[55] Xia W, Zheng Y, He X, Yang D, Shao H, Remias J, et al. Catalyzed Gasoline Particulate Filter (GPF) Performance : Effect of Driving Cycle , Fuel , Catalyst Coating 2017. doi:10.4271/2017-01-2366.Copyright.

[56] Boger T, Rose D, Nicolin P, Coulet B, Bachurina A. Severe Soot Oxidations in Gasoline Particulate Filter Applications. SAE Tech Pap 2018;2018-Septe:1–9. doi:10.4271/2018-01-1699.

[57] Liu X, Chanko T, Lambert C, Maricq M, Motor F. Gasoline Particulate Filter Efficiency and Backpressure at Very Low Mileage. SAE Tech Pap 2018:1–9. doi:10.4271/2018-01-1259.

[58] Chan TW, Meloche E, Kubsh J, Rosenblatt D, Brezny R, Rideout G. Evaluation of a Gasoline Particulate Filter to Reduce Particle Emissions from a Gasoline Direct Injection Vehicle. SAE Int J Fuels Lubr 2012;5:2012-01–1727. doi:10.4271/2012-01-1727.

[59] Ito Y, Shimoda T, Aoki T, Yuuki K, Sakamoto H, Kato K, et al. Next Generation of Ceramic Wall Flow Gasoline Particulate Filter with Integrated Three Way Catalyst. SAE Tech Pap 2015-01-1073 2015. doi:10.4271/2015-01-1073.Copyright.

[60] Prikhodko VY, Parks JE. Implications of Low Particulate Matter Emissions on System Fuel Efficiency for High Efficiency Clean Combustion. SAE Tech Pap 2009. doi:10.4271/2009-01-2709.

[61] Rose D, Boger T. Different Approaches to Soot Estimation as Key Requirement for DPF Applications. SAE Tech Pap 2009-01-1262 2009:01–1262. doi:10.4271/2009-01-1262.

[62] Rathod D, Onori S, Filipi Z, Hoffman M. Experimental investigation of soot

accumulation and regeneration in a catalyzed Gasoline Particulate Filter utilizing particulate quantification and gas speciation measurements. ASME 2018 Intern Combust Engine Div Fall Tech Conf ICEF 2018 2018;2. doi:10.1115/ICEF2018-9627.

[63] Dietrich M, Jahn C, Lanzerath P, Moos R. Microwave-based oxidation state and soot loading determination on gasoline particulate filters with three-way catalyst coating for homogenously operated gasoline engines. Sensors (Switzerland) 2015;15:21971–88. doi:10.3390/s150921971.

[64] Walter S, Schwanzer P, Hagen G, Haft G, Rabl HP, Dietrich M, et al. Modelling the influence of different soot types on the radio-frequency-based load detection of gasoline particulate filters. Sensors (Switzerland) 2020;20. doi:10.3390/s20092659.

[65] Higgins KJ, Jung H, Kittelson DB, Roberts JT, Zachariah MR. Size-selected nanoparticle chemistry: Kinetics of soot oxidation. J Phys Chem A 2002;106:96–103. doi:10.1021/jp004466f.

[66] Higgins KJ, Jung H, Kittelson DB, Roberts JT, Zachariah MR. Kinetics of diesel nanoparticle oxidation. Environ Sci Technol 2003;37:1949–54. doi:10.1021/es0261269.

[67] Kim SH, Fletcher RA, Zachariah MR. Understanding the difference in oxidative properties between flame and diesel soot nanoparticles: The role of metals. Environ Sci Technol 2005;39:4021–6. doi:10.1021/es048828z.

[68] Jung H, Kittelson DB, Zachariah MR. Characteristics of SME biodiesel-fueled diesel particle emissions and the kinetics of oxidation. Environ Sci Technol 2006;40:4949–56. doi:10.1021/es0515452.

[69] Al-Qurashi K, Boehman AL. Impact of exhaust gas recirculation (EGR) on the oxidative reactivity of diesel engine soot. Combust Flame 2008;155:675–95. doi:10.1016/j.combustflame.2008.06.002.

[70] Li X, Xu Z, Guan C, Huang Z. Oxidative reactivity of particles emitted from a diesel engine operating at light load with EGR. Aerosol Sci Technol 2015;49:1–10. doi:10.1080/02786826.2014.989955.

[71] Boehman AL, Song J, Alam M. Impact of biodiesel blending on diesel soot and the regeneration of particulate filters. Energy and Fuels 2005;19:1857–64. doi:10.1021/ef0500585.

[72] Yehliu K, Vander Wal RL, Armas O, Boehman AL. Impact of fuel formulation on the nanostructure and reactivity of diesel soot. Combust Flame 2012;159:3597–606. doi:10.1016/j.combustflame.2012.07.004.

[73] Song J, Alam M, Boehman AL, Kim U. Examination of the oxidation behavior of biodiesel soot. Combust Flame 2006;146:589–604. doi:10.1016/j.combustflame.2006.06.010.

[74] Stratakis GA, Stamatelos AM. Thermogravimetric analysis of soot emitted by a modern diesel engine run on catalyst-doped fuel. Combust Flame 2003;132:157–69. doi:10.1016/S0010-2180(02)00432-7.

[75] Lahaye J. Influence of cerium oxide on the formation and oxidation of soot. Fuel Energy Abstr 1996;37:206. doi:10.1016/0140-6701(96)88881-3.

[76] Vander Wal RL, Tomasek AJ. Soot oxidation: Dependence upon initial nanostructure. Combust Flame 2003;134:1–9. doi:10.1016/S0010-2180(03)00084-1.

[77] Vander Wal RL, Tomasek AJ. Soot nanostructure: Dependence upon synthesis conditions. Combust Flame 2004;136:129–40. doi:10.1016/j.combustflame.2003.09.008.

[78] Shao H, Lam W, Remias J, Roos J, Choi S, Seong H. Effect of Lubricant Oil Properties on the Performance of Gasoline Particulate Filter (GPF). SAE Int J Fuels Lubr 2016;9:2016-01–2287. doi:10.4271/2016-01-2287.

[79] Easter J. Influence of Fuel Introduction Parameters on the Reactivity and Oxidation Process of Soot from a Gasoline Direct Injection Engine. University of Michigan, 2018.

[80] Storey JM, Barone T, Norman K, Lewis S. Ethanol Blend Effects On Direct Injection Spark-Ignition Gasoline Vehicle Particulate Matter Emissions. SAE Int J Fuels Lubr 2010;3:2010-01–2129. doi:10.4271/2010-01-2129.

[81] Luo Y, Zhu L, Fang J, Zhuang Z, Guan C, Xia C, et al. Size distribution, chemical composition and oxidation reactivity of particulate matter from gasoline direct injection (GDI) engine fueled with ethanol-gasoline fuel. Appl Therm Eng 2015;89:647–55. doi:10.1016/j.applthermaleng.2015.06.060.

[82] Ruiz FA, Cadrazco M, López AF, Valdepeñas J, Agudelo JR. Impact of dual-fuel combustion with n-butanol or hydrous ethanol on the oxidation reactivity and nanostructure of diesel particulate matter. Fuel 2015;161:18–25. doi:10.1016/j.fuel.2015.08.033.

[83] Shulman ML, Jacobson MC, Carlson RJ, Synovec RE, Young TE. Dissolution behavior and surface tension effects of organic compounds in nucleating cloud droplets. Geophys Res Lett 1996;23:277–80. doi:10.1029/95GL03810.

[84] Novakov T, Penner JE. Large contribution of organic aerosols to cloud-condensation-nuclei concentrations. Nature 1993;365:823–6. doi:10.1038/365823a0.

[85] McMurry PH, Fink M, Sakurai H, Stolzenburg MR, Mauldin IL, Smith J, et al. A criterion for new particle formation in the sulfur-rich Atlanta atmosphere. J Geophys Res Atmos 2005;110:1–10. doi:10.1029/2005JD005901.

[86] Merikanto J, Napari I, Vehkamaki H, Anttila T, Kulmala M. New parameterization of sulfuric acid-ammonia-water ternary nucleation rates at tropospheric conditions. J Geophys Res Atmos 2007;112:1–9. doi:10.1029/2006JD007977.

[87] Zhang R, Suh I, Zhao J, Zhang D, Fortner EC, Tie X, et al. Atmospheric New Particle Formation Enhanced by Organic Acids. Science (80-) 2004;304:1487–9. doi:10.1126/science.1095139.

[88] Xu W, Zhang R. Theoretical investigation of interaction of dicarboxylic acids with common aerosol nucleation precursors. J Phys Chem 2012;116:4539–50. doi:10.1021/jp301964u.

[89] Carlton AG, Turpin BJ, Altieri KE, Seitzinger S, Reff A, Lim HJ, et al. Atmospheric oxalic acid and SOA production from glyoxal: Results of aqueous photooxidation experiments. Atmos Environ 2007;41:7588–602. doi:10.1016/j.atmosenv.2007.05.035.

[90] Kawamura K, Ng LL, Kaplan IR. Determination of organic acids (C1-C10) in the atmosphere, motor exhausts, and engine oils. Environ Sci Technol 1985;19:1082–6. doi:10.1021/es00141a010.

[91] Talbot RW, Beecher KM, Harriss RC, Cofer WRI. Atmospheric geochemistry of

formic and acetic acids at a mid-latitude temperate site. J Geophys Res 1988;93:1638–52. doi:10.1029/JD093iD02p01638.

[92] Zervas E, Tazerout M. Organic acids emissions from natural-gas-fed engines. Atmos Environ 2000;34:3921–9. doi:10.1016/S1352-2310(00)00160-6.

[93] Zervas E, Montagne X, Lahaye J. C 1 - C 5 Organic Acid Emissions from an SI Engine: Influence of Fuel and Air / Fuel Equivalence Ratio. Environ Sci Technol 2001;35:2746–51. doi:10.1021/es000237v.

[94] Zervas E, Montagne X, Lahaye J. Emission of specific pollutants from a compression ignition engine. Influence of fuel hydrotreatment and fuel/air equivalence ratio. Atmos Environ 2001;35:1301–6.

[95] Crisp TA, Brady JM, Cappa CD, Collier S, Forestieri SD, Kleeman MJ, et al. On the primary emission of formic acid from light duty gasoline vehicles and ocean-going vessels. Atmos Environ 2014;98:426–33. doi:10.1016/j.atmosenv.2014.08.070.

[96] Chebbi a, Carlier P. Carboxylic acids in the troposphere, occurence, sources and sinks: a review. Atmos Environ 1996;30:4223–49.

[97] Huang XF, Yu JZ. Is vehicle exhaust a significant primary source of oxalic acid in ambient aerosols? Geophys Res Lett 2007;34:1–5. doi:10.1029/2006GL028457.

[98] Fraser MP, Cass GR, Simoneit BRT. Gas-phase and particle-phase organic compounds emitted from motor vehicle traffic in a Los Angeles roadway tunnel. Environ Sci Technol 1998;32:2051–60. doi:10.1021/es970916e.

[99] Wentzell JJB, Liggio J, Li SM, Vlasenko A, Staebler R, Lu G, et al. Measurements of gas phase acids in diesel exhaust: A relevant source of HNCO? Environ Sci

Technol 2013;47:7663–71. doi:10.1021/es401127j.

[100] Pirjola L, Karl M, Ronkko T, Arnold F. Model studies of volatile diesel exhaust particle formation: Are organic vapours involved in nucleation and growth? Atmos Chem Phys 2015;15:10435–52. doi:10.5194/acp-15-10435-2015.

[101] Drozd GT, Zhao Y, Saliba G, Frodin B, Maddox C, Weber RJ, et al. Time resolved measurements of speciated tailpipe emissions from motor vehicles: trends with emission control technology, cold start effects, and speciation. Environ Sci Technol 2016:acs.est.6b04513. doi:10.1021/acs.est.6b04513.

[102] Arnold F, Pirjola L, Reichl U, Schlager H, Heikkila J, Keskinen J. First Online Measurements of Sulfuric Acid Gas in Modern Heavy-Duty Diesel Engine Exhaust: Implicationsfor Nanoparticle Formation. Environ Sci Technol 2012;46:11227–34.

[103] Lucachick GA, Kittelson D, Northrop W. Effects of Aftertreatment on Semi-Volatile Particulate Matter Emissions from Low Temperature Combustion in a Light-Duty Diesel Engine. SAE Int J Engines 2015;8:791–6. doi:10.4271/2015-01-0835.

[104] Bock N, Jeon J, Kittelson D, Northrop WF. Solid Particle Number and Mass Emissions from Lean and Stoichiometric Gasoline Direct Injection Engine Operation. SAE Tech Pap 2018-01-0359 2018. doi:10.4271/2018-01-0359.

[105] Swanson J, Kittelson D. Evaluation of thermal denuder and catalytic stripper methods for solid particle measurements. J Aerosol Sci 2010;41:1113–22. doi:10.1016/j.jaerosci.2010.09.003.

[106] Ntziachristos L, Amanatidis S, Samaras Z, Giechaskiel B, Bergmann A. Use of a Catalytic Stripper as an Alternative to the Original PMP Measurement Protocol.

SAE Int J Fuels Lubr 2013;6:532–41. doi:10.4271/2013-01-1563.

[107] Berndorfer A, Breuer S, Piock W, Von Bacho P. Diffusion Combustion Phenomena in GDi Engines caused by Injection Process. SAE Int 2013. doi:10.4271/2013-01-0261.

[108] Apple J, Gladis DD, Watts W, Kittelson D. Measuring Diesel Ash Emissions and Estimating Lube Oil Consumption Using a High Temperature Oxidation Method. SAE Pap 2009;2009-01–18. doi:10.4271/2009-01-1843.

[109] Parks JE, Storey JME, Prikhodko VY, Debusk MM, Lewis SA. Filter-Based Control of Particulate Matter from a Lean Gasoline Direct Injection Engine. SAE 2016 World Congr Exhib 2016:12. doi:10.4271/2016-01-0937.

[110] Zelenyuk A, Wilson J, Imre D, Stewart M, Muntean G, Storey J, et al. Detailed characterization of particulate matter emitted by lean-burn gasoline direct injection engine. Int J Engine Res 2017;18:560–72. doi:10.1177/1468087416675708.

[111] Maricq MM, Szente J, Loos M, Vogt R. Motor Vehicle PM Emissions Measurement at LEV III Levels. SAE Int J Engines 2011;4:597–609. doi:10.4271/2011-01-0623.

[112] Kirchner U, Vogt R, Maricq M. Investigation of EURO-5 / 6 Level Particle Number Emissions of European Diesel Light Duty Vehicles. Sae Pap 2010-01-0789 2010. doi:10.4271/2010-01-0789.

[113] Bock N, Jeon J, Kittelson D, Northrop W. Effects of Fuel Properties on Particle Number and Particle Mass Emissions from Lean and Stoichiometric Gasoline Direct Injection Engine Operation. SAE Tech Pap 2019-01-1183 2019. doi:10.4271/2019-01-1183.

[114] Kocsis MC, Briggs T, Anderson G. The Impact of Lubricant Volatility, Viscosity

and Detergent Chemistry on Low Speed Pre-Ignition Behavior. SAE Int J Engines 2017;10:2017-01–0685. doi:10.4271/2017-01-0685.

[115] Mayer M, Hofmann P, Geringer B, Williams J, Moss J. Influence of Different Fuel Properties and Gasoline - Ethanol Blends on Low-Speed Pre-Ignition in Turbocharged Direct Injection Spark Ignition Engines. SAE Int J Engines 2016;9:2016-01–0719. doi:10.4271/2016-01-0719.

[116] Jatana GS, Splitter DA, Kaul B, Szybist JP. Fuel property effects on low-speed pre-ignition. Fuel 2018;230:474–82. doi:10.1016/j.fuel.2018.05.060.

[117] Hülser T, Grünefeld G, Brands T, Günther M, Pischinger S. Optical Investigation on the Origin of Pre-Ignition in a Highly Boosted SI Engine Using Bio-Fuels 2013. doi:10.4271/2013-01-1636.

[118] Splitter D, Kaul B, Szybist J, Jatana G. Engine Operating Conditions and Fuel Properties on Pre-Spark Heat Release and SPI Promotion in SI Engines. SAE Int J Engines 2017;10:2017-01–0688. doi:10.4271/2017-01-0688.

[119] Noma K, Noda T, Isomura H, Ashida T, Kamioka R, Isoda T, et al. A Study of Injector Deposits, Combustion Chamber Deposits (CCD) and Intake Valve Deposits (IVD) in Direct Injection Spark Ignition (DISI) Engines ll. SAE Tech Pap Ser 2003. doi:10.4271/2002-01-2659.

[120] DuMont RJ, Evans JA, Feist DP, Studzinski WM, Cushing TJ. Test and Control of Fuel Injector Deposits in Direct Injected Spark Ignition Vehicles. SAE Tech Pap 2009;4970. doi:10.4271/2009-01-2641.

[121] Joedicke A, Krueger-Venus J, Bohr P, Cracknell R, Doyle D. Understanding the Effect of DISI Injector Deposits on Vehicle Performance. SAE Int 2012.

doi:10.4271/2012-01-0391.

[122] Stanmore B, Brilhac J, Gilot P, Gestion L. The Ignition and Combustion of Cerium Doped Diesel Soot. SAE Tech Pap 1999-01-0115 1999.

[123] Rodriquez-Rernandez J, Olivia F, Vzquez RA. Characterization of the Diesel Soot Oxidation Process through an Optimized Thermogravimetric Method. Energy & Fuels 2011:2039–48. doi:10.1021/ef200194m.

[124] Kęder M, Grzeszczyk R, Merkisz J, Fuć P, Lijewski P. Design of a New Engine Dynamometer Test Stand for Driving Cycle Simulation. J KONES Powertrain Transp 2014;21:217–24. doi:10.5604/12314005.1130477.

[125] ANDRONE C-F, Rao SB. Vehicle Simulation for Powertrain System Testing. Chalmers University of Technology, 2017.

[126] Terres A, Ebert V, Nowak A, Rosahl J, Hildebrandt M, Southgate J, et al. Particle Measurement Programme (PMP): Inter-laboratory correlation exercise with Condensation Particle Counters (CPCs). 2018. doi:10.2760/859241.

[127] Hinds WC. Aerosol technology: properties, behaviour, and measurement of airborne particles. 2nd ed. Wiley-Interscience; 1999.

[128] Bock N, Baum MM, Anderson MB, Pesta A, Northrop WF. Dicarboxylic Acid Emissions from Aftertreatment Equipped Diesel Engines. Environ Sci Technol 2017;51:13036–43. doi:10.1021/acs.est.7b03868.

[129] Bock NRH, Baum MM, Moss JA, Castonguay AE, Jocic S, Northrop WF. Dicarboxylic acid emissions from a GDI engine equipped with a catalytic gasoline particulate filter. Fuel 2020;275. doi:10.1016/j.fuel.2020.117940.

[130] Nolte CG, Solomon PA, Fall T, Salmon LG, Cass GR. Seasonal and spatial

characteristics of formic and acetic acids concentrations in the Southern California atmosphere. Environ Sci Technol 1997;31:2547–53. doi:10.1021/es960954i.

[131] Stivender DL. Development of a Fuel-Based Mass Emission Measurement Procedure. SAE Tech Pap 1971. doi:10.4271/710604.

[132] Lucachick G, Curran S, Storey J, Prikhodko V, Northrop WF. Volatility characterization of nanoparticles from single and dual-fuel low temperature combustion in compression ignition engines. Aerosol Sci Technol 2016;50:436–47. doi:10.1080/02786826.2016.1163320.

[133] Friedman B, Link MF, Fulgham SR, Brophy P, Galang A, Brune WH, et al. Primary and Secondary Sources of Gas-Phase Organic Acids from Diesel Exhaust. Environ Sci Technol 2017. doi:10.1021/acs.est.7b01169.

[134] Marr LC, Kirchstetter TW, Harley RA, Miguel AH, Hering S V., Hammond SK. Characterization of polycyclic aromatic hydrocarbons in motor vehicle fuels and exhaust emissions. Environ Sci Technol 1999;33:3091–9. doi:10.1021/es981227l.

[135] Zheng X, Wu Y, Zhang S, Hu J, Zhang KM, Li Z, et al. Characterizing particulate polycyclic aromatic hydrocarbon emissions from diesel vehicles using a portable emissions measurement system. Sci Rep 2017;7:1–12. doi:10.1038/s41598-017-09822-w.

[136] Eiguren-Fernandez A, Miguel AH. Size-resolved polycyclic aromatic hydrocarbon emission factors from on-road gasoline and diesel vehicles: Temperature effect on the nuclei-mode. Environ Sci Technol 2012;46:2607–15. doi:10.1021/es2037004.

[137] Skeen SA, Michelsen HA, Wilson KR, Popolan DM, Violi A, Hansen N. Near-threshold photoionization mass spectra of combustion-generated high-molecular-

weight soot precursors. J Aerosol Sci 2013;58:86–102. doi:10.1016/j.jaerosci.2012.12.008.